SYNTHESIS AND ANALYSIS OF SUPERHYDROPHOBIC-BASED CORROSION PROTECTION SYSTEMS FOR ALUMINUM ALLOYS AND THEIR EVALUATIONS ON FRICTION STIR SPOT-WELDED METALS

A Dissertation by

Sarah F. Jurak

Master of Science, Wichita State University, 2011

Bachelor of Science, Wichita State University 2008

Submitted to the Department of Mechanical Engineering
and the faculty of the Graduate School of
Wichita State University
in partial fulfillment of
the requirements for the degree of
Doctor of Philosophy

May 2018

SYNTHESIS AND ANALYSIS OF SUPERHYDROPHOBIC-BASED CORROSION PROTECTION SYSTEMS FOR ALUMINUM ALLOYS AND THEIR EVALUATIONS ON FRICTION STIR SPOT-WELDED METALS

The following faculty members have examined the final copy of this dissertation for form and content, and recommend that it be accepted in partial fulfillment of the requirement for the degree of Doctor of Philosophy with a major in Mechanical Engineering.

_____
Ramazan Asmatulu, Committee Chair

_____
Gamal Saad Weheba, Committee Member

_____
Yimesker Yihun, Committee Member

_____
Rajeev Nair, Committee Member

_____
Enkhsaikhan Boldsaikhan, Committee Member

Accepted for the College of Engineering

_____
Royce Bowden, Dean

Accepted for the Graduate School

_____
Dennis Livesay, Dean

DEDICATION

To George Talia, who started me on the path to this degree and was a great inspiration to me but was unable to be there to see it finished—he is deeply missed; and to my husband, who encouraged me to become an engineer and has been an invaluable support through all my degrees—without him I would not have achieved all that I have or even thought to try

ACKNOWLEDGMENTS

First, I would like to thank my advisor, Ramazan Asmatulu, for his expert guidance and support. He found the financial support that made my research possible and made sure I had all the resources I needed to be successful. I also thank the Department of Mechanical Engineering for the education needed to be a success and for providing the support, facilities, and equipment that allows inquiring, imaginative minds to make ideas a reality. Also, I would like to recognize Michael McCoy who helped me get started with my research. Finally, I would like to recognize the Cessna Shop and Advanced Joining and Processing Laboratory employees who provided crucial help in producing the welds and material specimens for this research.

ABSTRACT

The friction stir spot weld (FSSW) could potentially replace rivets as in situ fasteners, but the welding process results in a loss of corrosion resistance in the weld. The cost of corrosion to the U.S. economy in 2013 rose to $1 trillion annually, and the development of more effective corrosion control methods is needed. Of the different types of corrosion, galvanic corrosion is the most common and most destructive. This research investigates the effect of a superhydrophobic coating on the galvanic corrosion mechanism in the FSSW. Dissimilar friction stir spot welds were prepared using AA2024-T3 and AA7075-T6 materials. The development of a superhydrophobic coating was focused on creating a micro-nanostructured hierarchical surface morphology with a low surface energy component. The final coating was composed of a 58.7 wt% mineral spirits. 12.8 wt% silicone (Si) component, 17.8 wt% 74 μm aluminum (Al) particles, and 10.7wt % < 45 nm zinc oxide (ZnO) particles. Testing of the coating included static water contact angle (WCA) testing, which resulted in an average WCA of 158°. Determination of the sliding angle (SA) and WCA hysteresis found a SA of 4.08° with hysteresis of 7.6°. Adhesion of the coating to the substrate was verified by cross-hatch tape testing according to ASTM D3359, which showed less than 5% loss of material. Durability of the coating was tested by exposure to a base solution with a Ph of 9, a 0.5M H_2SO_4 acid solution, and an acetone solvent. Only the base solution had a significant detrimental effect on the coating WCA, decreasing the WCA from 154° to 109°. Corrosion mitigation of the coating was determined by comparing electrochemical testing of the coated AA2024 specimens, coated AA7075 specimens, and coated friction stir spot welds, with uncoated FSSW and bare aluminum materials. The coating was shown to decrease the current density with a more positive potential, indicating an improvement in corrosion mitigation. The corrosion rates for the coated specimens were significantly lower than those for the bare materials.

TABLE OF CONTENTS

TABLE OF CONTENTS (continued)

LIST OF FIGURES

LIST OF FIGURES (continued)

LIST OF FIGURES (continued)

LIST OF TABLES

LIST OF ABBREVIATIONS

AA	Aluminum Association
AE	Acoustic Emission
AFM	Atomic Force Microscopy
AJP	Advanced Joining and Processing Laboratory
Al	Aluminum
AMEC	Aerospace Metals Engineering Committee (of SAE)
AMS	Aerospace Material Specifications
ASM	American Society for Metals
ANOVA	Analysis of Variance
ANSI	American National Standards Institute
ASTM	American Society for Testing and Materials International
AWS	American Welding Society
BTA	Benzotriazole
C	Carbon
CAH	Contact Angle Hysteresis
CFD	Computational Fluid Dynamics
CNC	Computer Numerical Control
Cp-Ti	Commercially Pure Titanium
Cr	Chromium
CT	Computer Tomography
Cu	Copper
CAH	Contact Angle Hysteresis

LIST OF ABREVIATIONS (continued)

DMF	Dimethylformamide
DOE	Design of Experiments
DSC	Differential Scanning Calorimetry
F	Fluoride
FAA	Federal Aviation Administration
FAS	Fluoroalkylsilane
FSW	Friction Stir Welding
FSSW	Friction Stir Spot Weld
FTIR	Fourier Transform Infrared Spectroscopy
G2MT	Generation 2 Material Technology
GDP	Gross Domestic Product
GLCM	Gray Level Co-occurrence Matrix
GPB	Guinier-Preston-Bagaryatsky
GWP	Gross World Product
H	Hydrogen
HAZ	Heat-Affected Zone
HH	High RPM with High IPM
HL	High RPM with Low IPM
HMDS	Hexamethyldisiloxane
HV	Vickers Hardness
IIW	International Institute of Welding
IL	Ionic Liquid

LIST OF ABREVIATIONS (continued)

IPM	Inches per Minute
ISO	International Organization of Standardization
L	L-Direction (with the grain of the material)
LH	Low RPM with High IPM
LL	Low RPM with Low IPM
LOC	Lack of Consolidation
LOP	Lack of Penetration
LQR	Linear-Quadratic Regulator
LT	LT-Direction (long transverse; perpendicular or transverse to grain)
Mg	Magnesium
MMDPS	Metallic Material Properties Development and Standardization
MO	Molybdenum
MPO	Microplasmas Oxidizing
MTES	Methyltriethoxysilane
MWCNT	Multi-Walled Carbon Nanotube
N	Nitrogen
NACE	National Association of Corrosion Engineers
NASA	National Aeronautics and Space Administration
NASM	National Aerospace Standard, Inch
NCAT	National Center for Aviation Training
Ni	Nickel
O	Oxygen

ORMOSIL	Organically Modified Silica
PAN	Polyacrylonitrile
PDMS	Polydimethylsiloxane
PFPE	Perfluoropolyether
PEEK	Polyetheretherketone
PTES	Perfluorooctyltriethoxysilane
PVDF	Polyvinylidene Fluoride
RMS	Root-Mean-Square
RO	Reverse Osmosis
RPM	Revolutions per Minute
RTV	Room Temperature Vulcanizing
SA	Sliding Angle
SAE	Society of Automotive Engineers International
SAM	Self-Assembled Monolayer
SCE	Saturate Calomel Electrode
SEM	Scanning Electron Microscopy
Si	Silicon
SKPFM	Scanning Kelvin Probe Force Microscopy
SMP	Shape Memory Polymer
SVET	Scanning Vibrating Electrode Technique
SVM	Support Vector Machine
TEM	Transmission Electron Microscopy

TEOS	Tetraethoxysilane
Ti	Titanium
TMAZ	Thermo-Mechanically Affected Zone
TMCS	Trimethylchlorosilane
TWI	The Welding Institute
UTS	Ultimate Tensile Strength
UV	Ultraviolet
V	Vanadium
WCA	Water Contact Angle
XPS	X-Ray Photoelectron Spectroscopy
XRD	X-Ray Diffraction Analysis
Yt	Ytterbium
Zn	Zinc
ZnO	Zinc Oxide
Zr	Zirconium

LIST OF SYMBOLS

e^-	Electron
S´(S)	Strengthening Precipitate Phases in Al-Cu-Mg Alloys with Composition of Al_2CuMg
η	Strengthening Precipitate Phase of Al-Zn-Mg -Cu Alloys with Composition of $Mg(Al,Zn,Cu)_2$
ή	Strengthening Precipitate as Metastable Form of η Precipitates in Al-Zn-Mg-Cu Alloys
^{o}	Degree

CHAPTER 1

INTRODUCTION

1.1 Friction Stir Welding and Corrosion

Friction stir welding (FSW) is an environmentally friendly process, which does not produce toxic by-products or require cover gases or large amounts of energy. No fillers are necessary, so there is no change in the bulk chemistry of the material, and it does not reach solidus temperature, so there is no bulk solid-to-liquid transformation. As a result, friction stir welds generally have less residual stress, distortion, and shrinkage with better mechanical properties than welds produced by most conventional fusion methods [1]. FSW is presently being used in the aircraft industry in the design and manufacturing of aircraft. The friction stir spot weld (FSSW) could potentially replace rivets as in situ fasteners, but the welding process results in changes in the microstructure in the weld material which affects the corrosion resistance of the weld. The mechanical fasteners used currently have their own corrosion problems, but the use of the FSSW could introduce new problems associated with the exit hole of the spot weld, which can collect moisture and result in corrosion and galvanic corrosion between the weld material and base material.

Corrosion is a problem that warrants attention worldwide. The National Association of Corrosion Engineers (NACE) study released in 2002 estimated that the cost of direct corrosion to the economy was approximately $276 billion yearly, which was 3.1% of the gross domestic product (GDP) [2]. Direct costs are the result of the overdesign to account for corrosion, and the treatment of metals and parts to enhance corrosion resistance. This affects the manufacturing and construction of America's bridges, equipment, and infrastructure. Direct costs also include safety inspections, maintenance, and repair as well as replacement of corroded parts, equipment, and

infrastructure. Indirect costs are the result of failures due to corrosion, which result in injuries and destruction of property. The consequential lawsuits can be very expensive. There is also loss of time and wages due to downtime for maintenance and repairs. A depiction of the direct costs to society, from the NACE Cost of Corrosion Study, is shown in Figure 1.1(a). The indirect costs are as costly as direct costs. According to Generation 2 Materials Technology (G2MT) Laboratories, in today's dollars, the cost would be over $500 billion per year for direct costs due to inflation, which means the cost of both direct and indirect effects of corrosion had risen to above 1 trillion dollars annually by 2013, as shown in Figure 1.1(b) [3].

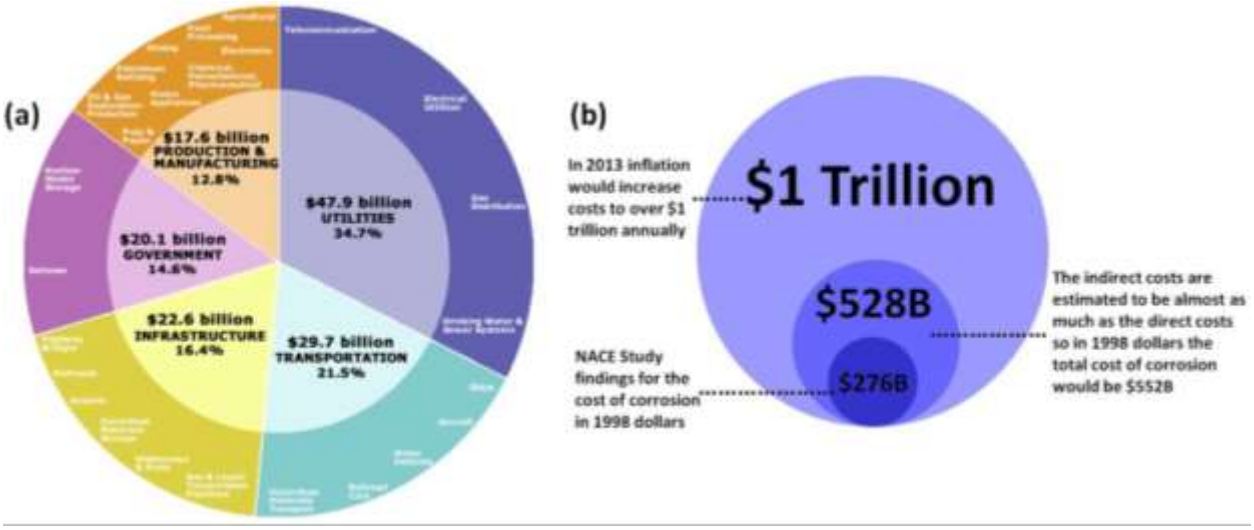

Figure 1.1. Direct and indirect costs to society as the result of corrosion failure: (a) findings of NACE corrosion study from NACE International 1], and (b) extrapolation of NACE study results of 1998 data to 2013 dollars [3].

Corrosion is very costly to our economy. It comprises 6.1% of the GDP, as shown in Figure 1.2. As part of the global economy with a gross world product (GWP) of 84.97 trillion in 2012 and assuming 6% for corrosion costs, corrosion is costing, globally, more than 5 trillion annually [3]. Advances in technology and industry practices have saved billions of dollars in the economic cost of corrosion with advances in corrosion protection systems and corrosion-resistant materials, but the savings are dwarfed by rising costs. That is why new materials and advances in corrosion

protection systems are so imperative. Even more alarming is the fact that the infrastructure of the U.S. is aging. This means replacements will be needed for ports, roads, bridges, utilities, railroads, etc. as corrosion takes its toll. With the state of the U.S. debt and economy this will be an ever-increasing problem. Therefore, research continues into new effective methods to address corrosion.

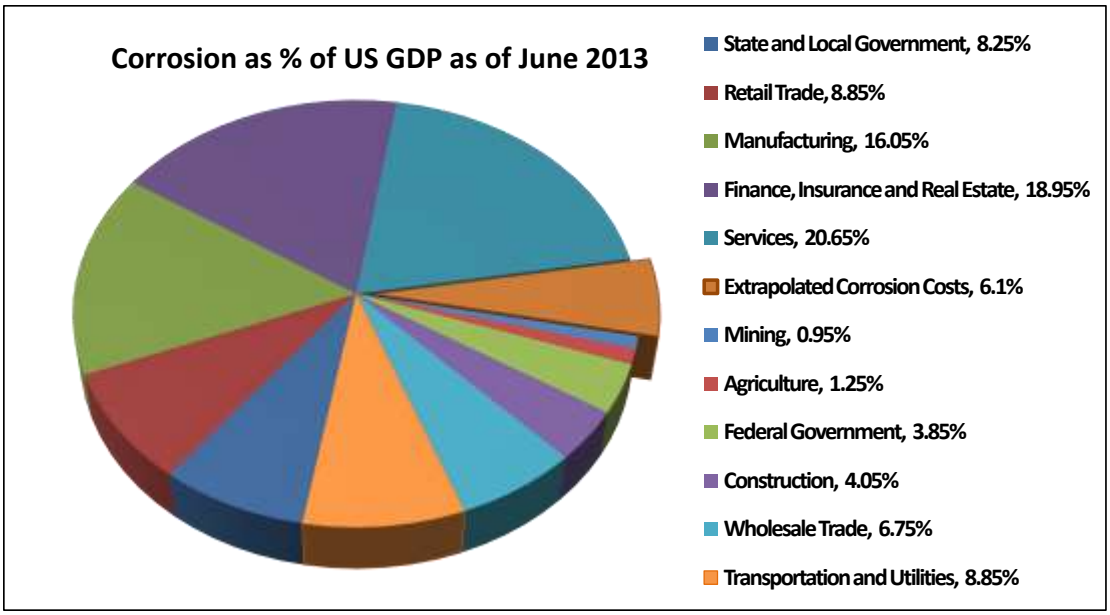

Figure 1.2. Cost of corrosion as part of U.S. GDP [2].

The aircraft industry would find the replacement of rivets with friction stir spot welds attractive, but the corrosion issue causes concern. The exit hole that is produced with traditional methods of friction stir spot welding can be addressed with the refill spot weld technique [4], but the galvanic corrosion issue is complex. The rivets are mechanical fasteners used to fasten the skin of the airplane to the stringers. The skin is AA2024-T3 and the stringers are AA7075-T6 aluminum (Al) alloys. The FSSW would be a dissimilar lap spot weld. Dissimilar welds are welds comprised of two different alloys, in this case AA2024 and AA7075. This causes potential galvanic corrosion between the differing alloy compositions within the weld. The complex nature of the corrosion process in the dissimilar FSSW is difficult to address.

The friction stir spot weld could be an asset to the aviation industry because it can reduce weight by replacing traditional joining and fastener methods with friction stir welds. FSW allows them to use lighter and stronger metals, which are difficult to join by other welding methods. Rivets could be replaced by the FSSW as in-situ fasteners, which would also reduce costs by reducing the part counts. FSSW is attractive to both the aerospace and automotive industries and because of the ergonomic factors associated with the installation of mechanical fasteners and the increased speed of making spot welds, robotics applications could be beneficial to many industries.

1.2 References for Chapter 1

[1] S. F. Jurak, "Statistical Analysis of the Mechanical Properties of Friction Stir Welds in 2024 and 2198 Aluminum Alloys," Master's Thesis, Wichita, State University, Wichita, KS, 2010.

[2] NACE International, "Corrosion Costs and Preventive Strategies in the United States," Houston, TX, 2002.

[3] Joshua E. Jackson, "The Cost of Corrosion Exceeds $1 Trillion in the U.S. in 2013," G2MT Laboratories, Houston, TX, 2011.

[4] S. F. Jurak, E. Jurak, and R. Asmatulu, "Recent Progress in Friction Spot Welding Processes of Metallic Materials," in *Composites and Advanced Materials Expo: Combined Strength. Unsurpassed Innovation*, CAMX 2014, Orlando, FL, October 13–16, 2014.

CHAPTER 2

LITERATURE REVIEW

2.1 Friction Stir Welding Process

Friction stir welding is a technology that was developed in 1991 by The Welding Institute (TWI), a British research facility [1] [2] [3] [6]. FSW is a thermo-mechanical process. Workpieces are joined by lowering a rotating weld tool into the material which effectively stirs the material as it is softened by the heat introduced into the area by frictional and forging forces. The weld tool is a cylindrical tool with a probe extending from the shoulder at the end. The shoulder rests on the material surface as the probe is lowered into the material to be welded. The tool rotaion speed, travel rate of the weld tool through the material and force applied by the shoulder of the tool on the surface are parameters used to control the heat introduced into the weld zone. The metal is heated by frictional and forging forces produced by the rotating probe, which results in softening of the material, but the temperature should be kept below the solidus temperature to minimize microstructural changes in the weld material. Friction stir welds generally have less residual stress and distortion with better mechanical properties than some other methods due to the fact that the material is heated to very near the melting point but is kept below the solidus temperature.

As the material is stirred the weld parameters and features on the weld tool work together to produce a solid defect free weld [6]. These weld tool design features can include scrolls added to the shoulder or threads to the probe which can facilitate mixing of material during the welding process. Flats or flutes also can be added to the probe. These features assist in moving material from the crown to the root of the weld and facilitate movement of material around the probe from the leading edge to the trailing edge of the weld tool. The shoulder at the material surface can be flat or curved. A concave shoulder can help contain the material during welding to lessen the

incidence of flash formation at the weld edge. Even slight changes in the weld tool design, such as changing the angle or spacing of the threads on the probe, can affect material movement in the weld zone. The number of scrolls or the direction of the scrolls can also be changed. The FSW process has been shown to be a path-independent process [4] [5]. Each tool design has a process window identified by the travel speed and revolution per minute (RPM) rotation of the weld tool, which includes weld parameter combinations that can produce a strong defect free weld [6]. Examples of process windows for different weld tool designs are shown in Figure 2.1.

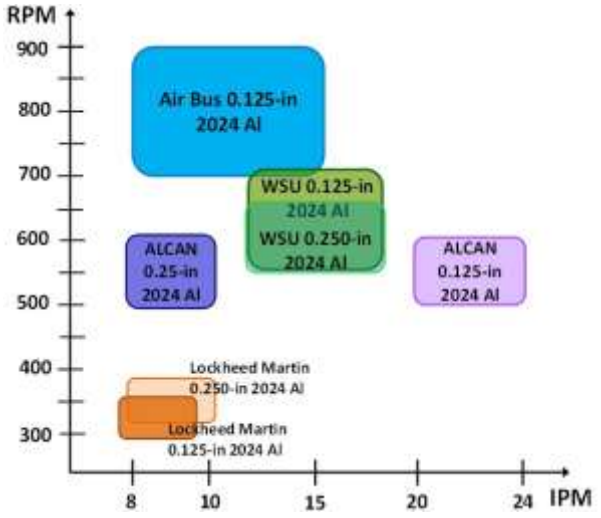

Figure 2.1. Examples of process windows for different weld tool designs used to produce welds of AA2024-T3 aluminum alloy [6].

There are microstructural gradients created by the friction stir welding process. The gradients can be separated into distinct microstructural regions; the nugget, the thermo-mechanically affected zone (TMAZ), and the heat affected zone (HAZ). During the FSW process, material is effectively forged by the probe from the leading edge to a void that forms behind the probe, filling in the void as the weld is produced [6] [7]. The flow of material around the probe forms the nugget (stir zone). The forging forces of the the probe moving through the material results in rotation of the grains adjacent to the nugget. The heat flowing into the area from the stir zone and the forging forces result in the thermo-mechanically affected zone (TMAZ). Frictional

energy from rotation of the shoulder on the surface introduces heat into the material under the tool shoulder, and heat flows into the area through the TMAZ forming the heat-affected zone (HAZ). A schematic of a linear friction stir butt-weld process is shown in Figure 2.2. The advancing side of the weld is defined as the side of the tool where the rotational direction is the same as the direction of travel.

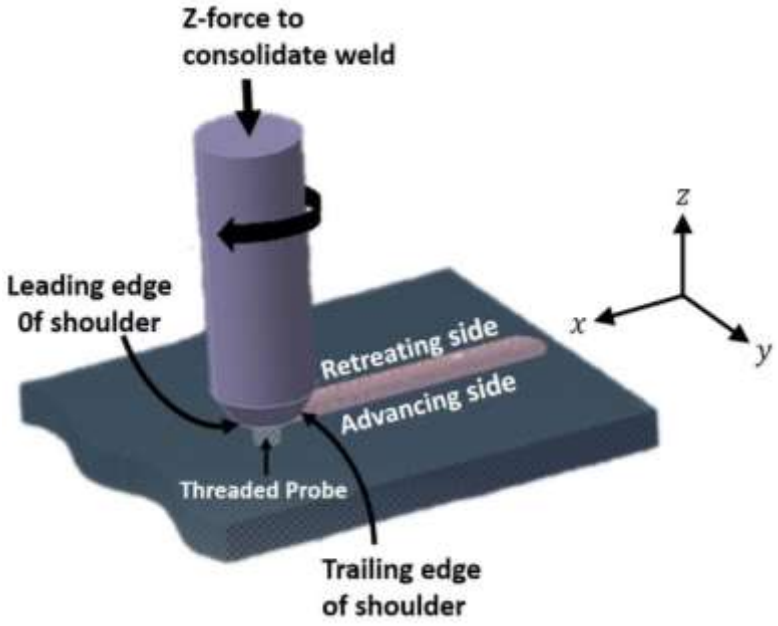

Figure 2.2. Depiction of the linear friction stir welding process for a butt weld including the conventioinal axis-directions.

The approximate location of the different zones or microstructural areas of FSW superimposed on a micrographic cross-section of a linear butt weld is shown in Figure 2.3. Below the micrographic image is shown a full field microhardness map of the weld. The hardness profile is related to the microstructure of the weld. The final microstructure of the weld material in a friction stir weld is dependent on the temperature history in the material during the welding process [6] [8]. The hardness maximum in this weld is in the nugget, which is associated with fine equiaxial grains as a result of continuous dynamic recrystallization [9]. The TMAZ is an area of high angle rotation and some coarsening of the grains. The HAZ has a coarse ‘over-aged’ grain structure

which resultes in an area of minimum hardness caused by the thermal effects of the welding process.

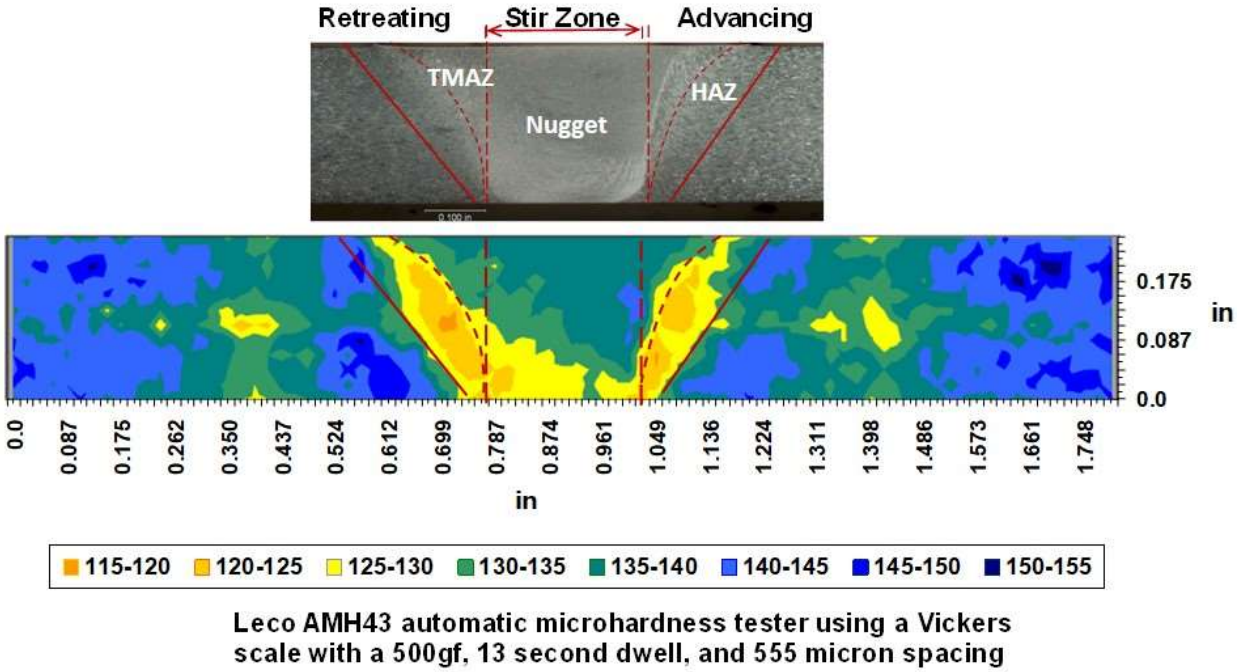

Figure 2.3. AA2024-T3 weld specimen with microstructural zones identified on macrograph cross section of joint with microhardness map [6].

2.2 FSW Effect on Precipitate-Hardened Metals

In precipitate-hardened metals such as the 2XXX and 7XXX series aluminum alloys, grain size is the result of temperatures experienced within the weld zone during the FSW process and the length of time they were maintained [6]. Maximum hardness in precipitate-hardened aluminum alloys occurs when there are small strengthening phase particulates, or S´(S) particulates, well dispersed and coherent in the matrix. When higher temperatures occur or lower temperatures for extended periods, course incoherent phases form, which result in a loss of strength. This mechanism is referred to as over-aging [10].

In the 2024-T3 base metal, the strengthening precipitates are Guinier-Preston-Bagaryatsky (GPB) zones [6]. The GPB zones of Cu and Mg are clusters of atoms that form thin plates as the

solutes become supersaturated with heating and then quenching of the material, such as in the process to obtain the 2024-T3 temper used in this study. The FSW process results in a dissolution of the GPB zones and S´(S) ($Al_2\,CuMg$) phases precipitate from the solid solution. The temperatures achieved in the nugget cause dissolution of the S'(S) preecipitates, and dynamic recrystallization results in a microstructure comprised of fine equiaxed grains with high angle boundaries and some GPB zones with few dislocations. GPB zones are at a minimum in the TMAZ and the deformation due to the forging forces of the probe causes a rotation of the grains with a high concentration of dislocations. In addition, temperatures reached cause S´(S) precipitation and coarsening of the grains. Therefore, there is a softening of the material in the TMAZ. In the HAZ, the area is affected only by heat but near the TMAZ, there is a microstructure similar to that of the TMAZ. On the other side of the HAZ near the parent material there is an increase in concentration of GPB zones closer to that found in the parent material. In the middle of the HAZ between theses two zones, the granular structure is made up of course grains of S´(S) phases and precipitate-free zones. Coarse S'(S) phases do not contribute sufficiently to the strength of the material which results in the minimum hardness area of the friction stir weld being located in the HAZ [11]. Due to this minimum hardness in the HAZ with the rotation of grains and high concentration of dislocations in the TMAZ, a defect-free friction-stir weld will usually fail in the TMAZ/HAZ region at a 45º angle. When defects are present in the nugget, the failure can be in the nugget, with the characteristic "onion rings" effect seen [6].

AA7075 is an Al-Zn-Mg-Cu alloy. There is disagreement on the precipitates formed with heating and quenching this alloy [6]. The strengthening precipitates in the 7XXX series metal alloy are ή precipitates and η ($MgZn_2$) precipitates. The ή are metastable forms of the η precipitates. Larger $Mg(Zn_2AlCu)$ as well as the $Mg_{32}(Al,Zn)_{49}$ precipitates have been reported. Corrosion

initiates in the precipitate-free zones and is associated with coarse precipitates. Friction stir welding results in coarse grain boundary and intergranular precipitates with wide precipitate-free zones in the HAZ which increases the materials susceptibility to corrosion in this area [6] [12] [13]. In the TMAZ larger precipitates are unchanged but the smaller precipitates have coarsened. The nugget displays an absence of intergranular precipitates and precipitate-free zones. As with the 2024 material, the nugget is comprised of fine equiaxed grains with high angle boundaries. Also, $Mg_{32}(Al, Zn)_{49}$ or $Mg(Zn_2, AlCu)$ precipitates are present. A few dislocations can also be found in the the nugget [13].

2.3 Determining the Quality of Weld

2.3.1 Possible Defects in Friction Stir Weld

Certain types of defects are possible in the friction sir weld just as with other methods of welding. One of the major defects is lack of penetration (LOP) which occurs when the probe length is too short or forge forces are inadequate. This results in a loss of strength in the weld. Figure 2.4 is a cross-section of a weld produced in the Advanced Joining and Processing Laboratory at Wichita State University with LOP indicated by the arrow in the root of the weld.

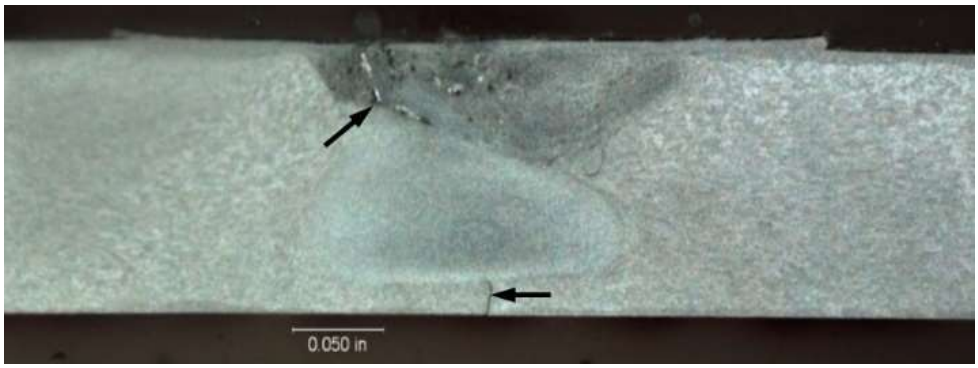

Figure 2.4. LOP present at root of weld, indicated by bottom arrow, and lack of consolidation present at crown of weld, noted by top arrow.

Some defects in the weld are the result of flow deficiencies caused by the tool design chosen with the combination of parameters used along with the material properties of the

workpiece. If the weld parameters and tool design result in temperatures in the weld zone that are too high (hot), then the condition of contact between the probe and work piece material can be a stick condition where there is an excessive flow around the probe resulting in flash and surface galling. If the weld parameters are too "cold," then a slip condition can result with insufficient flow of material around the probe [14], resulting in a worm hole or lack of consolidation (LOC) on the advancing side of the nugget. This is caused by the flow of material around the probe from the leading edge to the trailing edge being inadequate to fully fill in the void behind the probe as the tool advances. Figure 2.4 shows a lack of consolidation at the crown of the nugget as indicated by the arrow. Figure 2.5(f) is an example of a void in the weld. In order to avoid flow-related defects, the process parameters need to produce a stick-slip wiping flow at the interface (shear zone) of the probe and the work piece material, with the material flow from the front of the probe balanced with the flow into the void that forms behind the probe [14].

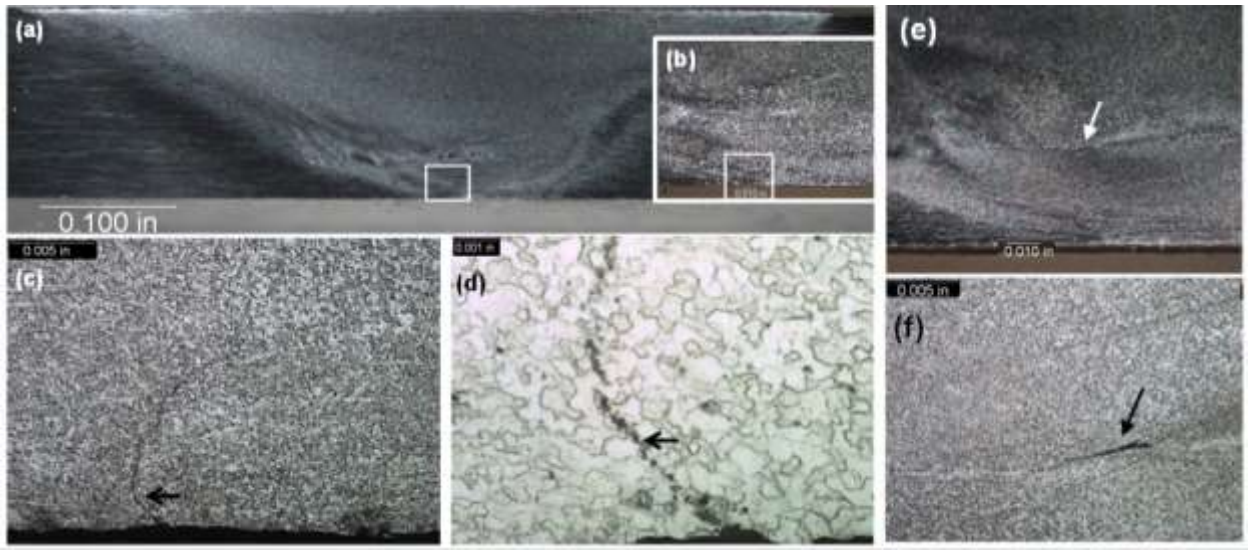

Figure 2.5. Micrograph cross-section of welds: (a) metallographic specimen, (b) higher magnification of section noted by square in previous view, (c) further magnification of outlined section with faying surface oxide remnant identified by arrow, (d) higher magnification of faying surface, (e) weld identifying void location, and (f) higher magnification of void [6].

If there is an inadequate flow of material in the stir zone, the oxide layer ($A1_2O_3$) on the surface of the aluminum alloy is not broken up and is seen in the shape of a “Lazy S” or “Zigzag” curve in the weld. Figure 2.5 (c-d) shows a micrograph of a weld cross-section with the Lazy S present [6]. This defect results in a residual oxide defect in the form of voids containing Al and O in the weld [15]. Crack initiation can occur during tensile testing due to this weakness in the weld [6] [16], and microcracks can occur in the residual oxide material with post-weld heat treatments even when the residual oxide layer cannot be seen [6][16].

In the case of LOP and the residual oxide defects, a condition referred to as a “kissing bond” results, which is another reason for loss of strength in the weld. The kissing bond refers to an area where two surfaces that have been joined are in contact with each other but have little to no metallic bond present [17]. This is the direct result of sliding friction conditions during welding. Surface stretch and shear are needed to produce a good bond, which is not present in the sliding condition [17].

Another defect that can occur is underfill. This is the result of too much flash being produced with the FSW process. If there is sufficient loss of material to cause a loss of thickness in the area of the weld underfill can occur. This loss of thickness will adversely affect the strength of the weld. The forces produced during FSW make securing the workpieces very important. If the workpieces are not adequately secured a mismatch across the joint can occur which can also affect the strength of the weld. An illustration of these defects is shown in Figure 2.6, where T is the thickness of the material, and h is the depth of the discontinuity. In FSW standards, these potential weld defects are referred to as discontinuities [18].

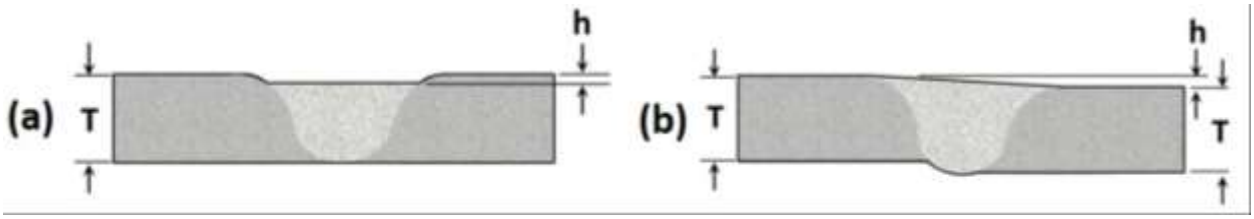

Figure 2.6. Illustrations of defects: (a) underfill discontinuity of friction stir weld, and (b) mismatch discontinuity [18].

If weld parameters are used which produce “hot” conditions when making a lap weld, an up-turn of material, or hooking effect, can occur at the edge of the weld zone in the area of the fusion of the two materials [19]. Weld parameters that produce “hot” conditions in the weld can result in a flow pattern of recirculation, whereby downward flow is reversed into an upward flow which is what causes the “hooking” defect [17].

2.3.2 Applicable Standards

There are standards which have been written to cover friction stir welding. The International Organization of Standardization (ISO) has published an ISO standard, ISO 25239-5:2011, This standard was prepared by the International Institute of Welding (IIW) for friction stir welding of aluminum, and provides quality standards for FSW but does not apply to friction stir spot welding. Included in this standard are design requirements, a set of rules for qualification of the welding procedure, and definitions of specific quality requirements. There are also requirements for qualification of the welding operator and requirements for inspection and testing are outlined.

The American Welding Society (AWS) developed AWS D17.3/D17.3M:2010 which is a standard for friction stir welding of aluminum in aerospace applications [18]. This is the standard used most often in the U.S. and it includes design and classification of welds for service and subsequent acceptance inspections, qualification of the welding procedure, qualification of the welding operator, and quality requirements for discontinuities. Other standards are referenced as

mandatory provisions of this AWS standard. Discontinuities are discussed and acceptance criteria including testing standards and ASTM standards are included where applicable. Friction stir spot welds are not mentioned in this specification. This standard is also approved by the American National Standards Institute (ANSI).

2.3.3 Evaluation of Friction Stir Weld

ASTM, AWS, or NASM standards. For microhardness testing ASTM E384 can be applied.and conductivity testing can be done according to ASTM E1004-17. Conductivity testing provides information about the microstructure in the weld because a changes in microstructure effects electrical conductivity in the weld zone [10]. The AWS D17.3/D17.3M:2010 standard [18] provides guidelines for evaluating the quality of the friction stir weld. Friction stir welds of pipes, sheets, and plates are tensile tested, and toughness testing is performed when required depending on the application. Fillet welds and friction stir lap seam welds are shear tested. This standard also provides instruction for the locations of test specimens in the weld and configuration of test specimens. Non-destructive testing can also be performed to identify discontinuities. Ultrasonic testing in accordance with ASTM E164 and radiographic testing to ASTM E1742 can be used to identify worm holes, voids, and lack of consolidation in the friction stir-welded material. Penetrant testing to ASTM E1417 can be used to look for LOP. Macros are useful in visually inspecting the weld for discontinuities such as discontinuities flash, joint line remnants, mismatch across the weld, and underfill discontinuities. When testing friction stir spot welds, the NASM 1312-4 REVISION 1 (2011) standard for shear testing a mechanically fastened sheet metal lap joint and NASM 1312-21 REVISION 2 (2012) for testing shear joint fatigue at constant amplitude are usually followed since there are no standards that apply specifically to FSSWs.

Statistical methods are available for evaluating the friction stir welding process. This involves determining the stability of the process by taking random products and testing them for required tolerances. In the friction stir weld, this means looking at the instances of the defects/discontinuities mentioned previously and their effect on the strength of the weld. The standards give acceptable variability tolerances for many of them, and some are specified in the certified process for the particular industry application.

Many of the discontinuities affect the strength of the weld therefore tensile testing of the weld can be done to determine the strength of the weld. Stress, strain, and fatigue testing can also be done. In order to determine what testing is required for each application the material properties and forces that will be applied to the weld when in use are taken into consideration. A statistical analysis of the mechanical testing data obtained can identify problems or trends. Unfortunately there are no allowables for friction stir welding at this time but data from current research can provide a baseline for expected static and dynamic testing results to determine if the weld is a strong defect free weld or to identify variability in the data caused by defects in the weld. Section 9 of the Metallic Materials Properties Development and Standardization (MMPDS), formerly the MIL-HDBK-5, has a detailed description of the methods that can be used for statistical analysis of test data obtained from mechanical testing.

2.4 Friction Stir Welding Process Control

2.4.1 Controlling the Process

The friction stir process is a combination of complex interactions and flow patterns which makes controlling the process difficult [6]. Studies have shown that flow around the weld tool is not symmetrical [20] , which further complicates the process. Extensive research has been conducted to identify the flow of material around the probe and the factors affecting this flow.

Understanding the flow of the weld material around the probe and boundary conditions at the edge of the stir zone is necessary to be able to control the FSW process. An early attempt to characterize the flow patterns seen in the production of dissimilar welds involved looking at the etched final product cross sections [21]. Later research involved adding markers in the weld material and mapping their movement in the weld zone [20] [22]. Colligan placed steel shotas markers in the weld and used a "stop action" step [20]. The welding was stopped mid-weld with the probe in place and the weld was radiographed to visualize the position of the markers in the weld. Seidel and Reynolds used inserts in the path of the weld [22] and progressive layers were milled from the top of the weld. Metallography at each step was used to visualize the weld material perpendicular to the direction of the weld tool path. This yielded a three-dimensional plot similar to a computer tomography (CT) scan to visualize the flow of material in the weld around the tool. Other researchers have modeled the material flow, boundary conditions, and heat production in the weld zone. In most studies, the results were then compared to experimentally obtained data. Still there was not a concensus as to the boundary conditions around the weld tool. Some have identified a sticking condition and some a slipping condition. It has been suggested that this depends on the material properties of the material being welded [23].

Colegrove and Shercliff found that the flow around the weld tool was highly cyclic. Their method used a computational fluid dynamics package to model the flow around the weld tool [24] [25]. A pattern of two boundary conditions occurring at the interface between the probe and the material was identified at different areas around the probe. The stress levels present determined which condition would ocurr at any particular location. A critical stress level was identified when stick conditions would be present, and in areas where the stress exceeded that critical level, slip conditions were present. Arbegast evaluated friction stir welding as an extrusion process, and

described complex flow patterns and thermal changes in the area of the weld tool in terms of five conventional metalworking zones [26]. As the temperature rises in front of the weld tool and strain energy is released, material begins to move upward to the shoulder area and downward to the extrusion area. As the tool advances a void is formed behind the tool as it advances forward [14], but material flow from the front into the back cavity does not occur until the temperature and stress levels rise to a critical level [26]. These critical stresses are called Gleeble flow stresses. Experimentally derived compressive Gleeble stress curves were developed and used to calculate the Gleeble flow stresses for the studied materials. The process was analyzed computationally and compared well to the experimental results.

Liechty and Webb used a fluid mechanics approach assuming a sticking constant velocity condition to model the boundary conditions [27]. Then a slipping variable shear stress model was investigated as a result of the study of the sticking constant velocity model. Experimental data obtained from visualizing the flow around the weld tool with thermocouple measurements made during the production of plasticine welds was used to validate the models. The sticking constant velocity model identified a region of material that moves with the tool and the slipping variable shear model indicated the material extrudes around the tool. The variable shear model compared better with the experimental data. Arbegast used computational fluid dynamics (CFD) to describe the conditions that cause defects in the friction stir weld [14]. He describes in detail the flow of material in the friction stir weld and the relationship between material flow and weld defects. A flow partitioned defamation zone model was used to describe the effects changes in weld parameters have on weld critical identified critical stress levels and critical isotherm levels. A flow volume pattern was identified for each defamation zone that must occur in order to avoid defects. It was suggested that the conditions needed to make a defect free weld are at a temperature where

stick-slip wiping conditions occur and that an exact balance between the amount of material being taken from the leading edge of the tool with that which is flowing into the void formed at the trailing edge of weld tool. This can be controlled by the processing parameters.

2.4.2 Current State of Development in Process Control

It is believed that the best way to control the FSW process would be to develop a real-time in-process method to avoid defects in the weld that affect the tensile strength and fatigue life. In one study, the heat generated during the friction stir welding process was investigated as a guide to monitor the quality of the weld [28]. Infrared thermography was used to map the heat generated in the weld during the welding process. Temperatures reached in the weld determine the final microstructure, and therefore strength and properties of the weld, and the weld parameters chosen determine the thermal input to the weld during the welding process. Controlling the heat input into the weld by in-process adjustments to weld parameters driven by infrared thermography monitoring of the temperatures generated could provide an in-process method of controlling the process. It was shown that the maximum temperatures reached during the process could be monitored using both thermocouples and thermal cameras in non-stationary conditions.

The cyclic flow identified by Arbegast [14] produces distinct metal flow patterns in each flow zone. Arbegast felt the cyclic nature of the flow patterns and their relationship to the process forces could provide a way to monitor weld quality in real time during the welding process [29]. Previous research by Morihara at the South Dakota School of Mines had shown a correlation between low frequency events and wormhole defects in the weld [29]. Arbegast developed algorithms to measure the weld process forces which could be used to asses the weld quality. Since weld defects are directly related to metal flow and process parameters this could potentially be used to avoid weld defects with in-process corrections to the process parameters. Resultant force

direction analysis was able to detect micro void formation. Normalized Fourier cumulative area analysis on the Y-force and Z- force was shown to be successful in detecting large volumetric defects and a small amount of lack of consolidation defects. Boldsaikhan et al. evaluated the weld by plotting the Y-feedback value on the horizontal axis against the change in Y on the vertical axis [30]. The phase space plots showed stable orbits for good welds and unstable orbits that diverged for welds with defects. High-frequency noise was present and methods were used to filter out the noise and obtain an easily read plot. Evaluating the plots was shown to be a successful method of predicting weld quality and also in determining the size of the defect. In follow-up research, a neural network was developed and successfully classified the weld [31]. No bad welds were classified as good, and this method displays the ability to provide real-time assessment of weld quality.

Another study collected acoustic emission (AE) data during the welding process for real-time detection of defects in the weld [32]. AE is the generation of transient elastic waves as the result of a material deforming under stress. Sensors can be used to record these stress waves and in this study camera images of the weld surface were captured off-line and Image Processing Toolbox of MATLAB software was used to correlate the surface condition with weld defects. The digital images of the weld surface were used to obtain the statistical histogram and Gray Level Co-occurrence Matrix (GLCM), which were used to determine the standard deviation and entropy of the images. Tensile testing of welds and X-ray radiographic examination of the welds for defects and statistical image correlations were used to validate the AE data collected during the FSW process. The AE data and statistical image variations were similar. The tensile test and radiographic evaluation of the welds were shown to agree well with the AE data. There is evidence that machine vision and AE techniques can be used in real-time assessment of FSW quality.

In a study to develop an on-line evaluation method for linear butt welds [33], an ultrasonic phased array inspection method that could be adapted for use on robotic FSW systems was developed for real-time evaluation of FSW. This inspection method was shown to be able to detect lack of penetration, lazy-S flaws, and voids of 0.1 mm with an inspection rate greater than 50 mm/s. The speed of this method is capable of being equal to the speed of the FSW process.

A system for automatic fault detection that uses a Support Vector Machine (SVM)-based method has also been studied [32]. The system would be a real-time fault detector. A learning algorithm was trained with collected frequency spectra data of the axial forces to in orderto differentiate between welds with gaps and those without. The data was randomly divided into nine bins; some were used for training and the ninth was used to test the system. Testing of this system indicated it was effective in classifying even very small gaps of 0.0002 inch with a high degree of accuracy and detecting gaps at 0.004 inch and above with perfect accuracy [32].

Industry would prefer to use robotic welding in their friction stir weld manufacturing process. Unfortunately, it is difficult to obtain welds with good quality when produced by robotic FSW methods due to difficulty in controlling the lateral movement of the tool during the process. Robot arms do not have the stiffness required to provide the Z-force needed to produce a strong defect free weld without the rotational force of the weld tool causing deflection of the robot arm. Studies have shown that if the RPM is increased, a weld can be made with a lower Z-axis force [32] but the coefficient of friction between the tool material and the weld material is a limiting factor in increasing the RPM of the spindle speed. When a certain number of rotations per minute is reached, frictional forces are inadequate to provide enough flow of material for filling, and defects will result. Research has developed methods to address this problem. The acceptable tolerance width for deflection has been shown to be one-half the diameter of the tool [34]. One

method that was studied for correcting the weld path used a laser system for in-process correcting of the weld path but it required a reference plane and only worked on straight linear welds [32]. It was capable of precision measurements though. A camera system was added to the laser system which eliminated the need for a reference plane. The modified system required controlled lighting and a visible joint line. It also could not be utilized during the plunge part of the FSW process.

Another study developed an embedded real-time algorithm, which was shown to be successful in real-time correction of the tool path [35]. A geometric description of the robot structure with closed-loops was used to develop a tree structure of the robot kinematics. From this, an elastostatic model of the robot was made and used to estimate the deflection of the tool center point. Here, a load cell sensor is placed in the FSW end effector, and force measurements during the FSW process are used with a force control algorithm to compensate for deflection in real time. This method was successful in compensating for lateral pin deviation in real time, and the weld quality compared well with welds produced by a computer numerical control (CNC) gantry type machine. Another study used both temperature control and force control to maintain the temperature below the solidus temperature and adjust for lack of stiffness in the robot [36]. Improved compliance was accomplished, although the inherent compliance of the robotic system was a limiting factor for the developed closed-loop control system.

Delays that exist in FSW robotic systems are associated with characteristics of the actuators and communication between the processor and actuators. One study used a linear-quadratic regulator (LQR) technique to design a system to address both the probe deviation problem and time delay in the robotic system [37]. The plunge depth was used to control force; therefore, the process controls used to make real-time adjustments in the welding process were spindle speed, travel speed, and plunge depth. An equation defining the nonlinear static relationship between the

axial force and the plunge depth was combined with a second-order model with pure delay to eventually arrive at a control system for the FSW process. The tracking control system included a feed-forward, stabilizing, and servo compensator. The system had high tracking accuracy, and compared to welds made with a robotic FSW system without control and which had voids, flash, and lack of penetration, the controlled joints were of good quality.

A combination of real-time evaluation methods may be needed to effectively assess the welding process and make corrections in the weld parameters. X-ray radiography and conductivity of the weld during the welding process have been mentioned as possibilities to be used in conjunction with other methods to monitor the weld quality. Research continues in this area to determine the best way to assure process quality.

2.5 Utility of FSW to Industry

Friction stir welding can be used to make welds in metals that are traditionally difficult to weld using other methods, such as 7XXX series aluminum [6] [38]. In the space program, the National Aeronautics and Space Administration (NASA) used FSW to produce the space shuttle's external fuel tanks [6] [39]. Boeing used this method to produce Delta rocket fuel tanks [6] [40] and 747-400F cargo nose barrier beams [6] [41]. Space-X and Embry Air used FSW in the design of their aircraft. Friction stir welding is useful to the space program because it can be performed in the vacuum of space. The auto industry uses FSW to incorporate aluminum alloys in the design of their automobiles for weight reduction

Friction stir welding has been successful in welding more than aluminum alloys. The two workpieces to be joined can have differences in thickness and can be of different materials [6], such as commercially pure titanium (CP-Ti) welded to 304 stainless steel [42]. Friction stir welds of AA2024 and AA7075 aluminum panels have been successfully produced [6] [38]. It has also

been shown that welds can be produced in AA6000 series material panels, AA5000 series aluminum panels [6] [43], Ti-6Al-4V alloy panels [6] [44] [45], steel [6] [46], magnesium (Mg) alloys [6] [47] [48], copper (Cu) [6] [49], composite materials [6] [50], polymers such as polypropylene [6] [51], and more. Welds have been successfully produced in advanced high-strength steels with a strength that exceeded the minimum design shear strength required by the American Welding Society for resistance spot welding of steel by as much as 150% [6] [52].

2.6 Corrosion of Friction Stir Welds

There are different types of corrosion, such as bacterial corrosion, deposit corrosion, layer corrosion, intergranular corrosion, crevice corrosion, pitting corrosion, galvanic corrosion, and more. Galvanic corrosion is one of the most common forms of corrosion and one of the most destructive [53]. The costs for cathodic and anodic protection alone to prevent galvanic corrosion in 1998 was $2.22 billion [54]. This includes materials and installation. Other measures used to combat galvanic corrosion are coatings and corrosion resistant metals. These accounted for more than $33.5 billion [54]. Therefore, galvanic corrosion is the subject of ongoing research for more effective prevention measures.

Research into galvanic corrosion and protection systems includes investigating new micro-electrochemical strategies for the study of corrosion inhibitors [55], microcells and corrosion currents in carbonated concrete [56], the effect of anodic films on the corrosion behavior of TC4 titanium (Ti) and LY12 aluminum [57], shape recovery coatings of self-healing polymers [58], modeling of zinc (Zn) and aluminum coatings [59], redox-responsive self-healing coatings for corrosion protection [60], coating defects under cathodic protection [61], corrosion protection using hot-dip aluminum-silicon (Al-Si) coatings on steel [62], the galvanic behavior of nickel-carbon (Ni-C)-filled conductive silicone rubber coupled to AZ31 magnesium alloys [63], the

galvanic response of polyacrylonitrile (PAN), and pitch-based short carbon fibers in polyetheretherketone (PEEK) composites [64]. These and many more are areas of ongoing research.

Galvanic corrosion occurs when materials of differing electrical potentials come in contact in the presence of water and oxygen (O) creating a galvanic couple [65] or galvanic cell. The process is expedited by the presence of an electrolyte such as sea water, which facilitates the flow of current. In contact with water, electrons are extracted from the less-noble anode, according to the following cathodic oxygen reduction equation:

$$O_2 + 2H_2O + 4e^- \rightarrow 4OH^- \quad (2.1))$$

The material with the higher electrode potential becomes the cathode in the galvanic cell, and the material with the lower electrode potential becomes the anode. Reduction occurs at the cathode or more noble material according to:

$$M^{m+} + me^- \rightarrow M \quad (2.2)$$

At the same time, the anode material is oxidized according to

$$M \rightarrow M^{m+} + me^- \quad (2.3)$$

where M is a metal atom on the surface, M^{m+} is an ion in solution, e^- is an electron, and m the number of electrons/ions. The galvanic couple can be between two different adjacent materials or between two sites on one material that have differing potentials due to discontinuities and flaws on the surface or changes in microstructure.

The corrosion process in the aluminum alloy involves two ionic species: $Al^{3+}$and AlO_2^-. The reversible half-cell reaction, $Al^{3+} + 3e^- \rightarrow Al$, can be related to the Nernst equation as [66]

$$E = E^0 + \frac{RT}{3F} Ln[Al^{3+}] \quad (2.4)$$

For the half-cell reaction, this equation gives the relation between its reduction potential and the Al^{3+}concentration, where E is the nonstandard half-cell reduction potential of interest, E^o is the standard half-cell reduction potential, F is Faraday's constant, R is the universal gas constant, and T is the absolute temperature [66]. The total galvanic corrosion process in the aluminum friction stir weld is depicted in Figure 2.7.

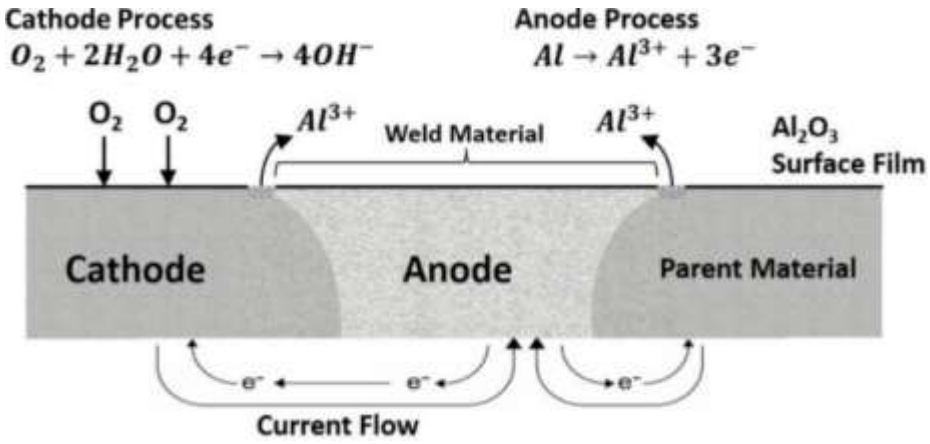

Figure 2.7. Galvanic corrosion process in linear friction stir weld of aluminum alloy.

The galvanic reaction is affected by environmental conditions such as temperature and the concentration of ion species present in the solution [66]. In aluminum alloy, this is what would determine which ion, Al^{3+}or AlO_2^-, is produced during the corrosion process, depending on whether the conditions are acidic or basic. The reactions that occur are determined by the electrochemical thermodynamics of the chemical species in the cell. The Nernst equation is derived from the standard changes in the Gibbs free energy as a result of the reactions that occur with the process. The electrode reaction for an oxidation-reduction reaction under equilibrium conditions takes the form $O + ne^- \rightarrow R$, where O is the species being oxidized, R is the species being reduced, and n is the number of electrons involved [65]. If all of the chemical species involved are in a standard state, then the standard electrode potential for the reaction is [65]

$$E^0 = -\frac{\Delta G^0}{nF} \tag{2.5}$$

where ΔG^0 is the Gibbs free energy for the reaction. This is related to the Nernst equation in its standard form as [65]

$$E = E^0 + \frac{RT}{nF} Ln\left(\frac{Ox}{Red}\right) \tag{2.6}$$

or

$$E = E^0 + \frac{RT}{nF} Ln(Q) \tag{2.7}$$

The Pourbaix diagram, also called the E-pH diagram, can be used with the electrode potential to determine if corrosion will occur, in order to predict environmental conditions that would prevent or reduce the progress of the corrosion process and what chemical species would be produced. The Pourbaix diagram for the aluminum oxidation-reduction reaction is shown in Figure 2.8.

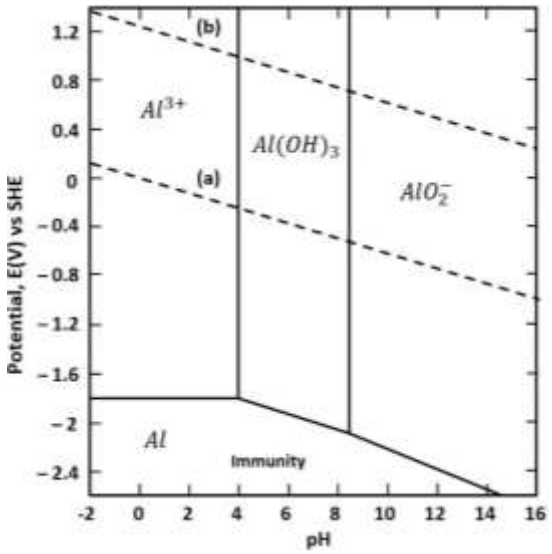

Figure 2.8. Pourbaix diagram for aluminum oxidation-reduction reaction.

The changes in the microstructure in the friction stir weld cause differing corrosion potentials between the microstructural zones and the parent material. This results in a galvanic coupling and decreased corrosion resistance in the weld, as compared to the base material. A riveted joint in the skin of the airplane joins the AA2024 skin material and the AA7075 stinger material. The FSSW configuration would be a lap joint of both of these materials. The weld would

be of dissimilar metals with differing microstructures and elemental compositions. Therefore, the corrosion mechanism is very complex and difficult to address. Research into potential corrosion protection systems for friction stir welds is ongoing to develop satisfactory methods to improve the corrosion properties of the friction stir weld for use in industry.

2.7 Corrosion Control Methods

There are numerus approaches to corrosion control in metallic materials [67]. One method of improving corrosion properties in metals is to add inclusions to the metal matrix. In one study, inclusions of ytterbium (Yb), chromium (Cr), and zirconium (Zr) were added to AA7075-T6 aluminum alloy, which is an Al-Zn-Mg-Cu alloy [68]. This approach resulted in the inhibition of recrystallization of the aluminum matrix after solution heat treatments. The additions formed 20-50 nm dispersoids with the alloy matrix, including pinning of the subgrain boundaries and retarding of their transformation to high-angle grain boundaries. The final result was a reduction in the number of η precipitates at the low angle boundaries, which were discontinuously distributed. An increased resistance to intergranular type and exfoliation type corrosion was seen as well as increased resistance to stress corrosion cracking [68].

Another method to retard corrosion is to modify the surface of the material. Kalita used a laser surface melting treatment to modify the surface of AA2024 friction stir welds in an attempt to improve the corrosion properties of the weld [69]. Laser treatments were performed on the nugget region of the FSW lengthwise to the weld in single-pass parallel-melt tracks with 0.7 mm between melt tracks. The laser melt treatment maximum melt depth was 280 μm. The melt zone was found free of S-phase secondary precipitates, and the final microstructure after the treatment was found to be fine columnar grains and columnar dendrites grown epitaxially on the unmelted substrate. A thick planar boundary with a much larger grain structure than the surrounding parent

and melt material was present from the base of the melt zone to the surface at the interface of the melt zone and unmelted material. The parent material adjacent to the melt zone displayed fine S-phase precipitates. The elemental constituents of the aluminum alloy were evenly distributed in the melt zone, but the weld zone exhibited copper-rich aluminum depleted areas corresponding to the S-phase precipitates, which are said to be responsible for the poor corrosion resistance of the friction stir weld material. The rapid melting and cooling of the laser surface melting treatment produced a fine uniform microstructure with desirable properties for corrosion resistance. An increase in the resistance to pit nucleation was seen.

Modification of the surface can create a superhydrophobic surface. Superhydrophobic surfaces are surfaces that have low surface energy and a micro-nanostructured morphology with a contact angle of 150° or more. One property of these surfaces is that a droplet of water balls up and rolls off the surface easily. Another property is that, as the droplet rolls off, it takes dirt and debris with it. These surfaces are of great interest in corrosion prevention because if the electrolyte and moisture needed for the corrosion process are prevented from reaching the substrate the surface, then this provides corrosion mitigation. Huang et al. applied superhydrophobic copper surfaces to copper and aluminum substrates by electrochemical deposition and electrochemical modification in ethanolic stearic acid to achieve a low surface energy copper stearate surface [70]. The surface was shown to have a micro-nanosized flower-like morphology with contact angles up to 157° and good roll-off properties.

Another study used laser treatment of thin aluminum sheets to create a near-superhydrophobic surface. Jagdheesh et al. modified a thin aluminum sheet of 100 μm by machining the surface with nanosecond ultraviolet laser pulses [71]. The laser-machined ~15 μm diameter blind microholes, shown in Figure 2.9, were created with multiple laser pulses in rows

with a hole spacing of 15–35 μm. The laser-processed surface was shown to have a maximum static water contact angle of 148°. The laser machining process caused piling of recast metal as a result of repeated melting as laser pulses were applied at the same spot, which created microwalls of ~3.5 μm in height at the rim of the blind microholes. The irregular top of the microwalls creates the micro-nanostructured surface morphology, which is required for a superhydrophobic surface.

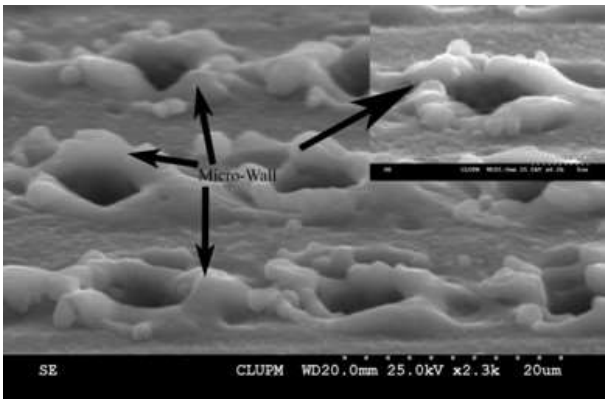

Figure 2.9. Aluminum after laser treatment of surface resulting in blind microholes.[71]

A corrosion-mitigation substance can be deposited on surfaces to increase corrosion resistance. Conversion coatings of hexavalent chromium [chromium(VI)] have been very effective in providing corrosion resistance. This coating even has self- healing properties, but due to the toxicity and carcinogenic properties of hexavalent chromium, research is ongoing to develop safer alternatives [72]. Yasakau et al. applied cerium and lanthanide deposits on the surface of AA2024 aluminum alloy [73]. The cerium and lanthanide hydroxide deposits collected in corrosion initiation sites after deposition on the surface of the material. Addition of the cerium and lanthanide inhibited the anodic and cathodic processes, but if the concentration of cerium or lanthanide is too high, it leads to deeper localized corrosion in the area of the S-phase intermetallics. Scanning Kelvin probe force microscopy (SKPFM) was used in conjunction with atomic force microscopy (AFM) to map the Volta potential on the surface during the corrosion process. It was shown that this technique could be used to optimize the concentration of the rare earth inhibitors for optimal

corrosion inhibition on the surface. There was evidence that cerium was more effective than lanthanum in corrosion inhibition, but cerium took longer to reach an effective deposition concentration on the surface than the lanthanum. Molybdenum (Mo) has also been shown to be an effective replacement for chromium and has been effective in anti-corrosion enhancement applied as a conversion coating as well as an additive in a coating/paint [72] [74].

A coating can be applied to surfaces as a method to provide corrosion mitigation. Coatings have been used widely to provide corrosion protection to metal surfaces. Polymers such as polyurethane, polyvinyl chloride, and epoxy resins are used in producing paints and other coatings [75]. In marine conditions, where seawater causes corrosion, an anodic corrosion protection system including a polymer coating and a negative mixed electrode potential is used. On the structures of the ship exposed to the marine atmosphere or where sea water spray is a constant occurrence, the anodic approach has a limited range of effectiveness, so a coating with metal powders is used [75] [76]. Polyurethane coatings with Zn and Al fillers have been shown to be more effective than other metal powder-filled polymer coatings in corrosion protection of metal substrates [75]. Kutyreva et al. studied the effectiveness of the coatings with metal filler and those without metal filler [76]. This study also compared the effectiveness of anodizing the surface to an approach called microplasmas oxidizing (MPO). This technique is outlined in the *Handbook on Anodic Treatment* [77]. The study compared polymer coatings applied after an anodizing process, with a liquid glass (SiO_2) coating applied by the MPO process [76]. The polymer and SiO_2 coatings were applied with and without added metal fillers. After application, the SiO_2 coating was filled with a polymer mixture of 1/4 polyurethane + 3/4 butylacetate to improve the corrosion-resistant properties of the coating, and metal fillers were added to the polymer. The coatings were corrosion tested in a salt spray chamber and electrochemically tested in a 3% NaCl solution. Results revealed significantly

improved corrosion resistance with the SiO_2 coating compared to the coatings of just polymer or polymer with metal filler. The SiO_2 coating with Al and Zn filler showed higher corrosion resistance than either of the polymer coatings and better corrosion resistance properties than the SiO_2 coating without metal fillers.

The coating is a passive form of protection by shielding the surface of the substrate from agents that cause the corrosion process, but if the coating becomes damaged this protection could be lost. Borisova et al. added nanoparticles to a sol-gel coating to provide active corrosion mitigation for aluminum alloys [78]. Mesoporous silica nanoparticles were loaded with 1H-benzotriazole (BTA) to be released in response to the alkaline or acidic pH changes that occur with the corrosion process. The nanocontainers were added to a silica zirconia film matrix. The mesoporous silica particles and BTA inhibitor have the same charge outside the neutral pH range. This would cause them to repel and trigger the release of the BTA from the silica matrix. The changes in pH during the corrosion process would cause the release of the BTA inhibitor, which in turn would form a passive layer, consisting of a complex between copper and BTA, in response to contact with the aluminum substrate. Scanning electron microscopy (SEM) and scanning vibrating electrode technique (SVET) measurements have indicated that the coating functioned as was intended and provided corrosion mitigation as well as the added self-healing properties provided by the release of the BTA.

2.8 Conclusions

Corrosion is a problem in the friction stir weld. There are many potential approaches to addressing this problem. In this paper, the use of a superhydrophobic coating for corrosion protection will be investigated. The development of a superhydrophobic coating for protection of aluminum alloys will be presented, and the superhydrophobic coating will be evaluated for

effectiveness in corrosion mitigation in the aluminum alloy. The coating will be evaluated by electrochemical corrosion testing and characterized as to static water contact angle (WCA), sliding angle (SA), and contact angle hysteresis (CAH). The durability and adhesion of the coating to the substrate will also be evaluated. The superhydrophobic coating will be applied to dissimilar friction stir spot welds of 0.05-inch AA2024-T3 and 0.04-inch AA7074-T6 aluminum alloy and evaluated for corrosion mitigation. Corrosion results for coated welds will be compared to corrosion results for bare welds, bare AA2024 and bare AA7075 specimens.

2.9 References for Chapter 2

[1] W. M. Thomas, E. D. Nicholas, J. C. Needham, M. G. Murch, P. Temple-Smith, and C. J. Dawes, "Friction Stir Butt Welding," Great Britain Patent 9125978.8, June 12, 1991.

[2] W. M. Thomas, E. D. Nicholas, J. C. Needham, M. G. Murch, P. Temple-Smith, and C. J. Dawes, "Improvements to Friction Stir Welding," Intenational Patent PCT/GB92/02203, August 11, 1995.

[3] W. M. Thomas, E. D. Nicholas, J. C. Needham, M. G. Murch, P. Temple-Smith, and C. J. Dawes, "Friction Welding," United States Patent 5,460,317, October 24, 1995.

[4] C. A. Widener, D. A. Burford, and S. F. Jurak, "Effects of Tool Design And Friction Stir Welding Parameters On Weld," *Materials Science Forum*, vols. 638-642, pp. 1261-1266, 2010.

[5] C. Widener, B. Tweedy, and D. Burford, "Path independence of allowables based friction stir butt welds," in *Collection of Technical Papers—7th AIAA Aviation Technology, Integration, and Operations Conference*, Belfast, Ireland, September 10-20, 2007.

[6] S. F. Jurak, "Statistical Analysis of the Mechanical Properties of Friction Stir Welds in 2024 and 2198 Aluminum Alloys," Master's Thesis, Wichita, State University, Wichita, KS, 2010.

[7] K. Kumar and S. V. Kailas, "The Role of Friction Stir Welding Tool on Material Flow and Weld Formation," *Materials Science and Engineering A*, vol. 485, no. 1-2, pp. 367-374, June 25, 2008.

[8] A. Reynolds, W. Tang, J. Khan, and K. Lindner, "Relationships between Weld Parameters, Hardness Distribution and Temperature History in Alloy 7050 Friction Stir Welds," *Science and Technology of Welding and Joining*, vol. 2, no. 9, pp. 190-199, 2005.

[9] J. Q. Su, T. W. Nelson, R. Mishra, and M. Mahoney, "Microstructural Investigation of Friction Stir Welded 7050-T651 Aluminium," *Acta Materialia*, vol. 51, no. 3, pp. 713-729, February 7, 2003.

[10] C. A. Widener, D. A. Burford, and S. F. Jurak, "Effects of Tool Design and Friction Stir Welding Parameters on Weld Morphology in Aluminum Alloys," *Materials Science Forum*, vols. 638-642, pp. 1261-1266, 2010.

[11] C. Genevois, A. Deschamps, A. Denquin, and B. Boisneau-Cottignies, "Quantitative Investigation of Precipitation and Mechanical Behaviour for AA2024 Friction Ftir Welds," *Acta Materiala*, vol. 53, no. 8, pp. 2447-2458, April 2005.

[12] C. S. Paglia and R. G. Buchheit, "A Look in the Corrosion of Aluminum Alloy Friction Stir Welds," *Scripta Materialia*, vol. 58, no. 5, p. 383-387, 2008.

[13] C. G. Rhodes, M. W. Mahoney, W. H. Bingel, R. A. Spurling, and C. C. Bampton, "Effects of Friction Stir Welding on Microstructure of 7075 Aluminum," *ScriDta Materialia*, vol. 36, no. 1, pp. 69-75, 1997.

[14] W. J. Arbegast, "A Flow-Partitioned Deformation Zone Model for Defect Formation During Friction Stir Welding," *Scripta Materialia*, vol. 58, no. 5, pp. 372-376, March 2008.

[15] T. Vugrin , M. Schmücker, and G. Staniek, "Root Flaws of Friction Stir Welds," in *Friction Stir Welding and Processing III—Proceedings of a Symposium Sponsored by the Shaping and Forming Committee of (MPMD) of the Minerals, Metals and Materials Society, TMS*, San Francisco, CA, 2005.

[16] C. Zhou, "Effect of Oxide Array on Fatigue in FSW 2024," *Scripta Materialia*, vol. 54, pp. 1515-1520, 2006.

[17] A. Oosterkamp, L. . D. Oosterkamp, and . A. Nordeide, ""Kissing Bond' Phenomena in Solid-State Welds of Aluminum Alloys," *Welding Journal*, vol. 83, no. 8, pp. 225–S-231-S, August 2004.

[18] AWS D17 Committee on Welding in the Aerospace Industry, *AWS D17.3/D17.3M:2010 Specification for Friction Stir Welding of Aluminum Alloys for Aerospace Applications*, American Welding Society, July 1, 2009.

[19] M. Wang, H. Zhang, J. Zhang, X. Zhang, and L. Yang, "Effect of Pin Length on Hook Size and Joint Properties in Friction Stir Lap Welding of 7B04 Aluminum Alloy," *Journal of Materials Engineering and Performance*, vol. 23, no. 5, pp. 1881-1886, May 2014.

[20] K. Colligan, "Material Flow Behavior During Friction Stir Welding of Aluminum," *Welding Journal*, vol. 78, no. 7, pp. 229-s–237-s, July 1999.

[21] Y. Li, L. E. Murr, and J. C. McClure, "Solid-State Flow Visualization in the Friction Stir Welding of 2024 Al to 6061 Al," *Scripta Materialia*, vol. 40, no. 9, pp. 1041-1046, 1999.

[22] T. U. Seidel and A. P. Reynolds, "Visualization of the Material Flow in AA2195 Friction-Stir Welds Using a Marker Insert Technique," *Metallurgical and Materials Transactions A*, vol. 32A, no. 11, pp. 2879-2884, November 2001.

[23] A. Gerlich, M. Yamamoto, and T. H. North, "Strain Rates and Grain Growth in Al 5754 and Al 6061 Friction Stir Spot Welds," *Metallurgical and Materials Transactions A*, vol. 38A, no. 6, pp. 1291-1302, June 2007.

[24] P. Colegrove and H. Shercliff, "2-Dimensional CFD Modeling of Flow Round Profiled FSW Tooling," in *Friction Stir Welding and Processing II*, San Diego, CA, March 2-6, 2003.

[25] P. Colegrove and H. Shercliff, "Development of Trivex Frictionstir Welding Tool Part 2: 3-Dimensional Flow Modelling," *Science and Technology of Welding and Joining*, vol. 9, no. 4, pp. 352-361, 2004.

[26] W. J. Arbegast, "Modeling Friction Stir Joining as a Metalworking Process," in *Hot Deformation of Alluminum Alloys III*, San Diego, CA, March 2–6, 2003.

[27] B. C. Liechty and B. W. Webb, "Modeling the Frictional Boundary Condition in Friction Stir Welding," *International Journal of Machine Tools and Manufacture*, vol. 48, no. 12-13, pp. 1474-1485, October 2008.

[28] L. M. Serio, D. Palumbo, U. Galietti, L. A. De Filippis and A. D. Ludovico, "Monitoring of the Friction Stir Welding Process by Means of Thermography," *Nondestructive Testing and Evaluation*, vol. 31, no. 4, pp. 371-383, 2016.

[29] W. J. Arbegast, "Using Process Forces as a Statistical Process Control Tool for Friction Stir Welds," in *Friction Stir Processing III*, San Francisco, CA, February 13-17, 2005.

[30] E. Boldsaikhan, E. Corwin, A. Logar, J. McGough, and W. Arbegast, "Phase Space Analysis of Friction Stir Weld Quality," in *4th Symposium on Friction Stir Welding and Processing*, Orlando, FL, February 25, 2007–March 1, 2007.

[31] E. Boldsaikhan, E. M. Corwin, A. M. Logar, and W. J. Arbegast, "The Use of Neural Network and Discrete Fourier Transform for Real-Time Evaluation of Friction Stir Welding," *Applied Soft Computing*, vol. 11, no. 8, p. 4839-4846, 2011.

[32] R. Rajashekar and B. M. Rajaprakash, "Development of a Model for Friction Stir Weld Quality Assessment Using Machine Vision and Acoustic Emission Techniques," *Journal of Materials Processing Technology*, vol. 229, pp. 265-274, March 1, 2016.

[33] C. R. Bird, "Ultrasonic Phased Array Inspection Technology for the Evaluation of Friction Stir Welds," *Insight—Non-Destructive Testing and Condition Monitoring*, vol. 46, no. 1, pp. 31-36, 2004.

[34] H. Takahara, Y. Motoyama, M. Tsujikaw, S. Oki, S. W. Chung, and K. Higashi, "Allowance of Deviation and Gap in Butt Joint on Friction Stir Welding," in *5th International Conference on Processing and Manufacturing of Advanced Materials—THERMEC 2006*, Vancouver, BC, Canada, July 4-8, 2006.

[35] M. Guillo and L. Dubourg, "Impact & Improvement of Tool Deviation in Friction Stir Welding: Weld Quality and Real-Time Compensation on an Industrial Robot," *Robotics and Computer-Integrated Manufacturing*, vol. 39, p. 22-31, June 1, 2016.

[36] A. Fehrenbacher, C. B. Smith, N. A. Duffie, N. J. Ferrier, F. E. Pfefferkorn, and M. R. Zinn, "Combined Temperature and Force Control for Robotic Friction Stir Welding," *ASME Journal of Manufacturing Science and Engineering*, vol. 136, no. 2, pp. 021007-1–021007-15, 2014.

[37] S. Zhao, Q. Bi, and Y. Wang, "An Axial Force Controller with Delay Compensation for the Friction Stir Welding Process," *The International Journal of Advanced Manufacturing Technology*, vol. 85, no. 9-12, p. 2623-2638, 2016.

[38] A. Reynolds, W. Tang, J. Khan, and K. Lindner, "Relationships between weld Parameters, Hardness Distribution and Temperature History in Alloy 7050 Friction Stir Welds," *Science and Technology of Welding and Joining*, vol. 2, no. 9, pp. 190-199, 2005.

[39] "NASA's Marshall Center," [Online]. Available: http://www.nasa.gov/centers/marshall/pdf/104835main_friction.pdf. [Accessed 10 May 2011].

[40] "Boeing IDS," Boeing, [Online]. Available: http://www.boeing.com/companyoffices/gallery/images/space/delta_iv/d4_mfg_06.html. [Accessed 10 May 2011].

[41] D. A. Burford, "Friction Stir Welding of Airframe Structure: From One Delivery System to Another," *SAE 2003 Transactions, Journal of Aerospace*, vol. 112, no. 1, pp. 295-300.

[42] M. Fazel-Najafabadi, S. F. Kashani-Bozorg, and A. Zarei-Hanzak, "Joining of CP-Ti to 304 Stainless Steel Using Friction Stir Welding Technique," *Materials and Design*, vol. 31, no. 10, pp. 4800-4807, December 2010.

[43] S. K. Sahoo, I. Samajdar, G. K. Dey, and K. Bhanumurthy, "Microstructure and Microtextural Studies of Friction Stir Welded Aluminium Alloy 5052," *Materials and Design*, vol. 32, no. 3, pp. 1657-1666, March 2011.

[44] S. Mironov, Y. Zhang, Y. Sato, and H. Kokawa, "Development of Grain Structure in b-Phase Field during Friction Stir Welding of Ti-6Al-4V Alloy," *Scripta Materialia*, vol. 59, no. 1, pp. 27-30, July 2008.

[45] A. J. Ramirez and M. C. Juhas, "Microstructural Evolution in Ti-6Al-4V Friction Stir Welds," *Materials Science Forum*, vols. 426-432, no. 4, pp. 2999-3004, 2003.

[46] H. Fujii, R. Ueji, Y. Takada, H. Kitahara, N. Tsuji, K. Nakata, and K. Nogi, "Friction Stir Welding Of Ultrafine Grained Interstitial Free Steels," *Materials Transactions*, vol. 47, no. 1, pp. 239-242, January 2006.

[47] W.-S. Chang, H.-J. Kim, J.-S. Noh, and H.-S. Bang, "The Evaluation of Weldability for AZ31B-H24 and AZ91C-F Mg Alloys in Friction Stir Welding," *Key Engineering Materials*, vols. 321-323, no. 2006, pp. 1723-1728, 2006.

[48] N. Afrin, D. Chen, X. Cao, and M. Jahazi, "Microstructure and Tensile Properties of Friction Stir Welded AZ31B Magnesium Alloy," *Materials Science and Engineering A*, vol. 472, no. 1-2, pp. 179-186, January 15, 2008.

[49] W. M. Thomas, C. S. Weisner, D. G. Staines, and I. M. Norris, "Friction stir Welding Technology—Preliminary Studies of Variant Techniques—Part 1," *Welding and Cutting*, vol. 5, no. 6, pp. 339-344, 2006.

[50] Z. Qin, C. Li, H. Zhang, Z. Wang, Z. Hu, and Z. Liu, "Friction Stir Welding of Zr55Al10Ni5Cu30 Bulk Metallic Glass to Crystalline Aluminum," *Journal of Materials Science and Technology*, vol. 25, no. 6, pp. 853-856, Novenber 2009.

[51] Z. Kiss and T. Czigány, "Applicability of Friction Stir Welding in Polymeric Materials," *Periodica Polytechnica, Mechanical Engineering*, vol. 51, no. 1, pp. 15-18, 2007.

[52] J. Rodelas, R. S. Mishra, G. Hilmas, and W. Yuan, "Mechanical Evaluation of Friction Stir Spot Welded Advanced High Strength Steels," in *TMS 2009 Annual Meeting and Exhibition*, San Francisco, CA, 2009.

[53] F. Mansfeld, "Galvanic Corrosion of Al Alloys," *Materials and Corrosion*, vol. 25, no. 8, pp. 578-586, January 1, 1974.

[54] NACE International, "Corrosion Costs and Preventive Strategies in the United States," Houston, TX, 2002.

[55] J. Izquierdo, L. Nagy, J. J. Santana, G. Nagy, and R. M. Souto, "A Novel Microelectrochemical Strategy for the Study of Corrosion Inhibitors Employing the Scanning Vibrating Electrode Technique and Dual Potentiometric/Amperometric Operation in Scanning Electrochemical Microscopy," *Electrochimica Acta*, vol. 58, pp. 707-716, December 2011.

[56] A. Castel and A. Nasser, "Microcell Versus Galvanic Corrosion Currents in Carbonated Concrete," *Magazine of Concrete Research*, vol. 66, no. 11, pp. 697-707, 2014.

[57] Z. Y. Wu, X. Y. Li, L. N. Zhao, and S. R. Hu, "Effect of Anodic Films on the Galvanic Corrosion Behavior of TC4 Titanium and LY12 Aluminum," *Advanced Materials Research*, vols. 998-999, pp. 39-42, July 2014.

[58] A. Lutz, O. van den Berg, J. Van Damme, K. Verheyen, E. Bauters, I. De Graeve, F. E. Du Prez, and H. Terryn, "A Shape-Recovery Polymer Coating for the Corrosion Protection of Metallic Surfaces," *ACS Applied Materials and Interfaces*, vol. 7, no. 1, pp. 175-183, 2015.

[59] S. R. Cross, S. Gollapudi, and C. A. Schuh, "Validated Numerical Modeling of Galvanic Corrosion of Zinc and Aluminum Coatings," *Corrosion Science*, vol. 88, pp. 226-233, November 2014.

[60] D. Crespy and M. Rohwerder, "Redox-Responsive Self-Healing for Corrosion Protection," *Advances Materials*, vol. 25, p. 6980-6984, 2013.

[61] C. F. Dong, A. Q. Fu, X. G. Li, and Y. F. Cheng, "Localized EIS Characterization of Corrosion of Steel at Coating Defects Under Cathodic Protection," *Electrochimica Acta*, vol. 54, pp. 628-633, 2008.

[62] I. De Graeve, I. Schoukens, A. Lanzutti, J. De Strycker, L. Fedrizzi, H. Terryn, and A. Alvarez-Pampliega, “Mechanism of Corrosion Protection of Hot-Dip Aluminium-Silicon Coatings on Steel Studied by Electrochemical Depth Profiling,” *Corrosion Science*, vol. 76, pp. 325-336, 2013.

[63] H. Zhou, Z. D. Xia, Z. Li, and F. Guo, “Galvanic Corrosion Behavior of Ni-C Filled Conductive Silicone Rubber Coupled to AZ31 Magnesium Alloys,” *Materials and Corrosion*, vol. 64, no. 12, pp. 1121-1126, 2013.

[64] A. Gebhard, T. Bayerl, and A. K. Schlarb, “Galvanic Corrosion of Polyacrylnitrile (PAN) and Pitch Based Short Carbon Fibers in Polyetheretherketone (PEEK) Composites,” *Corrosion Science*, vol. 51, no. 11, p. 2524-2528, 2009.

[65] J. W. Oldfield, “Electrochemical Theory of Galvanic Corrosion,” *ASTM Special Technical Publication*, vol. STP, no. 978, pp. 5-22, 1988.

[66] Y. Tan, “Homogeneous Electrode Models and Uniform Corrosion Measurements,” in *Heterogeneous Electrode Processes and Localized Corrosion*, R. W. Revie, Ed., Hoboken, NJ: John Wiley & Sons, Inc., 2013, pp. 1-35.

[67] R. Asmatulu, "Nanocoatings for corrosion protection of aerospace alloys," in *Corrosion Protection and Control using Nanomaterials*, V. S. Saji and R. Cook, Eds., Woodhead Publishing, 2012, pp. 357-375.

[68] K. H. Chen, H. C. Fang, Z. Zhang, X. Chen, and G. Liu, “Effect of Yb, Cr, and Zr Additions on Recrystallization and Corrosion Resistance of Al-Zn-Mg-Cu Alloys,” *Materials Science and Engineering: A*, vol. 497, no. 1-2, pp. 426-431, 2008.

[69] S. J. Kalita, “Microstructure and Corrosion Properties of Diode Laser Melted Friction Stir Weld of Aluminum Alloy 2024 T351,” *Applied Surface Science*, vol. 257, no. 9, pp. 3985-3997, 2011.

[70] Y. Huang, D. K. Sarkar and X.-G. Chen, “Preparation of Nanostructured Superhydrophobic Copperand Aluminum Surfaces,” *Nano-Micro Letters*, vol. 3, no. 3, pp. 160-165, 2011.

[71] R. Jagdheesh, J. J. García-Ballesteros, and J. L. Oca˜na, “One-Step Fabrication of Near Superhydrophobic Aluminum Surface by Nanosecond Laser Ablation,” *Applied Surface Science*, vol. 374, pp. 2-11, 30 June 2016.

[72] J. S. Warner, S. Kim, and R. P. Gangloff, “Molybdate Inhibition of Environmental Fatigue Crack Propagation in Al-Zn-Mg-Cu,” *International Journal of Fatigue*, vol. 31, no. 11-12, pp. 1952-1965, 2009.

[73] K. A. Yasakau, M. L. Zheludkevich, S. V. Lamaka, and M. G. S. Ferreira, “Mechanism of Corrosion Inhibition of AA2024 by Rare-Earth Compounds,” *The Journal of Physical Chemistry B*, vol. 110, no. 11, p. 5515-5528, 2006.

[74] T. Hájková and A. Kalendova, “Corrosion—Inhibiting Properties of Molybdenum-Containing Pigments in Coatings,” *Anti-Corrosion Methods and Materials*, vol. 63, no. 1, pp. 14-28, 2016.

[75] V. S. Sinyavskii and V. D. Kalinin, “Marine Corrosion and Protection of Aluminum Alloys According to Their Composition and Structure,” *Protection of Metals*, vol. 41, no. 4, pp. 317-328, 2005.

[76] E. N. Kutyreva, A. V. Dub, and A. G. Rakoch, “Cyclic Durability of D16T alloy Covered with Anodic and Microplasmous Coatings,” *Protection of Metals and Physical Chemistry of Surfaces*, vol. 45, p. 829, December 2009.

[77] E. E. Aver’yanov, *Handbook on Anodic Treatment*, Moscow: Mashinostroenie, 1988.

[78] D. Borisova, H. Möhwald, and D. G. Shchukin, “Mesoporous Silica Nanoparticles for Active Corrosion Protection,” *American Chemical Society (ACS) Nano*, vol. 5, no. 3, pp. 1939-1946, 2011.

CHAPTER 3

NANOSCALE SUPERHYDROPHOBIC COATINGS FOR CORROSION MITIGATION

3.0 Abstract

Superhydrophobic coatings have numerous applications from windshields to textiles, due to their repellent, corrosion, deicing, and self-cleaning properties. Superhydrophobic coatings are defined as those that have contact angles greater than 150°, but the sliding angle of the surface should be less than 10°, and hysteresis between advancing and receding angles should be very low. This surface will exhibit the so-called "lotus effect" where the water bounces and balls up when hitting the solid surface. The water droplet will run off readily, taking dirt and debris with it for a self-cleaning effect. The chemical composition of the surface has an effect on the contact angle, which can bring the water contact angle up to 120° but to achieve the > 150° WCA, an additional microstructural component is needed, which is a micro-nanostructure hierarchical morphology as seen in nature with the lotus plant. The superhydrophobic coating has promise to provide corrosion mitigation by blocking the oxygen and electrolytes needed for corrosion initiation from reaching the surface of the metallic substrates. Methods for preparing superhydrophobic coatings include sol-gel processing, layer-by-layer assembly, etching, lithography, chemical and electrochemical depositions and chemical vapor deposition, electrospinning, hydrothermal synthesis, and one-pot reactions. In this study, some of the research to develop robust and durable superhydrophobic coatings were discussed and analyzed for possible corrosion mitigation on the surfaces of metals and alloys. Readers such as scientists, engineers, students, and other participants in corrosion and coating technologies will greatly benefit from this work.

3.1 Introduction

3.1.1 General Background

Extensive research has been performed on superhydrophobic materials and coatings, and there have been promising results for corrosion resistance, as well as water repellent, anti-icing and self-cleaning applications [1]. Since the corrosion process requires oxygen for oxidation and an electrolyte, which can be provided by water/moisture, if the surface is protected by a superhydrophobic coating to prevent moisture and oxygen from reaching it, then corrosion is basically mitigated [1] [2]. The biggest problem is to design a coating that has the durability and robustness required to maintain its corrosion resistant properties over time. The coating should also be feasible relative to cost and the use of harsh chemicals in order for industry to implement them in their production processes to improve the corrosion resistance of their products. Many approaches have been used to produce the superhydrophobic coating, but few have been productionized for these reasons [1] [2] [3].

In designing a superhydrophobic coating, it is necessary to first understand the mechanism of superhydrophobicity. Many examples of superhydrophobicity occur naturally, such as the lotus leaf and the water glider. It was the study of examples in nature that piqued the interest of researchers and resulted in the design of superhydrophobic coatings. There has been extensive research into the superhydrophobic properties of plants [1] [2] [3]. Of all the plants exhibiting superhydrophobic properties, the design of the lotus leaf offers the most ideal model to date. The lotus plant retains its superhydrophobicity even under moisture condensation conditions [1] [2]. The stability of the lotus leaf water repellence resulted in the term ‘‘lotus effect’’ to describe superhydrophobic properties of the surfaces. These properties are the result of nanostructured roughness of the surfaces of the lotus plant and epicuticular wax crystalloids on the surface [1] [4].

Water droplets bead up and run off the surfae of the lotus leaf leaving a dry surface behind. A secondary benefit is that the water droplet takes particles of dust and dirt with it as it rolls off producing a self-cleaning effect.

3.1.2 Mechanism of Superhydrophobicity

The superhydrophobic properties of a coating depend on surface energy and surface morphology. It has been shown that the chemical composition of the surface has a substantial influence on surface energy [1] [5]. The surface molecules are bonded with fewer other molecules than in the interior, so there is more energy at the surface. The surface energy of a solid is the difference in energy state at the surface compared to the bulk interior or the amount of energy required in creating a unit area of surface. When a drop of liquid is placed on a solid surface, an equilibrium energy state will be reached between the three phase interfaces (liquid, solid, and gas). The three-phase interface is shown in Figure 3.1.

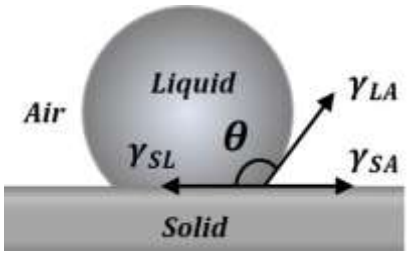

Figure 3.1. Representation of forces at three-phase interface between water droplet and solid surface [1].

In Figure 3.1, γ_{SL} is the solid-liquid interfacial energy, γ_{LA} is the liquid-air interfacial energy, and γ_{SA} is the solid-air interfacial energy. The interface here is with air but it is the same with any gas. The angle θ_0 is the characteristic angle achieved between the liquid surface and solid surface when the equilibrium state is reached. The equilibrium contact angle relates to surface energy according to the Young's equation [4]:

$$\cos\theta_0 = \frac{(\gamma_{SA}-\gamma_{SL})}{\gamma_{LA}} \tag{3.1}$$

Equation (3.1) is only valid with a smooth flat surface. The equilibrium contact angle θ_0 is a measure of the wettability of the surface. For a contact angle, less than 90°, the material is said to be hydrophilic, and for materials with contact angles greater than 90°, the material is said to be hydrophobic. A contact angle greater than 150° is considered superhydrophobic. When the contact angle is less than 10°, the surface is said to be superhydrophilic [4]. This relationship is shown in Figure 3.2.

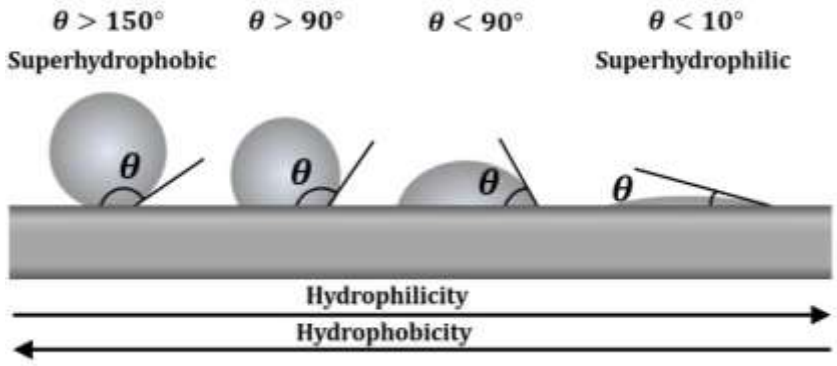

Figure 3.2. Wetting of water droplet on surface showing progression of contact angle from superhydrophobicity to superhydrophilicity [1].

The contact angle is an indication of superhydrophobicity or superhydrophilicity, but the angle at which a droplet rolls off a surface when tilted, the sliding angle, is related to the surface energy that has to be overcome for the initiation of movement. A droplet that is pinned to the surface due to local adhesion energy as in the case of hydrophilicity will not start rolling without energy input, i.e., mechanical energy, due to adhesion to the surface at the contact line. Even superhydrophobic surfaces have some adhesion at the contact line, which can, if great enough, result in hysteresis between the advancing and receding contact angles. The contact angle hysteresis is an indication of the tendency of a droplet to bounce and bead when dropped on the

surface and the ability of a droplet to roll off the surface easily. This affects the self-cleaning property of the surface.

Two models describe the interface with a roughened surface. The first model is the Wenzel model where the rough surface allows the droplet to stay in contact with the surface between the asperities thus increasing the surface area [1] [6] [7]. The Wenzel equation is:

$$cos\,\theta_w = r\frac{(\gamma_{SA}-\gamma_{SL})}{\gamma_{LA}} = r\,cos\,\theta_0 \tag{3.2}$$

where θ_w is the angle for the Wenzel model, which would be greater than for the Young's equation because r is greater than 1. The r is a roughness factor to adjust for the roughness of the surface which results in an increase in surface area and:

$$r = \frac{Actual\ roughened\ surface\ area}{Planar\ surface\ area} \tag{3.3}$$

In the Cassie-Baxter model, the asperities are high enough to prevent the droplet from touching the surface between asperities, resulting in the droplet being suspended on air trapped between the asperities. Therefore, the droplet is now resting on a heterogeneous surface comprised of a fraction of air and a fraction of solid surface. Cassie and Baxter developed an equation for the equilibrium angle on a porous solid using surface energy equations and the Young's equation. The Cassie-Baxter equation is as follows [1] [8]:

$$\cos\theta_{CB} = f_1\cos\theta_0 - f_2 \tag{3.4}$$

The Wenzel state is a sticky surface due to the increased surface area in contact with the droplet. The Cassie-Baxter state has low solid surface contact with the water droplet, which creates a slippery hydrophobic surface due to low surface energy. The Cassie-Baxter model combined with a micro-nanostructured hierarchical morphology allows a superhydrophobic surface with low

hysteresis [9] and a low sliding angle to be achieved. These states are shown in Figure 3.3 [6] [7] [8].

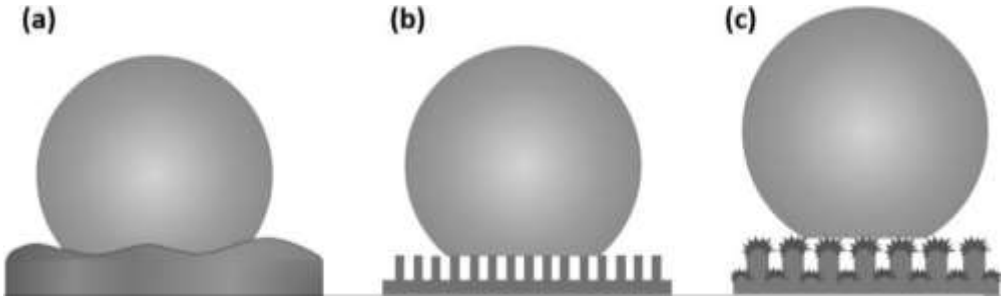

Figure 3.3. Water droplet in various states: (a) Wenzel state, (b) Cassie-Baxter state, and (c) micro -nanostructured hierarchical surface morphology [1].

3.2 Evaluation of Superhydrophobic Coatings

In characterizing the superhydrophobic properties of a coating, the static contact angle is measured and the sliding angle s determined. A water contact angle > 150° with an SA of < 10 indicates the coating has a superhydrophobic surface [10]. Contact angle hysteresis is the difference between the advancing and receding angles. The advancing angle can be measured by injecting added water into a stable droplet on a surface until just before the droplet expands outward on the surface. This is when the contact angle no longer increases with added water. The receding angle is then measured in a similar manner as water is removed from the droplet [1] [11]. The dynamic CAH is measured as the droplet sits on an inclined surface. As the surface incline is increased, measurement is taken just before the droplet begins to roll. The high WCA with low CAH is responsible for the self-cleaning property of superhydrophobic surfaces [1] [4]. Therefore, the WCA > 150° with low CAH, typically < 5°–10º, and an SA < 10° shows good superhydrophobic properties.

The area of liquid-air interface under the water droplet, the f_2 in equation (3.4), is an indication of degree of superhydrophobicity. This area fraction can be calculated under the

assumption that $f_1 + f_2 = 1$. Then the flat surface of the untreated substrate can provide the angle θ_0. Some disagree about the proper use of equation (3.4). It has been said that there is an inherent error of ~3° to 13° involved with the use of the commonly used form of the Cassie-Baxter equation [1] [12], where $f_1 + f_2 = 1$ are substituted into equation (3.4). From the Cassie and Baxter study [8], θ_1 would be defined as the contact angle to the smooth surface of the Young's equation, f_1 would be the total area of solid-liquid interface under the droplet, and f_2 would be the total area of liquid-air interface, which is a plane parallel to the roughened surface. The suggested error is said to be due to the fact that the commonly used equation is only valid for flat-topped uniformly shaped and spaced asperities where no liquid penetrates the asperities and contacts with the angled surfaces of the trough. There have been proposed methods to address this which will not be addressed here [12] [13] [14].

Since it is important that a corrosion-mitigating surface be robust and durable for use in industry [1], testing of how the coating stands up to ultraviolet (UV) exposure and exposure to atmospheric conditions can be performed. Tape testing according to ASTM D3359-17 of the surface can evaluate adherence of the coating to the substrate. Durability of the superhydrophobic properties can be analyzed by comparing the WCA during corrosion testing and after the tape has been applied and removed from the surface. Abrasion tests can be performed on the surfaces as well. The morphology of the surface can be characterized, and the elemental constituents can be determined. The elemental composition as well as their chemical and electronic state can be evaluated by X-ray photoelectron spectroscopy (XPS), the surface morphology and constituent dispersion can be identified by scanning electron microscopy, and the topographical morphology, such as surface roughness, can be analyzed by atomic force microscopy. The surface functional groups can be identified by Fourier transform infrared spectroscopy (FTIR).

It is known that superhydrophobic coatings can lose their superhydrophobicity properties. In general, damage to the coating surface is mostly responsible for this loss. Some common causes are high chloride exposure, low pH exposure, and exposure to high temperatures and UV light [1] [4]. The coating should be evaluated in solvents, in basic and in acidic solutions for stability. Thermal stability should also be evaluated. This can be accomplished by annealing coating specimens at different temperatures and then comparing the WCA of the coating for different annealing temperatures [1] [15] to determine the range where the coating has a stable WCA. The WCA decreases over time as the temperature is increased.

The corrosion resistance of the superhydrophobic coating can be determined by performing electrochemical corrosion testing [1] [16] [17] [18]. Comparing the corrosion resistance of the bare substrate to testing of the coating on the substrate can verify and quantify the corrosion mitigation of the coating. Many studies have evaluated the corrosion resistance of the coating that was developed by obtaining potentiodynamic polarization curves and calculating the polarization resistance (R_p) as [1] [19]

$$R_p = \frac{\beta_a \beta_c}{2.303(\beta_{a+}\beta_c) i_{Corr}} \tag{3.5}$$

and protection efficiency by [1] [19]

$$\boldsymbol{\eta} = \frac{i_1 - i_2}{i_1} \times 100\% \tag{3.6}$$

This information is very useful in evaluating the corrosion resistance of a coating. Coatings that have lower i_{corr} and higher E_{corr} values compared to the substrate can be effective in mitigating corrosion of the substrate. A higher R_p corresponds to a better corrosion resistance. Some studies choose to evaluate the effect of UV irradiation, submersion in acids, and submersion in solvents on the developed coating to determine the stability of the coating [1] [11] and not include the corrosion resistance.

3.3 Fabricating Superhydrophobic Coatings

The use of low surface energy (hydrophobic) materials such as fluoropolymeric materials or silanes in a coating to chemically create a low energy surface on a substrate can bring the WCA up to 120^o but to get to the extremes of $> 150^o$, an ingredient must be added to modify the surface structure [1] [20]. Therefore, nanoparticles are used to create a micro-nanostructured surface. Numerous methods that have been used to produce a superhydrophobic coating. These methods include sol-gel processing, layer-by-layer assembly, etching, lithography, chemical and electrochemical depositions and chemical vapor deposition, sublimation, plasma deposition, electrospinning, hydrothermal synthesis, and one-pot reactions. Coatings are applied to achieve the micro-nanostructured hierarchical morphology on the surface of the substrate and are bonded via covalent linkages between the organic layer and aluminum substrate. On the other hand, etching directly modifies the surface of the substrate by removing individual atoms to obtain the desired roughened morphology [1] [4].

The method selected to apply the coating to the substrate is dependent on the materials chosen to create the solution. The two areas of concern for material selection for the solution are electrical compatibly pertaining to corrosion risk and particle size. In order to achieve the Cassie-Baxter state, a three-level micro-nanostructured hierarchical morphology must be produced to achieve the superhydrophobic surface. Most commonly, a carrier solution with low surface energy materials is used with microparticles and nanoparticles to create a coating to be applied to a substrate. The coating must provide a low energy surface along with the required hierarchical morphology. A review of the methods indicates that several materials appear to be favored in the construction of the coatings. Nanoparticle constituents such as silicon oxide, zinc oxide, copper

oxide, and magnesium oxide are often utilized in the creation of a low-energy surface by creating nanoscale asperities on microscale particles.

3.3.1 Layer-by-Layer Coating

A layer-by-layer method was used in a study to apply alternating $–CH_3$ ending and –OH ending alkanethiolate self-assembled monolayer (SAM) stripes on a gold substrate [1] [21]. The purpose here was to create a tunable wetting surface. The substrate was printed with octadecanthiol (C_{18}) using the polydimethylsiloxane (PDMS) stamp template to form the $–CH_3$ ending SAM stripes. The –OH ending stripes were created by soaking the specimen in 6-mercapto-1-hexanol (C_6OH) solution. The alternating stripes were confirmed by SEM and AFM. Then zirconia oxide thin films were applied to the surface by electrochemical deposition. The XPS studies showed that the thin films were applied to both Au-C_{18} and Au-C_{18}/C_6OH. The potential scan rate and number of cycles was varied during the deposition procedure. The thickness of the zirconia thin film was found to vary on the coating depending on the potential scan rate and number of cycles. The faster scan rate produced a zirconium thin film of less than 200 nm thickness, and the slower scan rate produced a film thickness of as much as 800–900 nm. This indicates that the coating thickness was controllable. The thicker film areas displayed a WCA in a very low and very high range of 40° and 145°, respectively. The thinner thin film areas had readings of 100–115°. The coating was shown to be tunable by creating a heterogeneous coating with a controllable thickness and WCA. A problem seen with these layer-by-layer coatings is that if the layers are not bonded adequately, separation can occur between the layers, which could allow corrosion to initiate [1] [21].

The Wenzel equation, equation (3.2), indicates that a hydrophilic material will become more hydrophilic and a hydrophobic material will become more hydrophobic when roughened because r (the roughness factor) is greater than 1. This study for investigating the tunability of a

coating showed that zirconia films, which have been shown to be inherently hydrophilic, can be made to have a hydrophobic surface. Analysis of this coating measured the WCA up to 145°, depending on the electrochemical deposition rate used. Much of the coating surface had a WCA > 100°, which indicates the hydrophilic zirconia film had become hydrophobic with the application of this coating [1] [21].

3.3.2 Layer-by-Layer Self-assembly

The layer-by-layer self-assembly method makes a thin layer coating that is assembled on the substrate one layer at a time, as the name implies, which is very similar to the first method. The process starts with a thorough cleaning and ionic neutralization of the substrate. The substrate is then given a negative charge while the first layer of ionic liquid (IL), which is 1-dodecyl-3-methylimidazoiumbromide ([C_{12} mim] Br) in this case, is attracted to the substrate due to a differential charge between the substrate and IL layer coating material [1] [22]. For the first layer of the coating material, the ionic liquid is made to have a positive charge, while the substrate is given a negative charge. Once the covalent bonding of the first layer of coating has achieved the desired thickness, the charge of the first layer is reversed so that the total coating now has a negative charge. The next layer, which is SiO_2 in this coating, is given the opposite charge (negative), and the second layer is then covalently bonded to the first layer of the coating. Alternating the substrate and coating layer charge in this manner is continued until the optimum number of layers is reached. The optimum number of layers is dependent on the particle size of the SiO_2.

By alternating the layers as described, a hybrid film can be built to a predetermined thickness. This method creates a superhydrophobic surface with a micro-nanostructured hierarchical morphology by building a hybrid film via self-assembly. This hybrid film can have a

WCA of 152.3°. Testing has shown that a wide range of contact angles can be achieved, depending on the number of bilayers and the size of the nanoparticles chosen. The complicated cleaning required and multiple steps to create the layers to get a superhydrophobic coating by this method may not appeal to industry due to possible economic issues or production scalability issues [1] [22].

3.3.3 Electrodeposition

Depositing the micro- and nanoparticles onto the substrate has been demonstrated via several methodologies that are common to metal working. Chemical-vapor-deposition and electro-deposition are examples of a few. A micro-nanostructure hierarchical morphology that is superhydrophobic has been created by electrochemical deposition. The difficulty that can be encountered is to create the correct anode-cathode separation for the contoured and complex shaped parts, which would need to be submersed in a tank of $CuSO_4+5H_2O$ solution or $ZnSO_4+7H_2O$ for industrial applications [1] [23].

The anodization process has been performed on test coupons of steel with an anode coupon size of 20x50x3 mm and cathode brass coupon of 20x50x5 mm using a copper and zinc-based electrolyte solution. The electrolytic process occurred at 23°C and continued for about 60 minutes. It took a full 24 hours for the coupon to be air dried. The low-energy micro-nanostructure morphology of the surface was produced by CuO and ZnO atoms that had been covalently bonded to the substrate. SEM images revealed micropapillae structures on the coating surface. Bu increasing the magnification on the SEM images, the papillae were noted to be made up of hemispheric structures with hemispheric structure roughened surfaces. The three-level micro-nanoparticle hierarchical morphology is similar to the lotus leaf structure and is what gives the surface superhydrophobic properties. The Cu-Zn coating had a contact angle of 153° with a

SA <10° [1] [23]. The self-cleaning property was shown to be present by letting a drop roll on the surface through fly ash. Stability was tested in a solution between 1 and 13 by adjusting the pH with H_2SO_4 and NaOH. There was only a slight change in the WCA after immersion, and the WCA stayed above 150^o, indicating that the coating is stable in acidic and alkaline conditions. The coating was also tested for thermal stability. After heat treating for an hour at different temperatures up to 200° C, the WCA remained above 150°. A peel test resulted in a contact angle of > 155° after seven repeats of the tape test.

3.3.4 Electrospinning

Electrospinning is an efficient simple scalable method to produce continuous nanofibers that can be spun into a mat and then applied to a substrate, or it can be directly spun onto a substrate. With this versatile process, it is possible to design hybrid fibers for specific applications by changing the solution materials and/or modifying the process parameters [1] [24] [25] [26] [27]. The electrospinning process produces hydrophobic fibers and with the addition of micro- and nanoparticles can produce superhydrophobic fibers. A WCA of 155° has been achieved. An example of electrospinning to create a superhydrophobic coating was demonstrated in 2016 in the development of a polyvinylidene fluoride (PVDF) coating [19]. PVDF, which is inherently hydrophobic, was made into a superhydrophobic coating with the addition of ZnO nanoparticles. The PVDF-ZnO coating can be applied by a spray method or the solution can be converted to the electrospinning method of coating. The advantage of electrospinning over spray was that the concentration of ZnO needed was only 1/6 of the concentration required for the spray coating. It is worth noting that the spray method coating had a WCA of 122°, while the electrospun PVDF-ZnO coating had a WCA of 155° with a CAH of 4.5^o. The WCA of the substrate was determined to be 88°. This reinforces the statement that using hydrophobic materials to chemically achieve

superhydrophobicity is insufficient. A micro-nanostructured morphology is also needed to achieve a superhydrophobic surface [1] [24].

3.3.5 Sol-Gel Coating

The sol-gel process is a wet chemical process [1]. It involves the preparation of the "sol" (solution) which is a colloidal solid/liquid dispersion, usually of silica, metal oxides, or carbon in a solvent. The sol is put through a drying process to achieve the gel state. The gel can then be applied to a substrate by dip coating, spinning, or other methods. The result is a porous coating. The coated substrate is then usually heat treated to obtain the desired mechanical properties and reduce the size of the pores. The final surface morphology is determined by the constituents and processing used.

The sol can be prepared by mixing metal alkoxides or metal chlorides such as methyltriethoxysilane (MTES) or trimethylchlorosilane (TMCS) with alcohol and ammonia to obtain polymerization [1] [28] [29] [30]. Methanol is most often the alcohol, but ethanol is sometimes used. An acidic sol can be obtained by using an acid and alcohol to prepare the solution [28]. Fluorination in the gel stage process to add chemical hydrophobicity to the coating [1] [28] [31] can decrease the surface energy of the coating enough to obtain superhydrophobicity [31]. Optimizing the concentration of metal alkoxides/chlorides [1] [32] can improve the surface morphology to obtain the micro-nanostructure morphology to achieve a superhydrophobic surface. Micro- and nanoparticles such as silica can be dispersed in the sol before the gel process [28] to improve the micro-nanostructure and achieve the hierarchical morphology, which has been shown to achieve a WCA of at least 163° with a hysteresis as low as 2°.

A transparent sol-gel organically modified silica (ORMOSIL) superhydrophobic coating was prepared from MTES in methanol and ammonium hydroxide, which was modified in a TMCS

solution [1] [29]. The glass substrate was heated to 100°C, and then the MTES/methanol/ammonium hydroxide mixture was deposited on it by the spray method and subsequently annealed at 150°C for 2 hours and heated at 500° for 1 hour. Finally, the silica film coated glass substrate was modified in a solution of TMCS and hexane for 5 hours at room temperature and then annealed at 100°C for 1 hour. Methyl-groups were confirmed by FTIR, and 100–300-nm silica particles were identified on the surface by SEM. The root-mean-square (RMS) roughness value by AFM was found to be 137 nm. The WCA and SA of the unmodified silica coating were found to be 94° and 39°, respectively. After modification with the TMCS, the WCA increased to 167°, and the SA decreased to 3°. Thermal stability was tested and the coating was stable up to 200°C and decomposed up to 600°C. Hydrophobicity was retained up to 500°C on the unmodified coating but retained superhydrophobicity up to 550°C for the TMCS modified coating.

3.3.6 Hydrothermal Synthesis

Clean zinc plates were immersed in dimethylformamide (DMF) at 80°C for 24 hours and then dried at 120°C for 2 hours [1] [30]. The SiO_2 solution to be used for modification of the treated zinc specimens was prepared by a sol-gel process. Tetraethoxysilane (TEOS) as a precursor and ethanol as a solvent were mechanically mixed with distilled water for 12 hours at room temperature. Then solutions with varying concentrations of hexamethyldisiloxane (HMDS), and one without HDMS, were prepared for modification and then aged for 2 hours at 80°C. Next the pretreated zinc substrates were immersed in the sol-gel SiO_2 for modification for 2 hours at room temperature. SEM images of the structures on the surface after treatment revealed a flat layer of nanorods with diameters in the range of 50–150 nm and sub-micro tubes with diameters in the range of 300–400 nm both of ZnO. The rods and sub-micro tubes form a micro-nanostructure morphology. The contact angles of the different concentrations of HDMS showed that the WCA

increases as the concentration of HDMS increases, but when the HDMS/TEOS ratio reached a ratio of 3 (designated S3), the WCA decreased steadily with subsequent specimens. The highest WCA was 152° for a molar ratio of 2 (designated S2). The bare Zn and TEOS only treated substrates (designated S0) had water contact angles of 81° and 26°, respectively. Electrochemical corrosion testing producing polarization curves showed that the current density (i_{Corr}) was only 0.08 μA/cm^2 vs 18.48 μA/cm^2 for S2 and S0, respectively, and Bode plots showed a much higher impedance modulus $|Z|$ value for S2, indicating a very good corrosion resistance for this coating. Abrasion testing with sandpaper showed that S2 had superior abrasion resistance and maintained superhydrophobicity after four cycles of testing.

3.3.7 One-Pot Coating

One-pot coating is the name given to the method where solutions are mixed in a single container [1]. The method of application has no connection to the name. A solution is chosen to which micro-nanoparticles are then added. The viscosity of the solution determines if the coating is applied by dipping, painting, spraying, or layer-by-layer. As with most superhydrophobic coatings, the one-pot coating attaches to the substrate by covalent bonding. One successful one-pot coating was developed using room temperature vulcanizing (RTV) silicone rubber containing alumina hydrate mixed with stearic acid. The coating was allied using the spray method. When dried, the coating developed a micro-nanostructure morphology that produced a WCA of 160° and a CAH of 4° [33]. A second one-pot coating was developed using carbon nanotubes and a fluoroplastic (Teflon® PFA), which was spray coated. This coating was shown to have a WCA of 153° and a CAH < 5° [34].

A polymer film can provide the needed corrosion mitigation. The micro- and nanoscale hierarchical structures may be formed by mixing a low-energy epoxy base coat with micro- and

nanoparticles. By creating a uniform mixture, a polymer film may be created and applied to any surface to which the epoxy will adhere [1] [35]. The method of application is not restricted and is suitable for large areas of application if spraying is utilized. Dipping and brush application may also be considered suitable application methods. The key is to have the micro- and nanoparticles uniformly mixed in every droplet of the coating.

One method to create a polymer film coating is to add all the ingredients into a single container and mix until a uniform suspension of the micro and nanoparticles has been achieved in the solution. After choosing a method of application, depending on the viscosity of the polymer solution, the film or coating can be applied to the substrate. As the epoxy in the coating hardens, there is a slight shrinkage that allows the micro and nanoparticles to be exposed. The particles in the coating form the micro-nanostructure hierarchical morphology needed to create the superhydrophobic surface. The coating surfaces can be damaged over time due to exposure to UV light, chemicals, impact, or other mechanical interaction. The hierarchical morphology can become flattened, thereby loosing hydrophobicity. Research has shown that the polymer coating surface morphology can be revitalized by mechanically roughening the surface with sandpaper [1] [35]. This revitalization has been demonstrated to be effective for a finite number of times before the coating must be reapplied.

3.3.8 Hybrid Coating

Hybrid coatings can be obtained by combining different methods. An example is a hybrid coating to improve scratch resistance of superhydrophobic coatings. The sol-gel and spinning process were incorporated into the layer-by-layer method. The first layers were spun resin layers followed by photochemical curing. Next the sol-gel mixture inorganic multilayers were applied by airbrushing. Finally, a perfluoropolyether (PFPE) was applied to the surface by a spinning process.

The coating included metal alkoxides of TiO_2, ZrO_2, and SiO_2 incorporated into the layer-by-layer method [1] [32]. Multilayered samples ranging from one layer to seven layers were prepared and tested. Testing for scratch resistance includes adherence and scratch resistance testing as well as abrasion and erosion tests. The coatings had thicknesses from 7.6 to 67 µm. Some agglomeration occurred, possibly due to the differing rates of reaction of the precursors. Characterization of the roughened surface revealed that the five-layer and seven-layer coatings had the needed roughness and micro-nanostructured surface to be superhydrophobic. The WCA for the five-layer coating was 155° with a CAH of 1°, and the seven-layer coating had a CA of 154° with a CAH of 5°. The five-layer coating has a stable superior superhydrophobicity.

3.3.9 Other Coatings

Other frequently used methods to produce superhydrophobic coatings involve directly altering the surface of the substrate to obtain a superhydrophobic surface instead of relying on a superhydrophobic coating to create the superhydrophobic surface. One of these methods is chemical etching. Numerous studies have shown that physical roughening of the material surface is not sufficient to achieve superhydrophobic surface. Chemical heterogeneity needs to be modified to create a low surface energy material after etching. A study of the effect of preparation method and treatment in organic acids on the aluminum was conducted [1] [36]. Commercial pure aluminum substrates were prepared using various combinations of surface preparation with fine, extra fine, superfine, and ultrafine polishing. Roughness values indicated that sequentially preparing the surface with SiC abrasive paper (63 µm), extra fine (35.8 µm), and superfine (15.3µm) gave the best results. The substrates were then immersed in a solution of ethanol, hydrochloric acid, and lauric acid for etching over 10 min at 50^{o}C. Finally, the specimens were heated at 80°C for 30 minutes after being rinsed in ethanol and deionized water. Different

concentrations of lauric acid were used for immersion of the substrates, and then more specimens were produced using myristic acid. Surface roughness was evaluated using AFM. The AFM-RMS values for the substrates treated with the 20 g/L myristic acid and 30 g/L lauric acid were the highest, and these substrates had a WCA of 149° and 153°, respectively. The 30 g/L Lauric acid substrate was calculated to have a solid/liquid contact area of only 6%.

In one study, anodic titania nanotubes were formed on titanium foils in glycol and water with ammonium fluoride (NH_4F) at 20 V for 5 hours [1] [37]. After drying, the substrates were immersed in a solution of 1H,1H,2H,2H-Perfluorooctyltriethoxysilane (PTES), ethanol, and water for 1 hour to achieve hydrolysis of a SAM's layer on the etched substrate surface and then heat treated for 1 hour at 140^{o}C. The surface had a protrusion-like micro-nanostructured morphology with a net-like substructure, which was superhydrophilic with a WCA < 10^{o} after pretreatment in ammonium fluoride. After formation of the SAM, the WCA of the surface was found to be 160^{o} with a SA < 10°. Specimens without a potentiostatic anodization pretreatment were coated with the PTES coating, and the WCA was only 120^{o}. Corrosion testing in simulated seawater was conducted and showed the coating had increased corrosion resistance even after 90 days of immersion.

3.4 Recent Corrosion Mitigation Research

In order to stop or slow down corrosion, one or more components of the corrosion process must be minimized [1]. That is, the anode and cathode should exhibit minimized potential differences and/or the electrolyte must be eliminated or prevented from completing the circuit between the anode and cathode. The low surface energy of the superhydrophobic coating and low solid surface interface with the water droplet provide the coating with repellant and self-cleaning properties. These properties provide protection against corrosion by preventing the oxygen and the

electrolyte needed for corrosion initiation from reaching the substrate surface. Superhydrophobic coatings developed for corrosion mitigation must be durable since they will be exposed to environmental conditions, which can degrade the coating surface resulting in loss of hydrophobicity and surface cracking, thus undermining the usefulness of the coating as a barrier to corrosion initiation. Environmental conditions include exposure to UV light, heat, acid rain, and other weather conditions as well as coastal salt exposure. UV light exposure over long periods of time is the most damaging to polymeric materials, which, because of their inherent hydrophobicity, are commonly used in superhydrophobic coatings [1] [38]. Additives in the coating can mitigate the UV degradation. Added multi-walled carbon nanotubes (MWCNTs) have been shown to decrease UV degradation in polymeric coatings [38]. Graphene is hydrophobic, absorbs most of the incident light, and has been shown to be a possible addition for protection against UV degradation [39]. Other possible additives include ZnO and TiO_2 [40], although TiO_2 can produce free radicals, which can have an adverse effect on the coating over time [39] [41].

Self-healing superhydrophobic coatings have been a focus of research using shape-memory materials. One study developed a superhydrophobic coating with the ability to restore hydrophobicity and repair the surface damage by adding an epoxy shape memory polymer (SMP) and benzotriazole corrosion inhibitor [1] [42]. A PDMS template of a lotus leaf superhydrophobic surface with a lotus-like microstructure was made and used to imprint the lotus leaf surface morphology to the coating surface. When the coating was cut with a sharp blade and crushed with steel bars both by pressing into the surface and rolling the surface, the coating surface hydrophobicity was restored by heating to 60°C to trigger the shape memory effect. Outdoor exposure to direct sunlight was also able to affect self-healing efficiency. The cut was usually too small for water penetration after restoration of the surface morphology. The corrosion inhibitor

was effective in increasing corrosion inhibition at the site of the cut when over time water was eventually able to penetrate the cut. The WCA of the coating was > 153° and the SA was < 6°.

In a recent research study, a PVDF-ZnO nanocomposite superhydrophobic coating was applied by an electrospinning process onto an aluminum substrate [1] [19]. The developed coating was compared to a pure PVDF coating and the bare Al substrate. SEM images revealed the pure PVDF coating had a porous surface. Adding the ZnO nanoparticles in the PVDF-ZnO coating resulted in a decreased size of pores and an increase in their number on the surface. AFM analysis showed that the PVDF-ZnO coating increased the surface roughness by a factor of 2 higher than the pure PVDF coating. Corrosion data revealed that the current density was significantly lowered for both coatings compared to the bare substrate, but it was even lower for the PVDF-ZnO coating. The polarization resistance was also much higher for the PVDF-ZnO coating compared to the pure PVDF-ZnO coating. The protection efficiency of corrosion resistance, equation (3.6), was calculated with the corrosion current density data obtained during corrosion testing. It was found that the pure PVDF coating had a protection efficiency of 84%, and the PVDF-ZnO coating had an efficiency of 99%. The PVDF-ZnO coating was shown to have much higher corrosion mitigation properties. More on this coating can be found in section 3.3.4 on electrospinning.

In another study, a substrate of magnesium alloy AZ31 was immersed in a cerium nitrate hexahydrate solution for 20 minutes to apply a nanostructured cerium oxide film. The coated substrate was then immersed in a fluoroalkylsilane (FAS) solution with an accelerant for 30 minutes to complete the application of a superhydrophobic coating for corrosion control [1] [43]. The coating was analyzed for morphology and elemental content. X-ray diffraction (XRD) analysis was used to investigate the crystalline structure of the material. A cerium oxide film was verified on the magnesium surface with a thickness of 2 μm covered with FAS molecules. FE-SEM images

showed the cerium oxide film formed peaked ridges on the surface of the substrate aligned at sharp angles to the surface. The ridges were approximately 200 nm to 1 μm in length along the substrate surface, and the ridge thickness was 20–50 nm. Static contact angles were taken, and the coating had a WCA of 153° with a 7° CAH. The coated magnesium was immersed in 5.0 wt% NaCl for 24 hours, and the WCAs were obtained at 30, 180, 360, and 1440 minutes. The contact angles were stable up to 360 minutes, and then at 1440 minutes, the static WCA dropped to an average of 50° with a > 100° CAH. A cross-cut tape test according to D3359-17 was performed and indicated good adhesion of the coating to the substrate. The WCA was checked before and after the tape test to evaluate stability. The superhydrophobic coating had good adhesion and the contact was unchanged after tape removal.

Corrosion testing revealed a significant increase in the corrosion potential and decrease in current density for the cerium oxide coated magnesium compared to the bare magnesium which indicated good corrosion resistance improvement, but after immersion in the 5.0 wt% NaCl for 24 hours the corrosion potential steadily decreased, while the current density remained stable [1] [43]. Although the corrosion potential was decreasing, it remained above the potential for the bare magnesium throughout the corrosion testing. At the end of 24 hours immersion, the superhydrophobicity of the coating was lost during corrosion testing when the WCA decreased 50°. The coating was effective in providing corrosion resistance to the surface, although this property was lost at the end of corrosion testing.

3.5 Conclusions

Superhydrophobic coatings have been created using a number of different methods for various industrial applications, such as water repellency, anti-icing, and self-cleaning [1]. Recent studies have shown that superhydrophobic coatings are good candidates for use in corrosion

mitigation. These micro-nanostructured coatings with low surface energy can be designed for use in many corrosion applications. They are versatile and can be robust and durable by choosing the appropriate materials and methods, some of which include layer-by-layer, layer-by-layer self-assembly, electrodeposition, electrospinning, hydrothermal synthesis, sol-gel, and others discussed here, but there are more. Hybrid coatings can be developed by combining methods and modifying the processes for a better superhydrophobic surface. In this work, superhydrophobic coatings are being applied to corrosion control of aluminum alloys. A one-pot method was chosen in an attempt to achieve a coating that is easy to produce and cost effective. The materials chosen will not produce by-products that have an adverse effect on the environment and are not harmful to human life when normal safety procedures are followed.

3.6 References for Chapter 3

[1] S. F. Jurak, E. Jurak, M. M. Rahman, and R. Asmatulu, "Nanoscale Superhydrophobic Coating for Corrosion Mitigations," in *Nanocomposites*, M. Ram, Ed., Elsevier (in press).

[2] A. Otten and S. Herminghaus, "How Plants Keep Dry: A Physicist's Point of View," *Langmuir*, vol. 20, no. 6, p. 2405-2408, March 16, 2004.

[3] C. Neinhuis and W. Barthlott, "Characterization and Distribution of Water-Repellent, Self-Cleaning Plant Surfaces," *Annals of Botany*, vol. 79, no. 6, pp. 667-677, June 1, 1997.

[4] A. M. Mohamed, A. M. Abdullah, and N. A. Younan, "Corrosion Behaviour of Superhydrophobic Surfaces: A Review," *Arabian Journal of Chemistry*, vol. 8, no. 6, pp. 749-765, November 2015.

[5] J. T. Woodward, H. Gwin, and D. K. Schwartz, "Contact Angles on Surfaces with Mesoscopic Chemical Heterogeneity," *Langmuir*, vol. 16, no. 6, pp. 2957-2961, 2000.

[6] R. N. Wenzel, "Resistance of Solid Surfaces to Wetting by Water," *Industrial and Engineering Chemistry*, vol. 28, no. 8, p. 988-994, 1936.

[7] R. N. Wenzel, "Surface Roughness and Contact Angle," *The Journal of Physical Chemistry*, vol. 53, no. 9, p. 1466-1467, 1949.

[8] A. B. D. Cassie and S. Baxter, "Wettability of Porous Surfaces," *Transactions of the Faraday Society*, vol. 40, no. 0, pp. 546-551, June 1944.

[9] A. Lafuma and D. Quéré, "Superhydrophobic States," *Nature Materials*, vol. 2, no. 7, pp. 457-460, 2003.

[10] T. Sun, L. Feng, X. Gao, and L. Jiang, "Bioinspired Surfaces with Special Wettability," *Accounts of Chemical Research*, vol. 38, no. 8, pp. 644-652, 2005.

[11] T. T. Isimjan, T. Wang, and S. Rohani, "A Novel Method to Prepare Superhydrophobic, UV Resistance and Anti-Corrosion Steel Surface," *Chemical Engineering Journal*, vol. 210, pp. 182-187, November 2012.

[12] A. J. Milne and A. Amirfazli, "The Cassie Equation: How It Is Meant to be Used," *Advances in Colloid and Interface Science*, vol. 170, no. 1-2, p. 48-55, 2012.

[13] K. M. Hay, M. I. Dragilab, and J. Liburdy, "Theoretical Model for the Wetting of a Rough Surface," *Journal of Colloid and Interface Science*, vol. 325, no. 2, pp. 472-477, 2008.

[14] W. Choia, A. Tuteja, J. M. Mabry, R. E. Cohen, and G. H. McKinley, "A Modified Cassie-Baxter Relationship to Explain Contact Angle Hysteresis and Anisotropy on Non-Wetting Textured Surfaces," *Journal of Colloid and Interface Science*, vol. 339, no. 1, pp. 208-216, 2006.

[15] P. Varshney, S. S. Mohapatra, and A. Kumar, "Superhydrophobic Coatings for Aluminium Surfaces Synthesized by Chemical Etching Process," *International Journal of Smart and Nano Materials*, vol. 7, no. 4, pp. 248-264, 2016.

[16] S. Zheng, C. Li, Q. Fub, W. Hua, T. Xianga, Q. Wanga, M. Dua, X. Liu, and Z. Chen, "Development of Stable Superhydrophobic Coatings on Aluminum Surface for Corrosion-resistant, Self-Cleaning, and Anti-Icing Applications," *Materials and Design*, vol. 93, pp. 261-270, March 2016.

[17] S. Pana, N. Wang, D. Xionga, Y. Dengb and Y. Shi, "Fabrication of Superhydrophobic Coating via Spraying Method and its Applications in Anti-Icing and Anti-Corrosion," *Applied Surface Science*, vol. 389, pp. 547-553, December 2016.

[18] L. B. Boinovich, S. V. Gnedenkov, D. A. Alpysba, V. S. Egorkin, A. M. Emelyanenko, S. L. Sinebryukhov, and A. K. Zaretskaya, "Corrosion Resistance of Composite Coatings on Low-Carbon Steel Containing Hydrophobic and Superhydrophobic Layers in Combination with Oxide Sublayers," vol. 55, pp. 238-245, February 2012.

[19] A. B. Radwan, A. M. Mohamed, A. M. Abdullah, and M. A. Al-Maadeed, "Corrosion Protection of Electrospun PVDF-ZnO Superhydrophobic Coating," *Surface & Coatings Technology*, vol. 289, pp. 136-143, March 15, 2016.

[20] R. Blossey, "Self-cleaning Surfaces—Virtual Realities," *Nature Materials*, vol. 2, no. 5, pp. 301-306, May 2006.

[21] Y. Hao, D. M. Soolaman, and H.-Z. Yu, "Controlled Wetting on Electrodeposited Oxide Thin Films: From Hydrophilic to Superhydrophobic," *The Journal of Physical Chemistry C*, vol. 117, pp. 7736-7743, 2013.

[22] C. Zhang, S. Zhang, P. Gao, H. Ma, and Q. Wei, "Superhydrophobic Hybrid Films Prepared from Silica Nanoparticles and Ionic Liquids via Layer-by-Layer Self-Assembly," *Thin Solid Films*, vol. 570, pp. 27-32, 2014.

[23] H. Li and S. Yu, "Three-level Hierarchical Superhydrophobic Cu-Zn Coating on a Steel Substrate without Chemical Modification for Self-cleaning Property," *New Journal of Chemistry*, vol. 41, pp. 5436-5444, 2017.

[24] A. Meikandan and K. Malarmonan, "Fabrication of a Superhydrophobic Nanofibers by Electrospinning," *Digest Journal of Nanomaterials and Biostructures*, vol. 12, no. 1, pp. 11-17, 2017.

[25] N. Nuraje, W. Khan, Y. Lei, M. Cheylan, and R. Asmatulu, "Superhydrophobic Electrospun Nanofibers," *Journal of Materials Chemistry A*, vol. 1, no. 6, pp. 1929-1946, 2013.

[26] R. Asmatulu, M. Ceylan, and N. Nuraje, "Study of Superhydrophobic Electrospun Nanocomposite Fibers for Energy Systems," *Langmuir*, vol. 27, no. 2, pp. 504-507, 2011.

[27] M. Salahuddin, M. N. Uddin, G. Hwang, and R. Asmatulu, "Superhydrophobic PAN Nanofibers for Gas Diffusion Layers of Proton Exchange Membrane Fuel Cells for Cathodic Water Management," *International Journal of Hydrogen Energy* (in press), August 26, 2017.

[28] Q. F. Xu, J. N. Wang, and K. D. Sanderson, "A General Approach for Superhydrophobic Coating with Strong Adhesion Strength," *Journal of Materials Chemistry*, vol. 20, no. 28, p. 5961-5966, 2010.

[29] S. A. Mahadik, D. B. Mahadik, M. S. Kavale, V. G. Parale, P. B. Wagh, H. C. Barshilia, S. C. Gupta, N. D. Hegde, and A. V. Rao, "Thermally Stable and Transparent Superhydrophobic Sol-Gel Coatings by Spray Method," *Journal of Sol-Gel Science and Technology*, vol. 63, no. 3, pp. 580-586. 2012.

[30] A. V. Raoa, S. S. Latthea , S. A. Mahadika, and C. Kappenstein, "Mechanically Stable and Corrosion Resistant Superhydrophobic Sol-Gel Coatings," *Applied Surface Science*, vol. 257, no. 13, pp. 5772-5776, 2011.

[31] A. Roig, E. Molins, E. Rodríguez, S. Martínez, M. Moreno-Manãs, and A. Vallribera, "Superhydrophobic Silica Aerogels by Fluorination at the Gel Stage," Chemical Communications, 2004, pp. 2316-2317, 2004.

[32] R. Taurino, E. Fabbri, D. Pospiech, A. Synytska, and M. Messori, "Preparation of Scratch Resistant Superhydrophobic Hybrid Coatings by Sol-Gel Process," *Progress in Organic Coatings*, vol. 77, no. 11, p. 1635-1641, 2014.

[33] G. Momen and M. Farzaneh, "Simple Process to Fabricate a Superhydrophobic Coating," *Micro & Nano Letters*, vol. 6, no. 6, pp. 405-407, 2011.

[34] K. Wang, N.-X. Hu, G. Xu, and Y. Qi, "Stable Superhydrophbic Composite Coatings Made Aqueous Dispersion of Carbon Nanotubes and a Fluoropolymer," *Carbon*, vol. 49, pp. 1769-1774, 2011.

[35] Y. Si, F. Yangm and Z. Guo, Zhiguang, "Bio-Inspired One-Pot Route to Prepare Robust and Repairable Micro-Nanoscale Superhydrophobic Coatings," *Journal of Colloid and Interface Science*, vol. 498, pp. 182-193, 2017.

[36] A. M. Escobar and N. Llorca-Isern, "Superhydrophobic Coating Deposited Directly on Aluminum," *Applied Surface Science*, vol. 305, p. 774-782, June 2014.

[37] F. Zhang, S. Chen, L. Dong, Y. Lei, T. Liu, and Y. Yin, "Preparation of Superhydrophobic Films on Titanium as Effective Corrosion Barriers," *Applied Surface Science*, vol. 257, no. 7, p. 2587-2591, 2011.

[38] R. Asmatulu, G. A. Mahmud, C. Hille, and H. E. Misak, "Effects of UV Degradation on Surface Hydrophobicity, Crack, and Thickness of MWCNT-based Nanocomposite Coatings," *Progress in Organic Coatings*, vol. 72, no. 3, p. 553-561, 2011.

[39] N. Nuraje, S. I. Khan, H. Misak, and R. Asmatulu, "The Addition of Graphene to Polymer Coatings for Improved Weathering," *ISRN Polymer Science*, vol. 2013, pp. 1-8, 2013.

[40] R. Asmatulu, D. Diouf, M. Moniruddin, and N. Nuraje, "Enhanced Anti-Weathering of Nanocomposite Coatings with Silanized Graphene Nanomaterials," *International Journal of Engineering Research and Application*, vol. 6, no. 6, pp. 2248-9622, 2016.

[41] R. Asmatulu, "Nanocoatings for Corrosion Protection of Aerospace Alloys," in *Corrosion Protection and Control Using Nanomaterials*, pp. 357-374, V. S. Saji and R. M. Cook, Eds., Cambridge: Woodhead Publishing Limited, 2012.

[42] H. Qian, D. Xu, C. Du, D. Zhang, X. Li, L. Haung, L. Deng, Y. Tu, and J. M. Mol, "Dual-Action Smart Coatings eith a Self-Healing Superhydrophobic Surface and Anti-Corrosion Properties," *Journal of Materials Chemistry A*, no. 5, pp. 2555-2564, 2017.

[43] T. Ishizaki , Y. Masuda, and M. Sakamoto, "Corrosion Resistance and Durability of Superhydrophobic Surface Formed on Magnesium Alloy Coated with Nanostructured Cerium Oxide Film and Fluoroalkylsilane Molecules in Corrosive NaCl Aqueous Solution," *Langmuir*, vol. 27, no. 8, pp. 4780-4788, March 2011.

CHAPTER 4

DEVELOPMENT OF NANOSCALE SUPERHYDROPHOBIC COATING FOR CORROSION MITIGATION OF ALUMINUM ALLOYS

4.0 Abstract

The purpose of this study was to develop a superhydrophobic coating for corrosion mitigation in aluminum alloys. AA2024-T3 and AA7075-T6 specimens were coated and tested. Initially the coating development achieved a water contact angle (WCA) of 154^{o}. The design of experiments (DOE) was then used to refine the constituent parameters, which allowed for the development of a coating with less materials and a higher WCA. The final superhydrophobic coating was found to have an average WCA of 158^{o}, SA of 4.08^{o}, and hysteresis of 7.6^{o}. The coating was tested in acetone and sulfuric acid to determine its durability. The acetone had no effect on the WCA, but there was some decrease in WCA with submersion in sulfuric acid, but it was still highly hydrophobic. The coating was also heat treated up to 230^{o}C with no effect on its superhydrophobicity. Then it was then submerged in sodium bicarbonate, which had a significant effect on its hydrophobicity. The WCA was decreased to 109^{o} from 154^{o}. An adhesion crosshatch tape test showed good adhesion of the superhydrophobic coating to the substrate.

4.1 Introduction

Superhydrophobic coatings have numerous applications, from windshields to textiles, due to their repellent and self-cleaning properties. They also have applications in corrosion mitigation. Since the corrosion process requires oxygen for oxidation and an electrolyte, which can be provided by water/moisture, if the surface is protected by a superhydrophobic coating to prevent the moisture and oxygen from reaching it, corrosion can be mitigated. Researchers use the design of the lotus leaf as the basis of their research. There are numerous examples of superhydrophobic

surfaces in nature [1] [2], but the lotus leaf is the most ideal example [3]. Epicuticular wax on the lotus leaf surface provides a low surface energy, and micropapillae with nanostructure protuberances provide a macro-nanostructured hierarchical morphology of the surface [4].

The superhydrophobic surface can be evaluated relative to the contact angle between the droplet and the surface. Wenzel [5] [6] used the Young's equation for surface energy to show that the WCA is an indication of the amount of surface superhydrophobicity by revealing that a roughened surface will increase the WCA due to the increase in effective surface area. Cassie and Baxter showed that if the surface is roughened adequately, then the droplet will not have contact with the surface at the trough between asperities [7]. This creates a composite surface area where the water droplet contact area is with both the surface and the air trapped between asperities, which decreases the effective surface area and surface energy holding the droplet. Thus, the droplet will roll easier. A superhydrophobic surface has a WCA greater than 150^{o}, but if the sliding angle is less than 10^{o} and there is low contact angle hysteresis (CAH), typically 5–10^{o} [8] or less, then it will manifest what is referred to as the "lotus effect" [9] [10], where a droplet bounces on the surface and easily rolls off, taking dirt and debris with it. That is what provides the self-cleaning property. A macro-nanostructured hierarchical surface morphology with a low surface energy will provide a superhydrophobic surface with an SA less than 10^{o} and low hysteresis. The three water droplet states are depicted in Figure 4.1

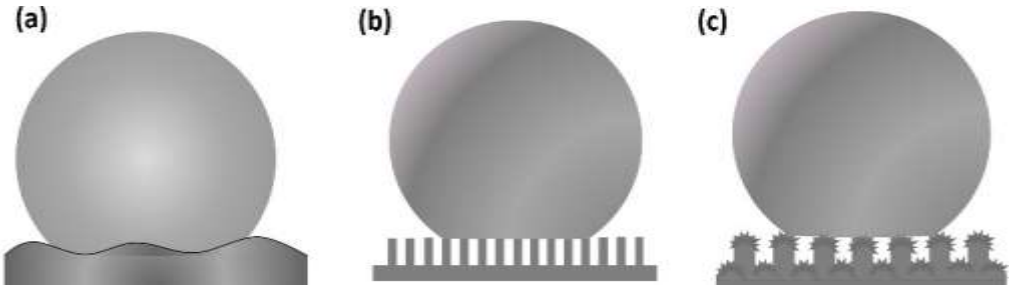

Figure 4.1. Water droplet in various states: (a) Wenzel state, (b) Cassie-Baxter state and (c) micro-nanostructured hierarchical morphology [11].

Since a superhydrophobic coating shows promise in corrosion mitigation, a coating that could provide corrosion protection to metallic surfaces could be useful. Corrosion costs the U.S. economy more than a trillion dollars annually [12]. Therefore, extensive research is being done to develop methods to address this problem. The purpose of this study was to design a superhydrophobic coating for the corrosion mitigation of aluminum alloys. Previous related work used RTV silicone rubber HVIC 1547, which contains 40–70 wt% alumina hydrate [13] [14] as a basis for developing a superhydrophobic coating for anti-icing applications. The RTV provided a low surface energy component, with alumina hydrate in the coating adding to the morphology. Momen and Farzaneh [13] mixed stearic acid of differing concentrations with the RTV coating and found that "blade-like" structures formed on the surface of the coating changing the surface morphology which achieved a static WCA of 163^{o} and < 5^{o} CAH. Arianpour et al. [14] mixed the RTV SR with n-hexane and added nanoparticles of carbon black, titanium oxide, or cerium oxide to the coating to determine how the particles would affect the properties of the coating. A coating with a WCA of 150^{o} and CAH of less than 10^{o} was achieved with all three nanoparticles. A simple low-cost coating that didn't require expensive equipment or hazardous chemicals for production would be more sustainable as well as environmentally friendly and would be attractive to industry. A one-pot method was chosen for assembly of the coating due to the ease of production. It was

decided to use a silicone caulking for the low surface energy component of the coating and add aluminum powder to the coating for the macrostructural constituent. The constituents would be mixed with mineral spirits to create the coating. Zinc oxide nanoparticles were also added for the nanostructural constituent because it could provide protection for the coating from UV light. Also, Zn is close to Al on the electrochemical potential chart and would be less likely to react with the aluminum in the coating. Zn and Al particles have been added to polymer coatings for use in marine corrosion applications [15] [16].

4.2 Experimental Procedure

Zinc oxide was obtained from U.S. Elements, and an aluminum powder of mesh 200 was obtained from Acros Organics. Jasco Paint Thinner (100% Mineral Spirits) and GE Silicone II 10 clear silicone caulking (10.1 oz.) were obtained from Lowe's Home Improvement. Aluminum AA2024-T3 and AA7075-T6 sheets were obtained from TW Metals Inc., Park City, Kansas. These metals were chosen because they are aviation materials. The material composition is shown in Table 4.1 for AA2024 and AA7075.

TABLE 4.1

MAXIMUM MATERIAL COMPOSITION OF AA2024-T3 AND AA7075-T6 BY WT% [17]

Material	*Tested Tensile Strength (ksi)*	*Composition (wt %) max.*										
		Si	*Fe*	*Cu*	*Mn*	*Mg*	*Cr*	*Zn*	*Ti*	*Other*		*Al*
										Ea.	*Tot.*	
2024-T3	LT:67.9-70.2	0.5	0.5	3.8-4.9	0.3-0.9	1.2-1.8	0.1	0.25	0.15	0.05	0.15	Bal
7075-T6	---	0.4	0.5	1.2-2.0	0.3	2.1-2.9	0.18-0.28	5.1-6.1	0.3	0.05	0.15	Bal

Differing amounts of Al, ZnO, and Si caulking were added to mineral spirits and mechanically mixed using a magnetic stirrer for 2 hours. Specimens 1.5 inch x 1.75 inch in size were cut from the aluminum sheets. Specimens of AA7075 and AA2024 were cleaned first with

acetone and then with ethanol by sonicating them for 10 minutes in each. Then the specimens were rinsed in reverse osmosis (RO) water and submerged in 0.7 M sulfuric acid for 30–40 minutes under 20 V DC current to etch the surface and improve adherence of the coating to the substrate. The specimens were weighed before and after etching. The setup for etching is shown in Figure 4.2. The four-specimen etching setup was developed to support the need for numerous specimens to run an experimental design.

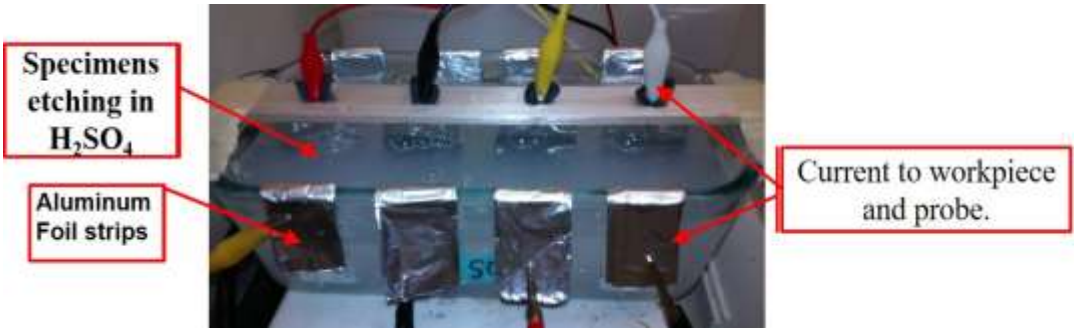

Figure 4.2. Four-specimen etching setup used to prepare specimens.

The WCA of each specimen was obtained before and after etching. The prepared coatings were applied to the Al specimens by a dip method. At first the coating was applied by brushing it onto the Al substrates, but the coverage was not good using that method, so the specimens were then dipped in the coating. The dip method resulted in a well-coated specimen. Brushed- specimen and dipped-specimen surfaces are shown in Figure 4.3. A spray method could also be effective.

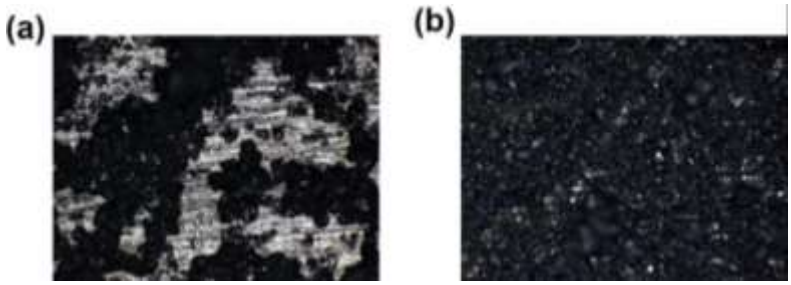

Figure 4.3. Aluminum specimens coated with the superhydrophobic coating taken at 10X magnification: (a) brush method and (b) dipping method.

Next the specimens were placed in a desiccator under negative pressure to remove air bubbles from the applied coating. After drying, the specimens were heat treated for 30 minutes at

150°C to remove residual mineral spirits from the coating. Then they were weighed and the coating WCA obtained. Initially only Si and Al powder were used in the coating for development. The addition of 26 wt% of Al particles in 61 wt% mineral spirits with 13 wt% Si caulking achieved a WCA of 142°. This constituent wt% composition was determined by trial and error. Next, 6 wt% ZnO nanoparticles were added to the mixture. This addition achieved a contact angle of 154°. A range for the Si, Al, and ZnO was designed around this constituent composition and entered into Statgraphics® software to obtain a DOE for optimizing the superhydrophobic coating composition. The final experimental design is shown in Table 4.2

TABLE 4.2

EXPERIMENTAL DESIGN FOR CENTRAL COMPOSITE STAR^3 DOE WITH 2-STAR POINTS AND TWO REPLICATES PERFORMED FOR EACH SET OF COATING PARAMETERS

Experimental Design			Equivalent Parameters		
*Si	Al	Zn	wt% *Si	wt% Al	wt% Zn
0	0	-1.682	13.96	19.54	2.28
0	0	0	13.33	18.67	6.67
0	1.6818	0	11.75	28.31	5.88
-1	1	-1	6.76	27.03	4.05
-1.682	0	0	2.39	21.02	7.51
0	-1.682	0	16.15	1.47	8.08
-1	-1	1	7.58	12.12	10.61
0	0	1.6818	12.76	17.87	10.67
1	1	-1	17.86	23.81	3.57
-1	-1	-1	8.06	12.90	4.84
1	-1	-1	20.83	11.11	4.17
-1	1	1	6.41	25.64	8.97
0	0	0	13.33	18.67	6.67
1	-1	1	19.74	10.53	9.21
1.6818	0	0	22.07	16.78	5.99
1	1	1	17.05	22.73	7.95

*Si contribution by Si caulking component

The coatings were characterized by obtaining the WCA for each coating using the sessile drop method. Each droplet was 20 µL in conformance with ASTM D7334-08(2013). Initially, three sites were tested as directed in the standard, but this resulted in too much variation in the final average contact angles, so it was decided to test five sites, one in the middle and one on each corner. The resulting average contact angles had much less variation between the three specimens for each coating. A droplet is shown on the surface of the coating in Figure 4.4(a). WCA testing was accomplished using a contact angle goniometer/optical tensiometer from Dyne Technology shown in Figure 4.4(b). This was used with a CAM100 program. The contact angle hysteresis of the final coating was determined using the goniometer for taking measurements as water was added to a droplet until it expanded for the advancing angle and then removing water from the droplet until it contracted for the receding angle, as described in ASTM C813-90(2014). The sliding angle was also determined by putting the droplet on the surface and gradually inclining the surface. The incline angle readings were determined using a digital level.

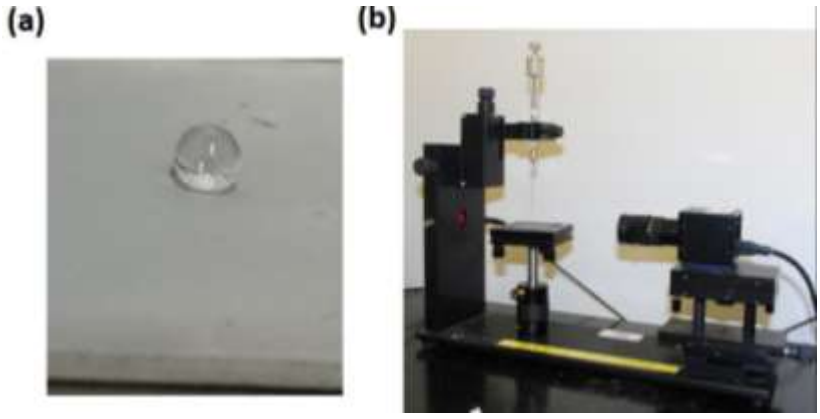

Figure 4.4. Surface characterization: (a) droplet on superhydrophobic coating surfaces, and (b) optical goniometer/tensiometer used to obtain WCA.

The durability of the final coating was evaluated by immersing the coated specimen in an acid, a base, a solvent and subjecting it to heat treatments. The adhesion strength was evaluated by performing a cross-hatch tape test according to ASTM D3359-17.

4.3 Results and Discussion

4.3.1 Testing of Coating

Static water contact angles were obtained for each specimen. There were 16 runs with two replicates performed, so there was a total of 48 specimens coated. Half were AA2024-T6 material and half were AA7075-T6 material. Each specimen was tested in five sites for WCA. The average WCA for each coating showed that there were two coatings that had high WCAs of 158°. One of those coatings was fragile and scratched easily. Since it damaged easily the other coating was chosen for further evaluation. The coating compositions and their WCA can be found in Table 4.3. Once the final coating was chosen more specimens were coated for testing.

TABLE 4.3

RESULTS OF WCA TESTING OF DOE COATINGS
(LINE OUTLINED IN RED CHOSEN AS FINAL COATING)

Equivalent Parameters			Water Contact Angle (WCA) Results		
wt%*Si	wt% Al	wt% Zn	Spec. #1	Spec. #2	Spec. #3
13.96	19.54	2.28	126	134	134
13.33	18.67	6.67	154	157	148
11.75	28.31	5.88	143	143	153
6.76	27.03	4.05	149	152	155
2.39	21.02	7.51	116	123	117
16.15	1.47	8.08	131	145	141
7.58	12.12	10.61	157	162	156
12.76	17.87	10.67	154	161	159
17.86	23.81	3.57	140	139	142
8.06	12.90	4.84	158	148	157
20.83	11.11	4.17	113	118	117
6.41	25.64	8.97	129	123	150
13.33	18.67	6.67	154	157	148
19.74	10.53	9.21	133	136	136
22.07	16.78	5.99	136	149	127
17.05	22.73	7.95	143	134	145

*Si contribution by Si caulking component

The design of experiments was used for optimizing the coating constituents after initially achieving a WCA of 154^{o} by trial and error. The DOE was designed around this coating composition to refine the constituent parameters with the goal of achieving a higher water contact angle. The DOE coating with the best WCA had the constituent composition of 58.7 wt% mineral spirits, 12.8 wt% silicone caulking, 17.8 wt% aluminum powders, and 10.7 wt% ZnO nanoparticles, which achieved an average WCA of 158^{o} with a maximum of 161^{o}. This coating is highlighted in red in Table 4.3. The contact angle hysteresis of the superhydrophobic coating was tested. And this testing found that CAH of the final coating was 7.6^{o}. These results are consistent with the results obtained by Momen et al. and better than those obtained by Arianpour et al. Radwan et al. achieved a WCA of 155^{o} with CAH of 4.5^{o} by electrospinning PVDF fibers and adding ZnO nanoparticles [18]. Taurino et al. used a hybrid sol-gel layer-by-layer method to apply spun resin layers and airbrushed sol-gel layers followed by perfluoropolyether (PFPE) layers on a substrate [19]. A contact angle of 155^{o} and 1^{o} CAH was achieved. Some results were superior to those achieved in this study but the process was much more complicated for the small improvement seen.

These WCA and CAH results indicate that the coating has good superhydrophobic properties. This coating would have less weight than the initial coating, which had 24.7 wt% Al and therefore would add less weight to the coated part. This would be an advantage in the aviation and automobile industries where less weight means higher gas mileage and lower fuel costs. The coating on a 1.5-inch x 1.75-inch specimen had an average weight of 0.035 g (60 cc of coating weighed 78.4 g). The final coating was found to have an average sliding angle of 4.08^{o} with a low of < 2^{o}. Four specimens were tested and the test data can be found in Appendix A. The durability of the coating was tested by exposing it to an acid, a base, and a solvent. Thirty minutes of

submersion in a solvent resulted in no change in the WCA, which indicated that the solvent had no effect on the coating hydrophobicity. After 30 minutes in an acid solution, the coating was still highly hydrophobic, with a WCA of 142^{o}, but this was a significant decrease from the original 158^{o} before testing. The coating was also immersed in sodium bicarbonate solution with a pH of 9. This was very detrimental to the coating. The contact angle was down to an average of 109^{o} from 154^{o}, but the surface was still hydrophobic. The WCA results for durability testing are shown in Table 4.4

TABLE 4.4

WCA READINGS FOR DURABILITY TESTING OF FINAL COATING

Testing	WCA Before (^{o})	WCA After (^{o})
H_2SO_4 (0.5 M)	158	142
Sodium Bicarbonate(pH=9)	153	109.9
Acetone	148	148
Heat Treat 230 C	153.6	154

The cross-hatch test was performed on two specimens according to ASTM D3359-17 using Intertape LA-26 Polyester/Rope-Fiber Laminate Tape, which has a 60 lb./in. adhesion strength. The coating showed very good adhesion to the substrate with less than 5% removal of material as rated by the rating specification tool. One of the cross-hatched specimens tested with the specification evaluation tool is shown in Figure 4.5. Both specimens tested were rated as a 4 on the rating scale, which is less than 5% material removed by the tape.

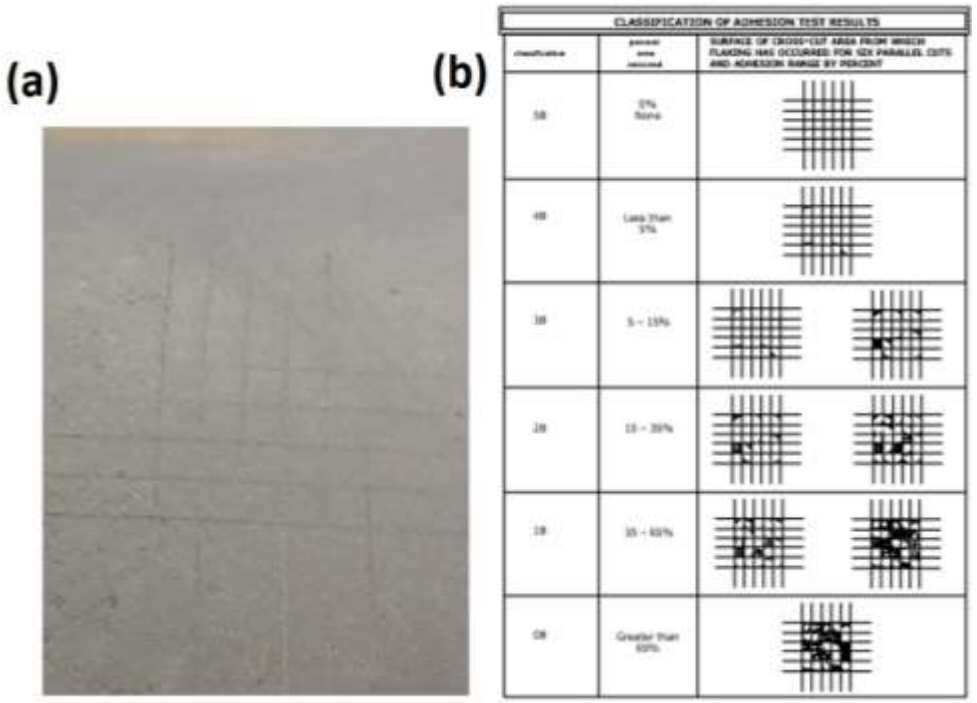

Figure 4.5. Cross-hatch adhesion test: (a) specimen after testing per ASTM D 3359, and (b) test guide to results per ASTM D 3359.

4.3.2 Statistical Analysis

The WCA results were added to the Statgraphics® Central Star[3] software with a 2-star points design, which evaluated the constituent parameters relative to the coating contact angle. Normality of the data was evaluated by the histogram shown in Figure 4.6. The over-laid normal distribution curve with the density estimate curve show the data is slightly skewed, but the data adequately represent a normal distribution for statistical analysis. A box-and-whisker plot indicated evidence of no significant difference between the means of the WCA data and the two replicates. This box-and-whisker plot is shown in the Appendix B. The normal probability plot shown in Figure 4.7 indicates a normal distribution of residuals. ANOVA data shown in Appendix B shows that no P-values were < 0.05. Also, the R^2 value was 91.7% for the design, which indicates that the design accounted for 91.7% of the variability in the contact angle data. The adjusted R^2, which takes into account the degrees of freedom, was 76.8%. The correlation matrix indicated an

orthogonal matrix, which is a reflection of the possibility of confounding effects. Overall the analysis indicates an adequate design, and the studentized residuals indicate there are no outliers since all residuals were less than 3. The studentized residual plot can also be found in Appendix B.

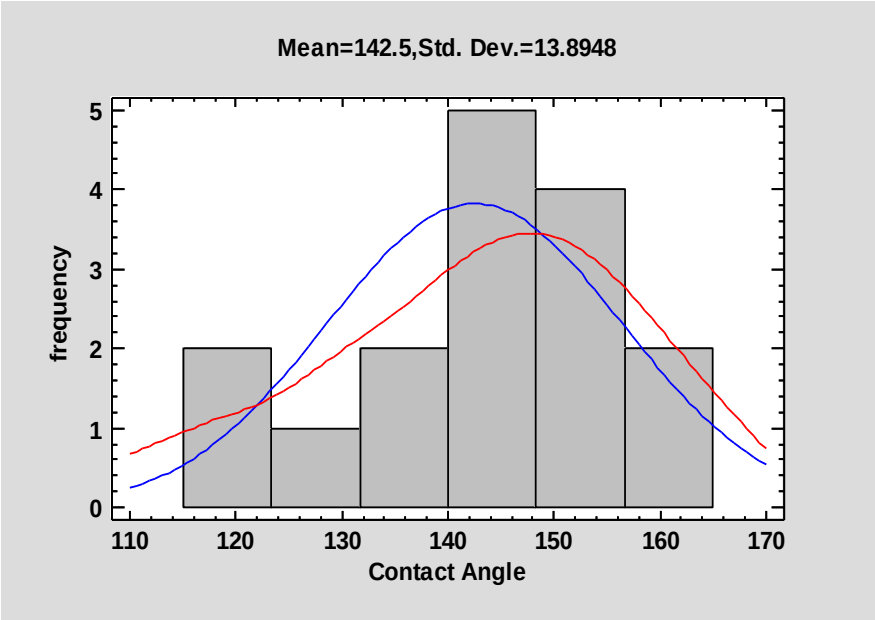

Figure 4.6. Histogram of DOE WCA data (blue line is normal curve and red line is density estimate).

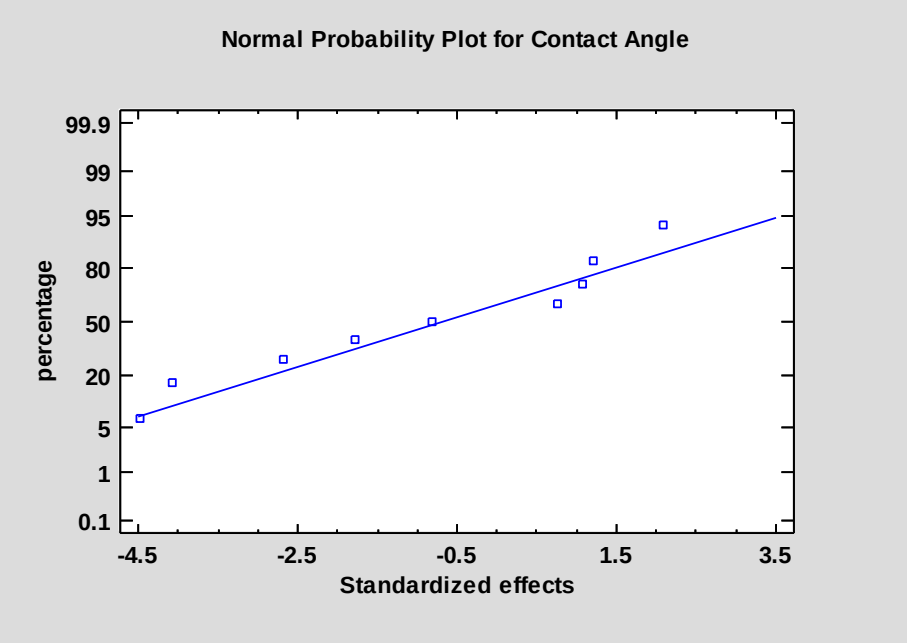

Figure 4.7. Normal probability plot used to evaluate normality of residuals.

Results of the statistical analysis indicate that the data has low variability and represents a normal distribution. The lack of variability between data sets indicates that data is consistent and the process is reproducible. The purpose of the DOE was to optimize the constituent content in the superhydrophobic coating. Although the coating WCA was improved, the main effects plot shown in Figure 4.8(a) indicates that the aluminum factor has not been optimized, while the Si caulking and ZnO WCA has peaked. The wireframe in Figure 4.8(b) shows increasing values for the Al WCA, while the Si caulking has peaked and the WCA has begun to decrease with the ZnO held constant at 4 grams. This means that the aluminum was not optimized, but another DOE could potentially be used to optimize the coating constituents. This DOE allowed the coating to be improved and the WCA increased, which helped stabilize the coating. The contact angle was increased to an average of 158^{o} from 154^{o}. Testing showed the coating to be stable with good adherence to the substrate.

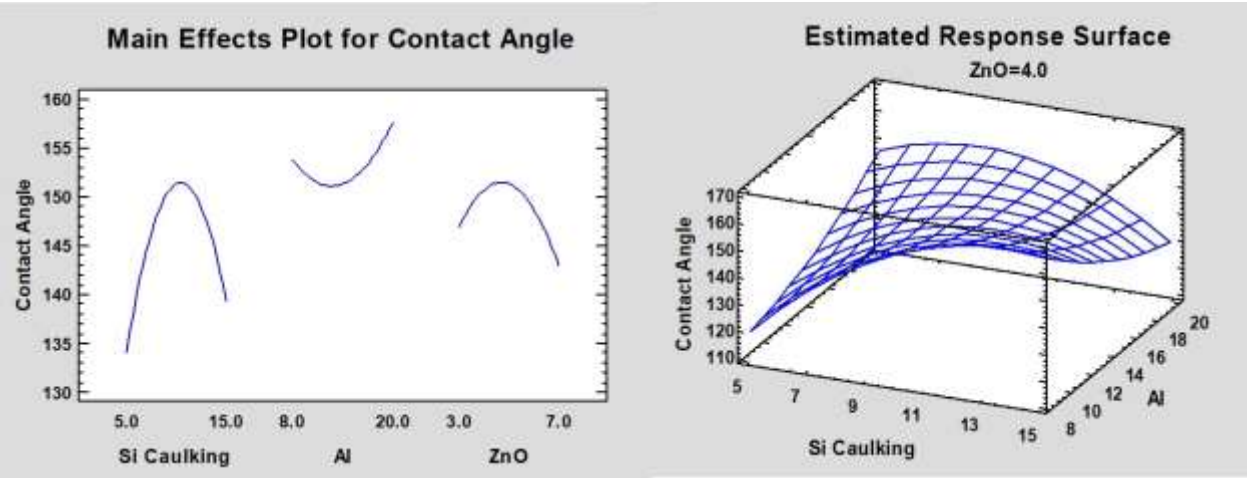

Figure 4.8. Analysis of design of experiments: (a) main effects plot from Statgraphics® analysis of DOE, and (b) wireframe representation of data.

There is evidence that another DOE could be used to optimize the coating, as shown in Figure 4.9. The 3-D mesh response surface shown in Figure 4.9(a) indicates where a WCA greater than 160^{o} could be predicted. This is the red area in the response mesh figure. In Figure 4.9(b), the

contour plot was set at 4 g for ZnO since that amount is predicted to be in the red area in the response surface mesh. The resultant surface shows a > 160º WCA area in the lower right-hand corner. This gives an indication for the ranges to develop the next DOE to optimize the coating composition.

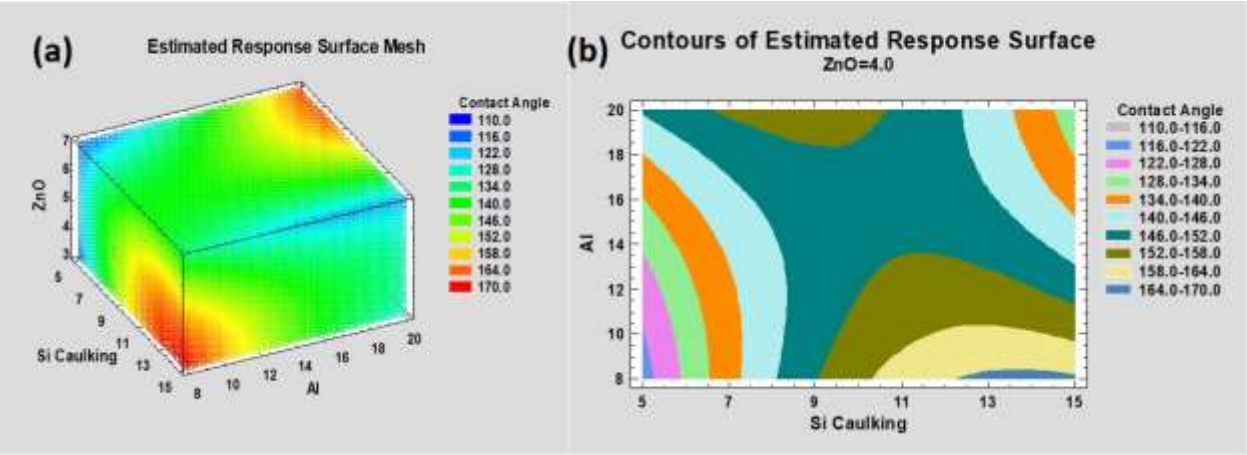

Figure 4.9. Analysis for follow-up DOE: (a) Statgraphics®-generated response surface predicting coating composition could have WCA greater than 160º, and (b) contour surface.

4.4 Conclusions

The final coating was superhydrophobic, and there is evidence that future work could improve on the coating using another DOE. Overall the study was successful in the following ways:

- A superhydrophobic coating with an average WCA of 158º, SA of 4.08º, and hysteresis of 7.6º was developed. Initially the WCA was 154º, but running an experimental design improved the coating.
- Coated specimens were heat treated at 243ºC with no effect on the WCA.
- The superhydrophobic coating was shown to have good adherence to the substrate.

- Submerging the coating in an acid and solvent had no significant effect on the WCA of the coating. However, a base with pH of 9 was detrimental, resulting in a final WCA of 109^{o} from 154^{o}.
- A Doe was used to improve the WCA which was successful in increasing the average WCA from 154^{o} to an average WCA of 158^{o}.
- The constituents in the coating were not optimized, but evaluation of the present DOE provided a range of parameters in order to develop another DOE to optimize the coating composition. There is evidence that another DOE could be successful.

4.5 References for Chapter 4

[1] A. Otten and S. Herminghaus, "How Plants Keep Dry: A Physicist's Point of View," *Langmuir*, vol. 20, no. 6, p. 2405-2408, March 16, 2004.

[2] C. Neinhuis and W. Barthlott, "Characterization and Distribution of Water-Repellent, Self-Cleaning Plant Surfaces," *Annals of Botany*, vol. 79, no. 6, pp. 667-677, June 1, 1997.

[3] M. Nosonovsk and B. Bhushan, "Hierarchical Roughness Makes Superhydrophobic States Stable," *Microelectronic Engineering*, vol. 84, no. 3, p. 382-386, 2007.

[4] L. Feng, S. Li, Y. Li, H. Li, L. Zhang, J. Zhai, Y. Song, B. Liu, L. Jiang, and D. Zhu, "Superhydrophobic Surfaces: Natural to Artificial," *Advanced Materials*, vol. 14, no. 24, pp. 1857-1860, 2002.

[5] R. N. Wenzel, "Surface Roughness and Contact Angle.," *The Journal of Physical Chemistry*, vol. 53, no. 9, p. 1466-1467, 1949.

[6] R. N. Wenzel, "Resistance of Solid Surfaces to Wetting by Water," *Industrial and Engineering Chemistry*, vol. 28, no. 8, p. 988-994, 1936.

[7] A. B. D. Cassie and S. Baxter, "Wettability of Porous Surfaces," *Transactions of the Faraday Society*, vol. 40, no. 0, pp. 546-551, June 1944.

[8] D. Quéré, A. Lafuma, and J. Bico, "Slippy and Sticky Microtextured Solids," *Nanotechnology*, vol. 14, no. 10, pp. 1109-1112, 2003.

[9] T. Sun, L. Feng, X. Gao, and L. Jiang, "Bioinspired Surfaces with Special Wettability," *Accounts of Chemical Research*, vol. 38, no. 8, pp. 644-652, 2005.

[10] A. M. Mohamed, A. M. Abdullah, and N. A. Younan, "Corrosion Behaviour of Superhydrophobic Surfaces: A Review," *Arabian Journal of Chemistry*, vol. 8, no. 6, pp. 749-765, November 2015.

[11] S. F. Jurak, E. Jurak, M. M. Rahman, and R. Asmatulu, "Nanoscale Superhydrophobic Coating for Corrosion Mitigations," in *Nanocomposites*, M. Ram, Ed., Elsevier (in press).

[12] Joshua E. Jackson, "The Cost of Corrosion Exceeds $1 Trillion in the U.S. in 2013," G2MT Laboratories, Houston, TX, 2011.

[13] G. Momen and M. Farzaneh, "Simple Process to Fabricate a Superhydrophobic Coating," *Micro & Nano Letters*, vol. 6, no. 6, pp. 405-407, 2011.

[14] F. Arianpour, M. Farzaneh, and S. A. Kulinich, "Hydrophobic and Ice-Retarding Properties of Doped Silicone Rubber Coatings," *Applied Surface Science*, vol. 265, p. 546-552, January 15, 2013.

[15] V. S. Sinyavskii and V. D. Kalinin, "Marine Corrosion and Protection of Aluminum Alloys According to Their Composition and Structure," *Protection of Metals*, vol. 41, no. 4, p. 317-328, 2005.

[16] E. N. Kutyreva, A. V. Dub, and A. G. Rakoch, "Cyclic Durability of D16T Alloy Covered with Anodic and Microplasmous Coatings," *Protection of Metals and Physical Chemistry of Surfaces*, vol. 45, pp. 829-832, December 2008.

[17] J. R. Davis, "Part III. Nonferrous Alloys and Special-Purpose Materials," ASM International, 1998.

[18] A. B. Radwan, A. M. Mohamed, A. M. Abdullah, and M. A. Al-Maadeed, "Corrosion Protection of Electrospun PVDF-ZnO Superhydrophobic Coating," *Science and Coatings Technology*, vol. 289, pp. 136-143, March 15, 2016.

[19] R. Taurino, E. Fabbri, D. Pospiech, A. Synytskab, and M. Messori, "Preparation of Scratch Resistant Superhydrophobic Hybrid Coatings by Sol-Gel Process," *Progress in Organic Coatings*, vol. 77, no. 11, pp. 1635-1641, November 2014.

CHAPTER 5

CORROSION MITIGATION EVALUATION OF SUPERHYDROPHOBIC COATING FOR CORROSION CONTROL OF ALUMINUM ALLOYS

5.0 Abstract

The friction stir spot weld (FSSW) could provide industry with a substitute for rivets as in situ fasteners. This would reduce the weight in airplanes, thereby resulting in increased fuel mileage and a reduced cost to the airlines. The friction stir welding process causes microstructural changes in the weld zone, which causes a loss of corrosion properties in the weld. The difference in potential in the weld zone compared to the base material creates a galvanic reaction between the two areas. A superhydrophobic coating has been developed for corrosion mitigation in aluminum alloys. This study evaluates that coating for corrosion control of the aluminum alloy and the FSSW. Configuration of the welds was intended to simulate the use of FSSW as in situ fasteners. AA2024-T3 and AA7075-T6 specimens were coated with the superhydrophobic coating and corrosion tested. Dissimilar lap welds of these two materials were also coated and tested with bare AA2024 and AA7075 specimens. The corrosion rates were compared to evaluate effectiveness of the coating in corrosion mitigation. Molybdenum was added to some of the coating and also tested to investigate the effect of adding this element to the coating. Coated materials with the superhydrophobic surface were found to have reduced corrosion rates compared to the bare specimens. The corrosion rates of the coated AA2024 and AA7075 specimens were improved significantly more than the coated FSSW material, possibly because the coating did not cover the weld material as uniformly as on the aluminum specimens due to the uneven surface of the weld. The addition of Mo to the coating lowered the corrosion rate to < 1 for the aluminum specimens and extended the superhydrophobicity of the coating during corrosion testing.

5.1 Introduction

The friction stir welding process was developed in 1991 by The Welding Institute, a British research facility [1]. FSW is a sub-solidus thermo-mechanical process. Here, at least two workpieces are joined by mechanically stirring the material, which is softened as heat flows into the area from friction, stirring and forging forces produced by the weld tool. A rotating probe moves through the material forging material from the leading edge of the probe into a void that forms behind the probe [2]. A shoulder at the base of the probe rotates on the surface of the material and produces frictional forces. The weld is asymmetrical and the side with rotation in the direction of travel is called the advancing side of the weld. The side with rotation in the opposite direction to movement is called the retreating side. A depiction of the FSW process is shown in Figure 5.1. During the welding process, the temperature in the weld zone is kept below the solidus temperature to allow softening of the material but not bulk solid-to-liquid transformation. This results in less residual stress and distortion as well as better mechanical properties in the friction stir weld compared to other welding methods, particularly fusion welding. There is no change in the bulk chemistry of the material during the FSW process because no fillers are required.

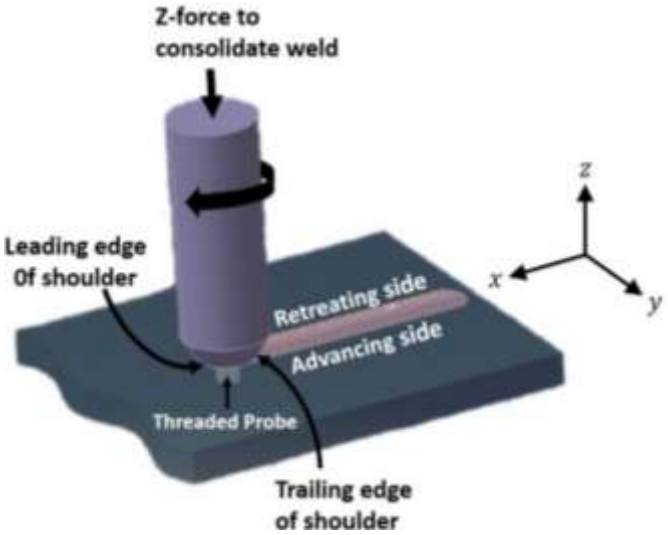

Figure 5.1. Depiction of linear friction stir welding process including axis-direction labeled in conventional terms.

The friction stir weld can be a linear weld, where the tool travels along the seam of two panels butted together, or a spot weld, where the tool is inserted and removed in place, which is referred to as a "poke" spot weld, or the probe can travel in a circular pattern making a discrete weld called a swept spot weld [3]. There also is a "refill" spot weld, which was developed and patented by GKSS Research Center Geesthacht GmbH [3]. The original friction stir spot welding methods leave an exit hole where the tool is withdrawn, but refill friction stir spot welding fills in the hole during the process. It has been shown that this improves the mechanical properties of the joint by increasing the length of the weld bond [4]. Since the exit hole is a site of increased stress and can affect the strength of the weld, the refill spot weld would be the preferred method by industry to produce a friction stir spot weld. The exit hole also gathers moisture, which would increase the potential for corrosion.

The welds in this study were dissimilar swept welds of AA2024 and AA7075 produced in the Advanced Joining and Processing Laboratory of the National Institute for Aviation Research at Wichita State University. These welds were produced in what is referred to as an OctaSpot^{TM} configuration. The tool path for the OctaSpot^{TM} is shown in Figure 5.2.

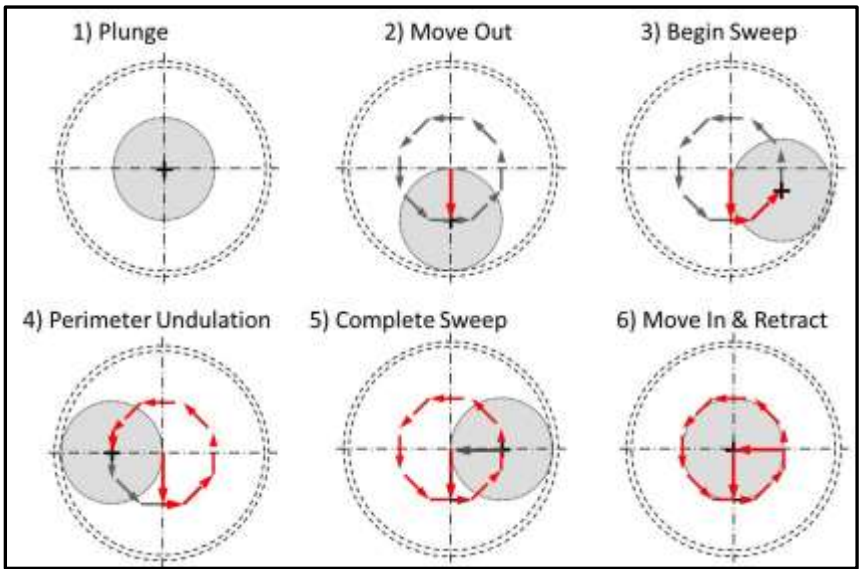

Figure 5.2. Travel path of probe during FSSW process producing OctaSpot™ weld.

Microstructural changes in the material during the FSW process causes loss of corrosion resistance due to differing potentials between the parent material and the weld material, which creates a galvanic cell. An FSSW full-field microhardness map produced in the Advanced Joining and Processing Laboratory at Wichita State University is shown in Figure 5.3. The cross section of the weld is also shown. This weld is a dissimilar lap weld of AA7075-T6 on the top and AA2024-T3 on the bottom, which would be the configuration of the weld in aviation since the skin is made of AA2024 and the stringers AA7075. The microstructural changes due to the welding process can be seen as hardness gradients in the full-field microhardness map. These changes in the microstructure are responsible for the loss of corrosion properties of the FSSW. The microstructural changes result in a galvanic reaction between the weld material and base material. This weld is a dissimilar weld, which means there is a mixture of AA2024 and AA7075 in the weld zone. This provides an additional source for a galvanic cell to form.

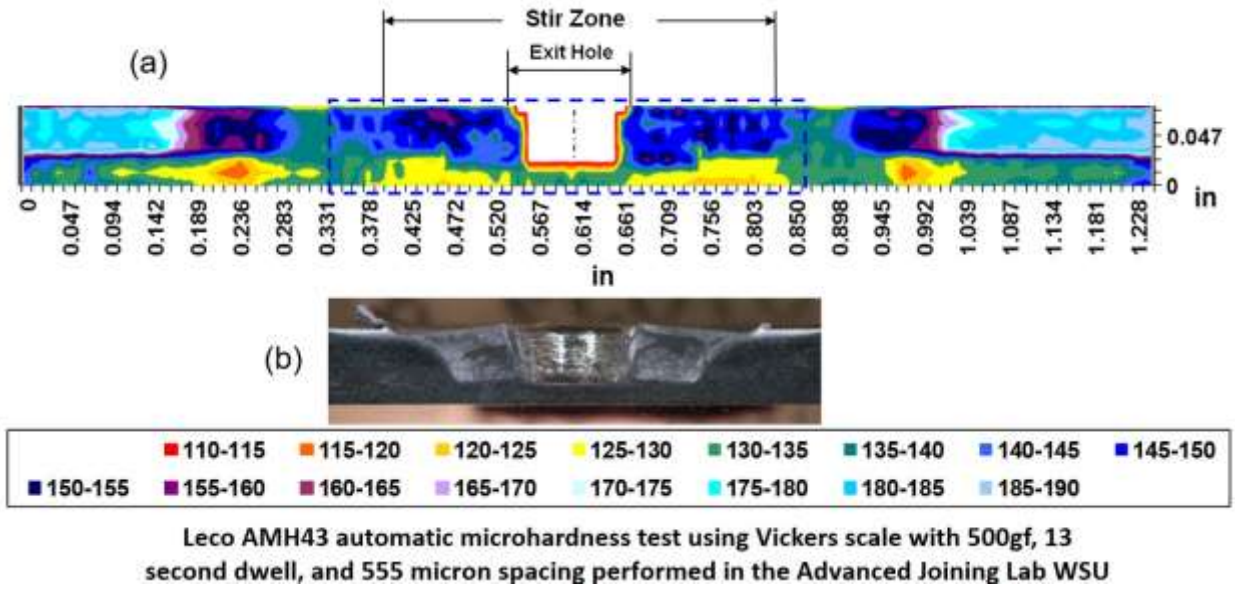

Figure 5.3. Full-field microhardness map of dissimilar FSSW lap weld of AA7075 and AA2024 material.

In this process, thermo-mechanical energy is introduced into the material as the probe effectively forges material from the leading edge to the area behind the probe, filling in a void that forms behind the probe [2]. The complex flow of material around the probe forms the nugget (stir zone). Shoulder rotation on the surface causes frictional energy, and the material adjacent to the weld is heated, forming the heat-affected zone. The thermo-mechanically affected zone is the result of mechanical forces experienced at the edge of the stir zone as the probe moves through the material and the heat that flows through the area as the nugget is formed. These changes in the microstructure are responsible for reduction of corrosion resistance in the weld zone.

There are many possible methods for addressing the problem of corrosion in the FSSW. One method that is used to address corrosion in general is to modify the composition of the metal and thus the microchemistry of the material and the corrosion properties. Formation of dispersions of ytterbium, zirconium, and aluminum on the surface of the material has been shown to provide corrosion resistance [5]. Another method to restore some of the corrosion properties to the weld is to apply post-weld heat treatments [6]. The surface can be modified by an application of another material such as thermally sprayed aluminum and molybdenum [7], or applying a CeO_2-filled sol-gel coating has been shown to provide corrosion resistance by preventing the moisture and electrolytes from reaching the surface to cause corrosion initiation [8]. Cerium-containing compounds in theory can block the anodic sites through precipitation of insoluble cerium hydroxides. Hydrophobicity has been shown to prevent moisture from gaining access to composite materials [9]. A superhydrophobic coating can potentially provide added corrosion protection due to the layer of air that gets trapped on the surface in the trough between asperities of the micro-nanostructured surface morphology, which provides a composite contact between the material surface and water.

In this study a superhydrophobic coating previously developed and tested for durability and superhydrophobic properties was applied to AA2024 and AA7075 specimens as well as friction stir spot welds to evaluate the effectiveness of this coating in corrosion mitigation. Lap welds were made of 0.05-inch AA2024-T3 and 0.04-inch AA7075-T6 material for this study. The superhydrophobic coating that was developed was shown to have an average water contact angle of 158^{o}, a sliding angle of 4.08^{o}, and hysteresis between the advancing and receding angle of 7.6^{o}. Acetone was shown to have no effect on the WCA. There was some decrease in the WCA with submersion in sulfuric acid, but it was still highly hydrophobic. The material was also heat treated up to 230^{o}C with no effect on the superhydrophobicity of the coating. The coating was then submerged in sodium bicarbonate, which had a significant detrimental effect on the hydrophobicity of the coating. The WCA was decreased to 109^{o} from 154^{o}. An adhesion cross-hatch test showed good adhesion of the superhydrophobic coating to the substrate.

5.2 Experimental Procedure

Zinc oxide nanoparticles < 45 nm were obtained from U.S. Research Nanomaterials, Inc., and an aluminum powder of mesh 200 (74 μm) was obtained from Acros Organics. ZnO was used to provide UV protection to the coating and also it is nearest to Al on the corrosion potential chart, which would reduce the possibility of there being a galvanic reaction between the metallic particles. Silicone was used as the low surface energy component of the coating in the form of GE Silicone II 10.1-oz Clear Silicone Caulking obtained from Lowe's Home Improvement. Jasco Paint Thinner (100% Mineral Spirits) were obtained from Lowe's Home Improvement as well. AA2024-T3 and AA7075-T6 sheets were obtained from TW Metals Inc., Park City, Kansas. The material properties of these metal alloys are shown Table 5.1.

TABLE 5.1

MAXIMUM MATERIAL COMPOSITION OF AA2024-T3 AND AA7075-T6 BY WT% [10]

Material	*Tested Tensile Strength (ksi)*	*Composition (wt %) max.*										
		Si	*Fe*	*Cu*	*Mn*	*Mg*	*Cr*	*Zn*	*Ti*	*Other*		*Al*
										Ea.	*Tot.*	
2024-T3	LT:67.9-70.2	0.5	0.5	3.8-4.9	0.3-0.9	1.2-1.8	0.1	0.25	0.15	0.05	0.15	Bal
7075-T6	---	0.4	0.5	1.2-2.0	0.3	2.1-2.9	0.18-0.28	5.1-6.1	0.3	0.05	0.15	Bal

Swept friction stir spot welds were made with an MTS® ISTIR PDS five-axis motion, seven-axis force monitoring FSW machine with a 4130-steel anvil. The weld tool design used to produce the welds was the Trivex, with a convex 0.3-inch shoulder with three scrolls and three flutes. The threaded probe was 0.045 inch in length and 0.08 inch in diameter. The FSW gantry and weld tool design used to make the FSSW is shown in Figure 5.4. Welds were made at the Advanced Joining and Processing Laboratory at Wichita State University.

(a) (b)

Figure 5.4. Producing FSSW: (a) MTS® gantry machine, and (b) weld tool design used to produce swept FSSW.

The tool chosen for this process has been shown to be able to consistently produce strong defect free welds. Parameters were identified that would produce defect-free welds and would minimize heat production in the weld zone and its effect on corrosion properties. The weld tool and weld parameters were chosen to try to ensure that the contribution of the welding process to

the variation in the corrosion properties of the welds would result in consistent quality welds so that the effect of the superhydrophobic coating on the corrosion properties could be more readily seen when comparing the coated welds to bare welds. The parameters used for welding are shown in Table 5.2 After welding the FSSW panels were cut into 1.5-inch x 1.75-inch specimens for coating and testing. Before cutting, the welds were sanded to provide a smooth surface.

TABLE 5.2

WELD PARAMETERS USED TO PRODUCE STUDY WELDS

Tool	Rotational Speed	Travel Speed	Lead Angle	Forge Load
Trixex (Concave)	1740	8.45	0.5	1000

The superhydrophobic coatings that were corrosion tested were prepared by mixing the aluminum powder, ZnO nanoparticles, silicone caulking, and mineral spirits using a magnetic stirrer. A coating was also prepared with 2 wt% molybdenum for testing. Specimens of 1.5-inch x 1.75-inch size were cut from the AA2024 and AA7075 aluminum material sheets. Half of the samples tested were AA2024 and half were AA7075. The specimens of flat bare material and weld specimens were cleaned in acetone and ethanol by sonication, 10 minutes each, to remove oils and dirt before etching. The specimens were then electrochemically etched in 0.7 M sulfuric acid under 20 V DC current for 30–40 minutes. Before and after application of the superhydrophobic coating, the specimens were weighed and the WCA was obtained. The mineral spirits were measured into a container, and the silicone caulking was measured and added to the mineral spirits. The solution was mechanically mixed for 30 minutes by magnetic stirrer. Next the ZnO nanoparticles (< 45 nm) were measured and added to the mixture and stirred again for 30 minutes. Finally, the Al particles (200 mesh or 74 μm) were measured and added, followed by mixing for 2 hours. Each specimen for testing was coated by dipping into the prepared superhydrophobic coating. Next the specimens

were placed in a desiccator under negative pressure to remove air bubbles from the applied coating. After drying, the specimens were heat treated for 30 minutes at 150^{o}C to remove residual mineral spirits from the coating.

The GAMRY ParaCell™ Electrochemical Cell was used for electrochemically testing the coated specimens with a reference saturate calomel electrode (SCE). Testing was carried out in 0.5 M NaCl. Specimens were immersed in the 0.5 M NaCl for 30 days. At days 2, 6, 14, and 30, they were removed and electrochemically tested. The WCA was also taken on days 6, 14, and 30.

5.3 Results and Discussion

Corrosion testing was completed on the initial superhydrophobic coating developed by the trial and error method after achieving a WCA of 153^{o}. Constituents of the initial coating were 12.3 wt% Si, 24.7 wt% Al, and 6 wt% Zn, with 57 wt% mineral spirits. A 2 wt% molybdenum was added to a batch of this coating to evaluate its effect. The average results of this corrosion testing are shown in Figure 5.5. Adding the MO modestly improved the corrosion properties of the coating but its addition significantly improved the coatings ability to maintain its hydrophobicity, which decreased during corrosion testing, even though the coating was still highly hydrophobic. The superhydrophobic coating significantly improved the corrosion rate of the material.

The Tafel data for the coating showed a negative shift to the left and positive shift up, which indicated an improvement in corrosion potential toward the cathodic region. This data is shown in Figure 5.6. This is in line with the corrosion rates obtained during testing. The silicone coating maintained its hydrophobicity but was not able to achieve superhydrophobicity without the addition of metallic particles. Adding micro- and nano-sized particles provided the micro-nanostructured morphology needed to achieve a WCA above 150^{o}.

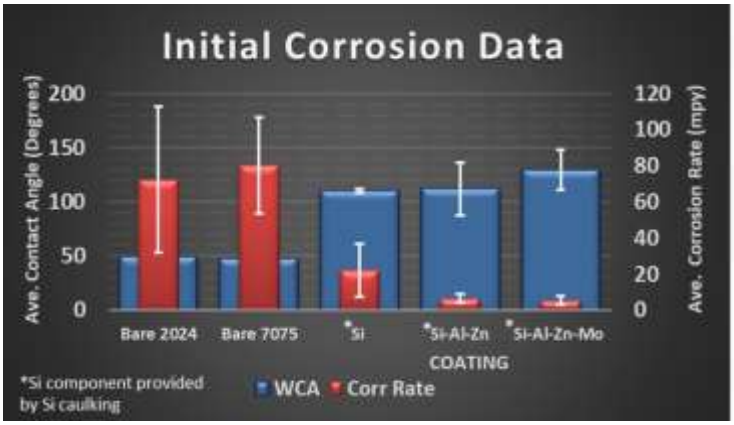

(a)

WCA (degrees)		
Constituent	Initial	After Testing
Si Coating	115	110
Si-Al-Zn	151	138
Si-Al-Zn+Mo	141	131

(b)

Figure 5.5. Initial coatings corrosion data and WCA: (a) average results for data obtained over 30 days of corrosion testing of initial superhydrophobic coatings, and (b) WCA during testing.

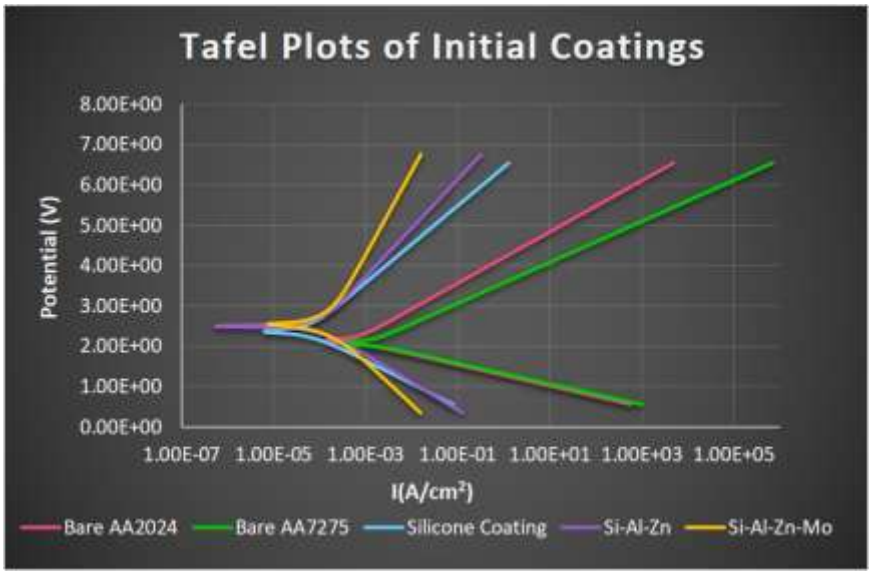

Figure 5.6. Plot of Tafel data for each initial coating tested.

Data from corrosion testing on day 14 of the initial electrochemical testing is shown in Table 5.3. The current density of the coated specimens compared that of bare materials is much lower and has increased, which indicates corrosion resistance. The coating was successful in protecting the substrate from corrosion attack, as seen by the low corrosion rate compared to that of bare aluminum. The addition of molybdenum to a coating had the effect of lowering the corrosion rate and significantly extending the superhydrophobicity of the coating.

TABLE 5.3

DATA FROM ELECTROCHEMICAL TESTING DAY 14 OF CORROSION TESTING OF INITIAL SUPERHYDROPHOBIC COATING

Experimental Sample	Initial Electrochemical Testing		
	I_{corr}(mA)	E_{corr}(V)	Corrosion Rate (mpy)
Bare 2024	5.46E-01	2.130	46.210
Bare 7075	1.16E+00	2.080	98.020
Si-Al-Zn-Mo	1.44E-01	2.540	7.978
Si-Al-Zno	9.42E-02	2.500	12.190
Si	5.37E-02	2.370	4.547

The final superhydrophobic coating was developed with the assistance of a design of experiments. The constituents of the final coating were 58.7 wt% mineral spirits, 12.7 wt% Si, 17.9 wt% aluminum, and 10.7 wt% Zn. The aluminum and FSSW specimens were coated with the final superhydrophobic coating and corrosion tested. The averages over the 30-day corrosion testing are shown in Figure 5.7.

Figure 5.7. Final coating corrosion data averages with WCA.

The bare aluminum specimens had a large amount o variation of the data but the final result was reasonable. The coating improved the corrosion rates of the coated aluminum and weld specimens

compared to corrosion rates for the bare aluminum. The corrosion rates for the coated weld were less than that of the bare aluminum where the weld material usually has much lower resistance to corrosion. The coated weld and aluminum specimens maintained their hydrophobicity during corrosion testing. The coated welds remained very close to superhydrophobic, above 140^{o}, while the coated aluminum specimens were 130^{o} for the surface WCA. The bare specimens were less than 90^{o}, which indicates hydrophilicity.

The water contact angle testing of the corrosion-tested coated specimens showed that the WCA decreased during their corrosion testing but not as much as for the bare aluminum specimens. Although the WCA decreased with corrosion testing, the coatings were still highly hydrophobic. The coating was shown to be resistant to the effect of emersion in the NaCl solution. The initial and final water contact testing results are shown Figure 5.8.

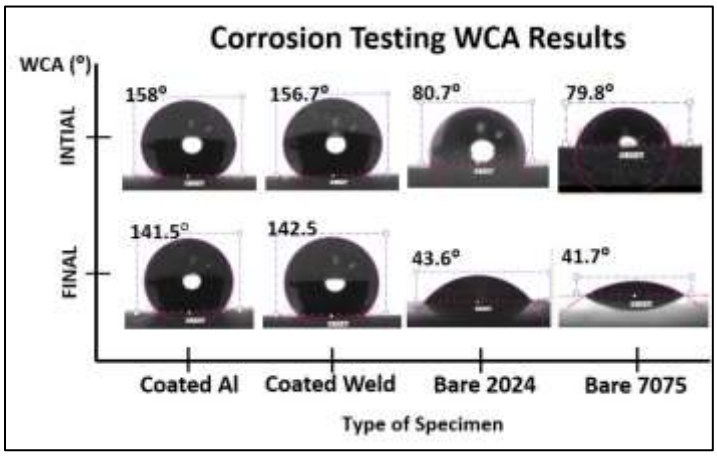

Figure 5.8. Static water contact angle results before and after corrosion testing.

The Tafel curves of these specimens are shown in Figure 5.9. These plots for the coated weld and coated aluminum specimens are compared with Tafel plots for a bare FSSW material and bare aluminum specimens. The coated-specimen Tafel plots again shifted to the left and positively upward but much more so than for the initial coating, which confirms the corrosion

results and indicates that the DOE was successful in improving the coating by shifting the corrosion potential to be more anodic.

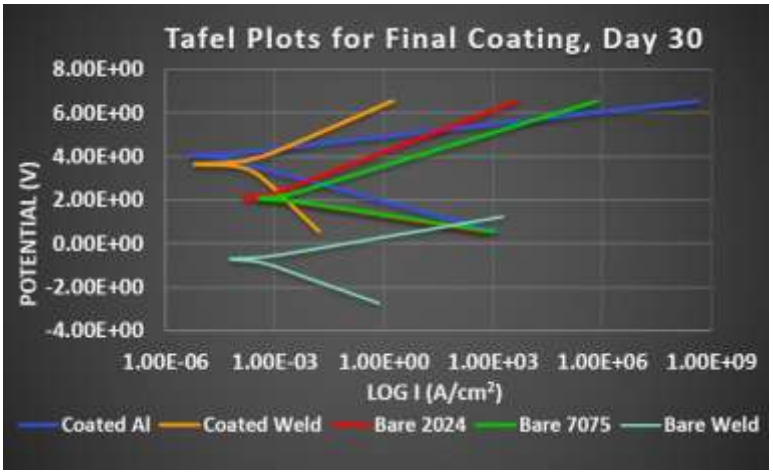

Figure 5.9. Bare specimens compared to final coating applied to aluminum specimens and FSSWs.

The some of the data from the electrochemical testing of the final coating corresponding to the Tafel plots shown in Figure 5.9 is shown in Table 5.4.

TABLE 5.4

ELECTROCHEMICAL DATA FROM INITIAL TESTING, DAY 2, AND DAY 6 OF CORROSION TESTING OF FINAL COATING

Experimental Sample	Day Zero			Day Two			Day Six		
	I_{corr}(mA)	E_{corr}(V)	Corrosion Rate (mpy)	I_{corr}(mA)	E_{corr}(V)	Corrosion Rate (mpy)	I_{corr}(mA)	E_{corr}(V)	Corrosion Rate (mpy)
Bare 2024	2.83E+00	2.05	239.20	1.54E+00	2.36	130.20	1.37E+00	2.37	110.80
Bare 7075	1.38E+00	2.12	116.80	1.12E+00	2.25	94.53	9.73E-01	1.16	82.39
Coated Al	2.51E-01	2.74	22.05	4.68E-01	3.84	41.11	4.56E-01	3.95	40.05
Coated Weld	1.21E+00	2.63	106.20	8.67E-01	3.91	123.10	4.28E-01	3.89	62.93
Bare Weld	2.33E+00	-0.868	269.20	1.07E+00	-0.94	76.15	5.46E-01	-0.944	37.56

The results possibly reflect passivation of the surfaces of the metals as the corrosion rates of the bare materials are significantly lower than initially. The current density, i_{corr}, is lower for the coated material than the bare specimens and the corrosion potential, E_{corr}., increases on day two but decreases or stays steady on day 14 which could be due to passivation of the surface. The

corrosion rate remains lower in the coated weld and aluminum specimen than that in bare aluminum throughout but the coated weld has a higher corrosion rate than the bare weld on day 14.

5.4 Conclusions

Specimens coated with a superhydrophobic coating developed using a design of experiments were corrosion tested with bare aluminum specimens. The coated aluminum and FSSW material were compared to corrosion results for bare specimens of the same The corrosion data and Tafel curves indicated that there was a significant improvement in the corrosion resistance of the coated specimens compared to the bare specimens. The coating is effective in mitigating the corrosion of aluminum FSSW material, which has been a concern when industry considers using friction stir welding in production processes. Quality issues are still being researched for solutions, such as those pertaining to weld defects that cannot be readily seen by visual inspection. Potential solutions have been suggested and are being developed. A superhydrophobic coating is a promising solution for restoring corrosion resistance to the weld material

5.5 References for Chapter 5

[1] W. M. Thomas, E. D. Nicholas, J. C. Needham, M. G. Murch, P. Temple-Smith, and C. J. Dawes, "Friction Welding," United States Patent 5,460,317, October 24, 1995.

[2] K. Kumar and S. V. Kailas, "The Role of Friction Stir Welding Tool on Material Flow and Weld Formation," *Materials Science and Engineering A*, vol. 485, no. 1-2, pp. 367-374, June 25, 2008.

[3] S. Jurak, E. Jurak, and R. Asmatulu, "Recent Progress in Friction Spot Welding Processes of Metallic Materials," in *Composites and Advanced Materials Expo: Combined Strength. Unsurpassed Innovation*, CAMX 2014, Orlando, FL, October 13–16, 2014.

[4] K. Tokaji, Y. Tozaki, T. Kurita, and S. Murata, "Effect of Re-Filling Probe Hole on Tensile Failure and Fatigue Behavior of Friction Stir Spot Welded Joints in Al-Mg-Si Alloy," *International Journal of Fatigue*, vol. 30, no. 10-11, pp. 1956-1966, October-November 2008.

[5] H.-c. Fang, K.-h. Chen, Z. Zhang, and C.-j. Zhu, "Effect of Yb Additions on Microstructures and Properties of 7A60 Aluminum Alloy," *Transactions of Nonferrous Metals Society of China*, vol. 18, no. 1, pp. 28-32, 2008.

[6] K. N. Krishnan, "The Effect of Post Weld Heat Treatment on the Properties of 6061 Friction Stir Welded Joints," *Journal of Materials Science*, vol. 37, no. 3, p. 473-480, 2002.

[7] A. Naimia, H. Yousfi, and M. Traric, "Microstructure and Corrosion Resistance of Molybdenum and Aluminum Coatings Thermally Sprayed on 7075-T6 Aluminum Alloy," *Protection of Metals and Physical Chemistry of Surfaces*, vol. 48, no. 5, p. 557-562., 2012.

[8] M. Schem, T. Schmidt, J. .Gerwann, M. Wittmar, M. Veith, G. E. Thompson, I. S. Molchan, T. Hashimoto, P. Skeldon, A. R. Phani, S. Santucci, and M. L. Zheludkevich, "CeO_2-filled sol-jel coatings for corrosion protection of the AA2024-T3 Alloy," *Corrosion*, vol. 51, no. 10, pp. 2304-2315, 2009.

[9] S. Kasaragadda and R. Asmatulu, "Effects of Surface Hydrophobicity on Moisture Ingression of Fiber Reinforced Laminate Composites," in *The Composites and Advanced Materials Expo—CAMX 2015*, Dallas, TX, October 27-29, 2015.

[10] J. R. Davis, "Part III. Nonferrous Alloys and Special-Purpose Materials," ASM International, 1998.

Chapter 6

GENERAL CONCLUSIONS

Corrosion of metallic surfaces continues to be a costly problem, but research continues to develop adequate corrosion mitigation solutions. In this study, the use of superhydrophobic coatings was investigated, and a surface coating was developed using a design of experiments approach. The final coating was superhydrophobic, and there is evidence that future work could improve on this coating using another DOE. Overall, the study was successful in the following ways:

- A superhydrophobic coating was developed with an average WCA of 158^{o}, SA of 4.08^{o}, and hysteresis of 7.6^{o}. Initially the WCA was 154^{o}, but running an experimental design improved the coating.
- Coated specimens were heat treated at 243^{o}C with no effect on the WCA.
- The superhydrophobic coating was shown to have good adherence to the substrate, with only 5% of material removal with a cross-hatch tape test.
- Submerging the coating in an acid and solvent had no significant effect on the WCA of the coating. However, a base with pH of 9 was detrimental, resulting in a final WCA of 109^{o} from 154^{o}.
- The superhydrophobic coating was effective in significantly impeding the corrosion attack on the metal substrate and was also effective in protecting the FSSW from corrosion attack. The coated FSSW had a lower corrosion rate and lower current density than that of bare aluminum material.
- Specimens coated with a superhydrophobic coating developed using the DOE were corrosion tested with bare aluminum specimens. The coated aluminum and FSSW material

were compared to corrosion results for bare specimens of aluminum and FSSW material. The corrosion data and Tafel curves indicated there was a significant improvement in the corrosion resistance of the coated specimens compared to the bare specimens.

- The constituents in the coating have not been optimized but the evaluation of the present DOE provided a range of parameters in order to develop another DOE to optimize the coating composition. There is evidence that another DOE could be successful in improving surface morphology and the water contact angle
- The coating is effective in significantly mitigating the corrosion of aluminum FSSW material which has been a concern when industry considers using friction stir welding in production processes. There are still quality issues being researched for solutions such as weld defects that cannot be readily seen by visual inspection. Potential solutions have been suggested and are being developed.
- A superhydrophobic coating is a promising solution for restoring the corrosion resistance to weld material.

CHAPTER 7

FUTURE WORK

In this study, a superhydrophobic coating was developed, which testing showed had good superhydrophobic properties, but the constituents were not optimized. Therefore, more refinement of the coating is possible. This coating has promise for use in corrosion control but is in the early stages and requires more refinement. There is evidence that another design of experiments could possibly refine the coating and increase the water contact angle of the surface. Future work could focus on the following:

- Continue development of coating by running a DOE to optimize the coating.
    - Optimize constituents.
    - Investigate and optimize microparticle size.
    - Decrease variation by optimizing the mixing time and method of constituents.
- Continue research and development to make the coating more durable, because the coating adheres well to the substrate but scratches too easily.
    - Change the source of the silicone.
    - Change the low surface energy contribution.
- Characterize the coating surface morphology using SEM.
    - Visualize the surface surface morphology.
    - Gain data of thickness of coating.
- Characterize the coating surface morphology using AFM.
    - Gain data for the roughness factor, which could identify the roughness of the coating and possibly quantify the herterogenous surface.

- Calculate the percentage of solid-to-air surface contact to quantify the superhydrophobic properties of coating.

APPENDICES

APPENDIX A

EXPERIMENTAL DATA

This appendix contains experimental data relating to testing of the final coating. Specimens were prepared by electrochemically etching in 0.7 M H2SO4. Each specimen was weighed before and after etching. Then they were coated and weighed when dry. Contact angles were obtained before and after etching as well as after coating. This data for the initial and final coatings are shown in Table A.1. The aluminum AA2024-T3 average WCA bare was 56º, and the average WCA for the AA7075-T6 material was 59º.

TABLE A.1

WEIGHTS AND WCA FOR COATED SPECIMENS

	Initial Coating			Final Coating					
Specimen	#1	#2	#3	#1	#2	#3	#4	#5	#6
Wt. before etch (g)	6.33	5.11	6.27	5.17	6.34	5.05	5.1	6.33	5.11
Wt. before Coated (g)	6.27	5.05	6.22	5.13	6.3	5.01	5.02	6.27	5.03
Wt. loss (g)	0.06	0.06	0.05	0.04	0.04	0.04	0.08	0.07	0.08
Wt. Post Coating (g)	6.41	5.16	6.36	5.31	6.41	5.12	5.11	6.35	5.10
Coating Wt. (g)	0.15	0.11	0.14	0.18	0.11	0.11	0.09	0.08	0.07
Coating WCA (º)	153	152	157	157	162	156	157	158	157
Al WCA after Etch (º)	77	59	71	62	52	57	61	37	59

Sliding angle tests were run on three specimens coated with the final coating. The three specimens were #4, #5, and #6 in Table A.1. Readings were taken at four sites on each specimen.

The average of the three specimen SA readings was 4.08°. Results of the testing are shown in Table A.2.

TABLE A.2

RESULTS OF SLIDING ANGLE TESTING ON FINAL COATING

Site	Specimen		
	#4 SA	#5 SA	#6 SA
#1	6.5	8	7.5
#2	2	3.5	3
#3	2	5	4
#4	2.5	3	2
Average SA	3.25	4.875	4.125
Contact Angle	157	158	157

APPENDIX B

STATISTICAL ANALYSIS RESULTS FOR FINAL COATING

There is evidence that the experimental design explains 91.7% of the error by examining the R^2 value. Since the P-values are not < 0.05, there is strong evidence that there is no difference in the means of the sets of data. Some of the ANOVA results are shown in Table B.1.

TABLE B.1

SOME ANOVA RESULTS OF STATISTICAL ANALYSIS

R-squared = 91.726 percent
R-squared (adjusted for d.f.) = 76.8328 percent
Standard Error of Est. = 6.91978
Mean absolute error = 3.51111
Durbin-Watson statistic = 1.6043 (P=0.2691)

Further ANOVA for Variables in the Order Fitted

Source	*Sum of Squares*	*Df*	*Mean Square*	*F-Ratio*	*P-Value*
Si	93.4664	1	93.4664	0.52	0.4865
Al	18.8128	1	18.8128	0.10	0.7529
Zn	181.083	1	181.083	1.00	0.3374
Model	293.362	3			

The box-and-whisker plot shown in Figure B.1 indicates there is no statistical difference between the means of the WCA data and the two replicates.

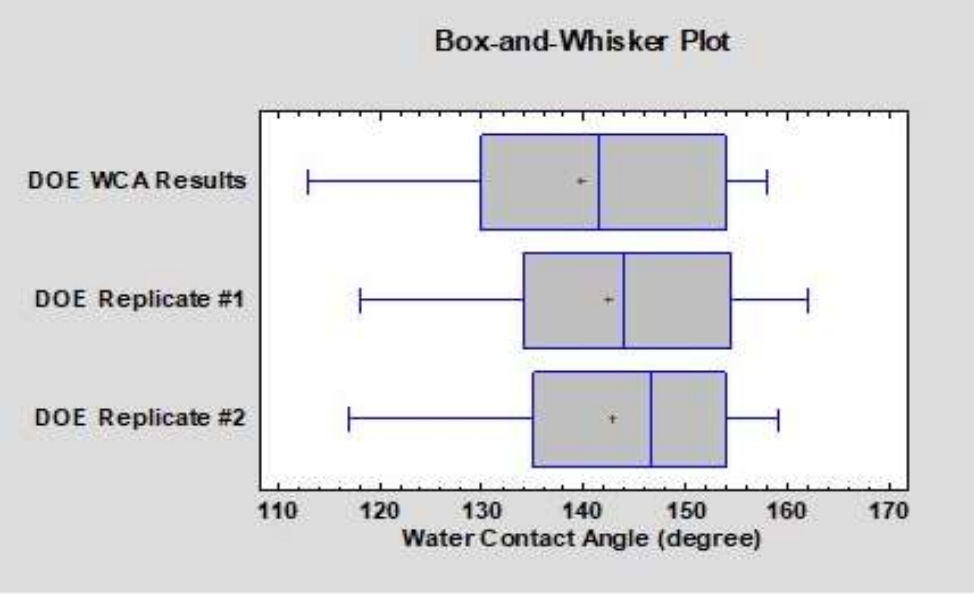

Figure B.1. Box-and-whisker plot for statistical analysis of final coating data.

The studentized residual plot is shown in Figure B.2. This figure examines the difference between the predicted value and the actual value obtained, which is called a residual. Large

residuals are an indication of outliers. The studentized residuals show no indication of outliers because all residuals are less than 3.

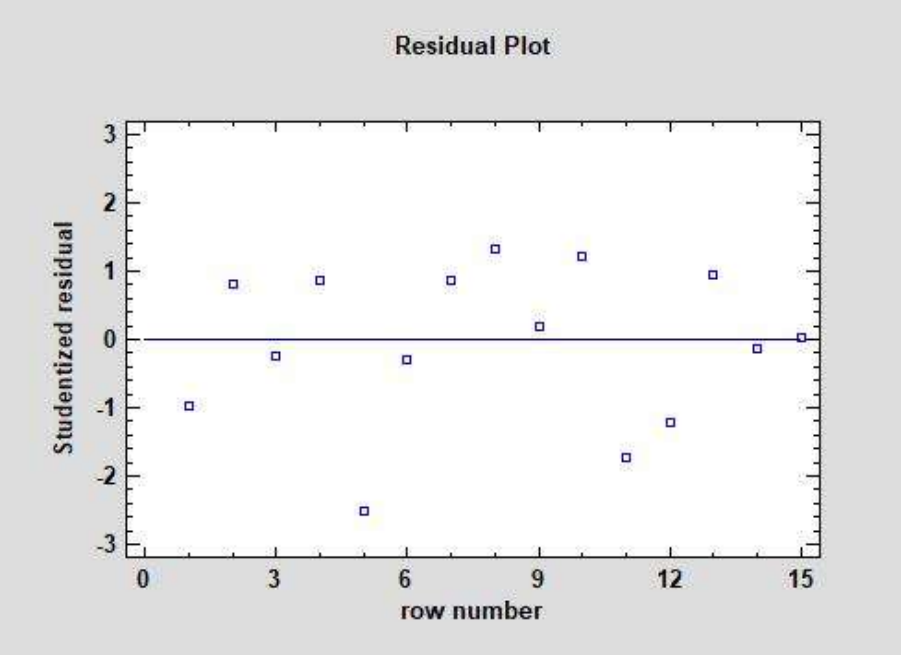

Figure B.2. Studentized residuals for DOE WCA data.